



University of Kentucky
UKnowledge

University of Kentucky Doctoral Dissertations

Graduate School

2007

HELIUM (e, 2e) COPLANAR AND OUT-OF-PLANE EXPERIMENTS

Bruno A. deHarak

University of Kentucky, badeha2@uky.edu

[Right click to open a feedback form in a new tab to let us know how this document benefits you.](#)

Recommended Citation

deHarak, Bruno A., "HELIUM (e, 2e) COPLANAR AND OUT-OF-PLANE EXPERIMENTS" (2007). *University of Kentucky Doctoral Dissertations*. 552.

https://uknowledge.uky.edu/gradschool_diss/552

This Dissertation is brought to you for free and open access by the Graduate School at UKnowledge. It has been accepted for inclusion in University of Kentucky Doctoral Dissertations by an authorized administrator of UKnowledge. For more information, please contact UKnowledge@lsv.uky.edu.

ABSTRACT OF DISSERTATION

Bruno A. deHarak

The Graduate School
University of Kentucky

2007

HELIUM ($e, 2e$) COPLANAR AND OUT-OF-PLANE EXPERIMENTS

ABSTRACT OF DISSERTATION

A dissertation submitted in partial fulfillment of the
requirements for the degree of Doctor of Philosophy
in the College of Arts and Sciences
at the University of Kentucky

By
Bruno A. deHarak

Lexington, Kentucky

Director: Prof. N.L.S. Martin, Professor of Physics and Astronomy

Lexington, Kentucky

2007

Copyright © Bruno A. deHarak 2007

ABSTRACT OF DISSERTATION

HELIUM ($e, 2e$) COPLANAR AND OUT-OF-PLANE EXPERIMENTS

We have measured relative triple differential cross sections (TDCS) for the electron impact ionization of helium in both coplanar and out-of-plane geometries using the ($e, 2e$) technique. All experiments have been performed in a regime where exchange effects can be largely ignored. For the coplanar experiments we report scattered (rather than ejected) angular distributions of the TDCS for incident energies of 150 eV and 488 eV, and an ejected electron energy 34.5 eV. At both incident energies experiments were carried out for a fixed pair of ejected directions $+90^\circ, -90^\circ$ and a range of scattering angles $-30^\circ \rightarrow +30^\circ$, and also for a fixed pair of ejected directions $+75^\circ, -105^\circ$ and a range of scattering angles $-34^\circ \rightarrow +18^\circ$. The data are presented directly as pairs of ($e, 2e$) scattered electron angular distributions, and in the manipulated form of their sum, difference, and the ratio difference/sum; these manipulated forms provide a particularly rigorous test of theory. These are compared with up to five types of theoretical calculations. Good, but not perfect, agreement is found between experiment and calculations that include significant post collision interaction effects.

The out-of-plane experiments measured ejected electron angular distributions for the helium autoionizing levels $(2s^2)^1S$, $(2p^2)^1D$, $(2s2p)^1P$, and for direct ionization. These experiments required the modification of an (originally coplanar) ($e, 2e$) spectrometer; specifically a novel rotatable mount for the electron gun was implemented. These modifications have allowed us to make measurements over the full 2π radians of a plane that includes the momentum transfer direction and is perpendicular to the scattering plane. The incident electron energy was 488 eV, the scattering angle was 20.5° , and the momentum transfer was 2.1 au. The results are interpreted in terms of a simple Born approximation calculation in which each autoionizing state adds an L -dependent resonant term to the scattering amplitude.

KEYWORDS: Atomic Physics, Electron Impact Ionization, Autoionization,
($e, 2e$), Helium

Bruno A. deHarak
(Author's Name)

Nov. 9, 2007
(Date)

HELIUM ($e, 2e$) COPLANAR AND OUT-OF-PLANE EXPERIMENTS

By

Bruno A. deHarak

Nicholas Martin

(Director of Dissertation)

Joseph Brill

(Director of Graduate Studies)

Nov. 9, 2007

(Date)

DISSERTATION

Bruno A. deHarak

The Graduate School
University of Kentucky

2007

HELIUM ($e, 2e$) COPLANAR AND OUT-OF-PLANE EXPERIMENTS

DISSERTATION

A dissertation submitted in partial fulfillment of the
requirements for the degree of Doctor of Philosophy
in the College of Arts and Sciences
at the University of Kentucky

By
Bruno A. deHarak

Lexington, Kentucky

Director: Prof. N.L.S. Martin, Professor of Physics and Astronomy

Lexington, Kentucky

2007

Copyright © Bruno A. deHarak 2007

Table of Contents

Table of Contents	iii
List of Tables	v
List of Figures	vi
Chapter 1: Introduction	1
Chapter 2: The $(e, 2e)$ technique	4
Chapter 3: Electron-atom scattering	7
3.1 Cross-section	7
3.2 Elastic scattering	9
3.3 Inelastic scattering	13
Chapter 4: Autoionization	17
Chapter 5: Experimental apparatus	28
5.1 Vacuum system	31
5.2 Electron gun	34
5.3 Gas jet	37
5.4 Spectrometers	37
5.5 Timing circuitry	43
5.6 Computer control and data collection	46
5.7 Scattered turntable modification	48
5.8 Movable electron gun mount	52
5.8.1 Alignment	55
5.8.2 Ejected angular distribution	57
5.8.3 Calibration	60
Chapter 6: Coplanar momentum transfer dependence	62
6.1 Introduction	62
6.2 Theory	65
6.3 Experimental details	70
6.4 Results	74
6.5 Conclusions	78

Chapter 7: Out of plane studies	88
7.1 Introduction	88
7.2 Theory	90
7.3 Experimental Details	91
7.4 Results and discussion	94
7.5 Conclusions	96
Appendix A: The ejected electron spectrum of He below the $N = 2$ threshold . . .	98
A.1 Introduction	98
A.2 Experimental method	100
A.3 Results and discussion	101
A.4 Summary and conclusions	107
Appendix B: SIMION	120
B.1 SIMION Overview	120
B.2 Purpose	120
B.3 Model Considerations	122
B.3.1 Potential Array Size	122
B.3.2 Distribution of Trajectories	124
B.4 Point Source	126
B.5 Line Source	132
B.6 Predicted versus Actual Results	132
B.7 Conclusion	135
Appendix C: Thermal broadening	136
C.1 Conclusion	139
Appendix D: Analytical expression for a scaling factor	140
Appendix E: Effects of bin size on resolution	142
E.1 Introduction	142
E.2 Results	143
E.2.1 Impulse response	143
E.2.2 The system is not invariant	145
E.2.3 The area under the image is affected by the step size	146
E.2.4 The image of a Gaussian is not a Gaussian	146
E.2.5 The resolution depends on <i>the size of the feature</i>	146
E.3 Determining the bin size	148
E.4 Conclusions	149
Bibliography	151
Vita	158

List of Tables

6.1	Reduced chi-squared values resulting from the fits of theory to experiment	74
7.1	Helium autoionizing levels and relevant parameters	91
7.2	Basic kinematic parameters for our experiments	92
7.3	Comparison of calculated and fitted values of q_L	94

List of Figures

2.1	Geometry for an $(e, 2e)$ experiment	5
4.1	Phase shift as a function of energy	23
4.2	Sine and cosine of the phase shift as a function of energy	24
4.3	The ratio of the total transition probability to that of the direct ionization probability	26
5.1	Main components in the vacuum chamber	29
5.2	Photograph of the coplanar configuration of the apparatus	30
5.3	Vacuum system schematic	33
5.4	Electron gun	35
5.5	Faraday cup	36
5.6	Ejected electron spectrometer	39
5.7	Scattered electron spectrometer	40
5.8	PSD image from both spectrometers	44
5.9	Block diagram of timing and signal processing circuitry	45
5.10	Distribution of electron arrival times	47
5.11	Mechanical diagram of turntable modification	50
5.12	Block diagram for the scattered turntable modification	51
5.13	Geometry of the modified apparatus	53
5.14	Photograph of the movable electron gun mount	53
5.15	Aligning the axis of rotatable gun mount and the gun angle	55
5.16	Aligning the gas nozzle	57
5.17	Closeup of the alignment tool	58
5.18	Comparison of ejected angular distributions obtained from coplanar and out-of-plane geometries	59
5.19	Comparison of measured and reported ejected angular distributions	60
6.1	Theoretical calculations - $E_0 = 488$ eV $\theta_{ej} = \pm 90^\circ$	66
6.2	Theoretical calculations - $E_0 = 488$ eV $\theta_{ej} = +75^\circ, -105^\circ$	67
6.3	Theoretical calculations - $E_0 = 150$ eV $\theta_{ej} = \pm 90^\circ$	68
6.4	Theoretical calculations - $E_0 = 150$ eV $\theta_{ej} = +75^\circ, -105^\circ$	69
6.5	Angle convention for coplanar experiments	71
6.6	Comparison of ejected electron counts as a function of scattering angle.	72
6.7	Combining experiments at $E_0 = 150$ eV.	73
6.8	Results - $E_0 = 488$ eV $\theta_{ej} = \pm 90^\circ$	80
6.9	Results - $E_0 = 488$ eV $\theta_{ej} = +75^\circ, -105^\circ$	82
6.10	Results - $E_0 = 150$ eV $\theta_{ej} = \pm 90^\circ$	84
6.11	Results - $E_0 = 150$ eV $\theta_{ej} = +75^\circ, -105^\circ$	86
7.1	Cartoon of a PWBA calculation of the ejected electron angular distribution for direct ionization	92
7.2	Geometry of the apparatus	93
7.3	Out-of-plane results	95

Chapter 1

Introduction

What happens when an atom is hit by a projectile? A large part of atomic physics, and all of the work I will describe, involves answering this very simple question. Of course there are many specific manifestations of this question: e.g. one can consider elastic or inelastic collisions, slow or fast projectiles, as well as different types of projectiles.

The reasons for answering this *question* are as manifold as its various specific manifestations. However, two major reasons are to gain an understanding of (a) collision dynamics and (b) atomic structure. The importance of examining collision dynamics cannot be overstated; such experiments probe our understanding of scattering (and quantum) theory. In fact, it has been stated that “the most important experimental technique in quantum physics is the scattering experiment” [1]. The experiments described in chapters 6 and 7 were performed to test our understanding of scattering theory (at least as it pertains to electrons scattered by helium).

While the main focus of this work is to examine collision dynamics, I have included (in appendix A) a set of experiments we performed that deal with atomic structure (specifically they examined autoionizing resonances in helium). Besides being valuable in their own right, these results have been useful to us for tuning and calibration purposes.

Our work has involved the experimental examination of electron impact single ionization:

$$X + e_0(E_0, \mathbf{k}_0) \longrightarrow X^+ + e_a(E_a, \mathbf{k}_a) + e_b(E_b, \mathbf{k}_b), \quad (1.1)$$

in which an incident electron of energy E_0 (momentum \mathbf{k}_0) ionizes a neutral atom or molecule X , producing a singly charged ion X^+ in the ground or excited state [2], and two outgoing electrons e_a and e_b . For the experiments described here, the energies of the two outgoing electrons are sufficiently different that exchange effects can be ignored, and it is therefore reasonable to label the faster electron as *scattered* and the slower as *ejected*. We can therefore change the labels of the outgoing electrons in equation 1.1:

$$X + e_0(E_0, \mathbf{k}_0) \longrightarrow X^+ + e_{sc}(E_{sc}, \mathbf{k}_{sc}) + e_{ej}(E_{ej}, \mathbf{k}_{ej}) \quad (1.2)$$

where the subscripts *sc* and *ej* refer to the *scattered* and *ejected* electrons respectively.

The target for all of my work has been helium. Helium is in many ways an obvious choice; it is (a) the prototypical multi-electron atom, (b) inexpensive and (c) easy to handle.

How is the title of this work, *Helium ($e, 2e$) coplanar and out-of-plane experiments*, connected to equation 1.2? Helium, as mentioned in the previous paragraph, is the (both literal and figurative) *target* of our experiments (i.e., it is the X in equation 1.2). ($e, 2e$) experiments detect both of the outgoing electrons resulting from electron impact single ionization (i.e., e_a and e_b on the RHS of equation 1.2). In chapter 4, I will explain the details of the ($e, 2e$) technique, for the moment let it suffice to say that an ($e, 2e$) experiment “. . . is a measurement almost at the limit of what is quantum mechanically knowable and its description presents a substantial challenge to theory” [3, pg. ix]. The ($e, 2e$) technique seems to be a method of choice. Finally, the terms *coplanar* and *out-of-plane* refer to the geometric relationship of the trajectories of the three electrons in equation 1.2 (coplanar indicates that all three electron trajectories define a single plane, out-of-plane indicates that they do not).

Conceptually, I have divided this dissertation into three parts. The first part provides background information and starts by providing details of the ($e, 2e$) technique in chapter 2. Following the description of ($e, 2e$) experiments are two chapters on theory; chapter 3 provides some of the basics of scattering theory (and more specifically the Born approximation), while chapter 4 describes autoionization. After this (if not exhaustive, then perhaps exhausting) trip into theory, chapter 5 describes the nuts and bolts of the apparatus used for our experiments.

The second part (consisting of chapters 6 and 7) is the essence of this dissertation; it describes, and provides the results from, our scattering experiments. Chapter 6 is devoted to our coplanar ($e, 2e$) experiments. We present scattered angular distributions of relative triple differential cross sections (TDCSs) for direct ionization of helium by electrons with incident energies 150 eV and 488 eV, and an ejected electron energy 34.5 eV. At both incident energies experiments were carried out for a fixed pair of ejected directions $+90^\circ, -90^\circ$ and a range of scattering angles $-30^\circ \rightarrow +30^\circ$, and also for a fixed pair of ejected directions $+75^\circ, -105^\circ$ and a range of scattering angles $-34^\circ \rightarrow +18^\circ$. This chapter also demonstrates how, by manipulating pairs of datasets, we can test

theory in a more exacting way than with single datasets. Additionally, we compare these experimental results with theoretical calculations performed by the Madison group at the University of Missouri, Rolla. Chapter 7 then details our out-of-plane experiments. These experiments measured ejected electron angular distributions of relative TDCSs for the helium autoionizing levels $(2s^2)^1S$, $(2p^2)^1D$, $(2s2p)^1P$, and for direct ionization using 488 eV incident energy electrons. The scattering angle was 20.5° and the momentum transfer had a magnitude of 2.1 au. It is shown that the results can be described qualitatively by a simple Born approximation calculation in which each autoionizing state adds an L -dependent resonant term to the scattering amplitude.

Finally, the third part consists of the appendices, and presents results that are ancillary to the topic of this dissertation.

Chapter 2

The $(e, 2e)$ technique

An $(e, 2e)$ experiment is “. . . an electron impact ionization measurement in which the kinematics of all the free electrons are completely determined” [4]. The symbology indicates the type of incident particle on the left side of the comma, and the number and type of outgoing particles to the right of the comma, with the implication that the outgoing particles are all detected in coincidence; e.g., an $(e, e\gamma)$ experiment [5] detects an outgoing electron and photon from a reaction where these are the outgoing particles. It can be argued that $(e, 2e)$ experiments are the culmination of efforts to devise techniques to delve into the process of electron impact single ionization. These efforts started with experiments that detected only one of the outgoing electrons, thereby determining total and single differential cross-sections for this process (see section 3.1 for descriptions of various types of cross sections). Starting in the 1930s, experiments that determined the doubly differential cross section were performed (e.g. Hughes and McMillen [6], Bullard and Massey [7], and Hughes and Mann [8]). Experiments examining this process continued to evolve over the years, and a milestone was reached in 1969 when Ehrhardt [9] and Amaldi [10] each independently reported results from experiments where both outgoing electrons were detected in coincidence, i.e., they had performed the first $(e, 2e)$ experiments. (See [11] for a slightly less condensed history of the $(e, 2e)$ technique).

Let us examine the technique more closely. Given the momenta of the two outgoing electrons, and assuming that one knows the momentum of the incident electron, momentum conservation allows one to determine the momentum of the residual ion. This means that the momenta of all independent particles involved in the process are determined; i.e., an $(e, 2e)$ experiment is kinematically complete. It also means that one is able to determine the triple differential cross section (TDCS).

A geometrical representation of an $(e, 2e)$ experiment is shown in figure 2.1. The incident and scattered momenta define the scattering plane. Experiments where the incident and both detected outgoing electrons form a single plane (i.e., ejected electrons are only detected if they have momenta within the scattering plane) are referred to as *coplanar* experiments. Experiments where this is not so (i.e., it is possible to detect ejected electrons having momenta outside of the scattering plane) are referred to as

out-of-plane experiments. The momentum transferred from the incident electron to the atom or molecule is referred to as the *momentum transfer vector* \mathbf{K} , and is simply the difference of the incident and scattered momenta

$$\mathbf{K} = \mathbf{k}_0 - \mathbf{k}_{sc}. \quad (2.1)$$

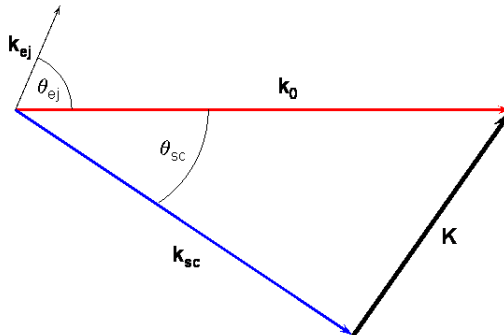


Figure 2.1: Geometry for an $(e, 2e)$ experiment.

In addition to classifying $(e, 2e)$ experiments as being coplanar or out-of-plane, one can also classify them as *symmetric* (meaning that each of the two outgoing electrons have the same energy $E_{sc} = E_{ej}$ and angle relative to the incident direction $\theta_{sc} = \theta_{ej}$) or *asymmetric* (meaning that the energies of the outgoing electrons are different) [12, pg. 25].

An $(e, 2e)$ experiment, being kinematically complete, can be viewed as having five parameters. Three of these parameters are the energies of the incident, scattered, and ejected electrons (E_0 , E_{sc} , and E_{ej} , respectively). The other two parameters are the directions of the scattered, and ejected electrons (\hat{k}_{sc} , and \hat{k}_{ej} , respectively). Since these directions are typically measured with respect to the incident electron direction \hat{k}_0 , the incident direction is (conceptually at least) fixed. The experimenter generally fixes four of these five parameters and varies the remaining one.

So far I have differentiated $(e, 2e)$ experiments by their geometry (e.g., coplanar versus out-of-plane, and symmetric versus asymmetric). One can also categorize them by the goal of the experiment. In general the aim of an $(e, 2e)$ experiment is either to study

the structure of the atom (or molecule) or to study collision dynamics. Structural studies typically use incident energies of at least 1 keV, and (quite often) symmetric geometry. Under these conditions the reaction mechanism is simple enough to be described using the plane wave impulse approximation (PWIA) [11], which allows momentum space wavefunctions of the target to be obtained.

Chapter 3

Electron-atom scattering

There are basically three electron-atom scattering processes:

- *Elastic scattering* where energy is exchanged between the centers-of-mass of the electron and atom only (i.e., neither excitation nor ionization of the atom occurs).
- *Inelastic scattering* where excitation and/or ionization of the atom does occur.
- *Superelastic scattering* where the atom is in an excited state prior to the interaction with the incident electron, and the electron gains energy from the atom (i.e., the atom transitions to a lower excited state, or the ground state, and the excess energy is transferred to the electron). Superelastic scattering is not within the scope of this work and will not be discussed.

But before getting to the specifics of the scattering *process*, let's describe how to *quantify* scattering.

3.1 Cross-section

The likelihood that a collision will take place between a projectile and a target is conveniently described in terms of a cross section. Since all of the experiments presented in this work involve collisions between electrons and helium atoms, the descriptions that follow, although quite general, will be couched in terms of electrons and atoms. Consider a monoenergetic beam of electrons directed at a target. Flux (F) is defined as the number of particles passing through a plane of unit area perpendicular to the direction of travel per unit time. For a monoenergetic beam, all of the incident particles have the same velocity v , and the flux of the beam is:

$$F = n_0 v \tag{3.1}$$

where n_0 is the number of incident particles per unit volume.

We will assume the target is “thin” in the sense that an incident particle will interact with, at most, one atom. The number of electrons scattered per unit time (n_s) by the target atoms will be proportional to the flux of electrons (i.e., the number of “bullets”

per unit area, per unit time), the number of target atoms that are intercepted by the incident beam N , and the total cross section (i.e., apparent size) of each atom σ [13, pg. 118]:

$$n_s = F N \sigma \quad (3.2)$$

We call σ the *total* cross section because the total number of scattered electrons is proportional to it. Knowledge of n_s can be quite valuable, but we have more detailed questions about the scattering process. For instance, we might want to know the number of electrons that will be scattered into some solid angle $d\Omega$. Again we know that this must be proportional to the number of atoms per unit volume, and to the flux. However, we no longer use the total cross section σ , instead we need some quantity that indicates the apparent size of the target with respect to scattering into some specific angle. This quantity is a singly differential cross section (SDCS) $d\sigma/d\Omega$, which obeys:

$$\sigma = \int \frac{d\sigma}{d\Omega} d\Omega \quad (3.3)$$

Using this singly differential cross section the number of scattered electrons per unit time dn_s is simply:

$$dn_s = F N \frac{d\sigma}{d\Omega} d\Omega \quad (3.4)$$

Notice that I referred to $d\sigma/d\Omega$ as *a* SDCS (as opposed to *the* SDCS). The reason is that the cross section can be singly differential with respect to any of the kinematic variables (e.g., for inelastic collisions we could measure the energy E of the scattered electron in which case we are dealing with $d\sigma/dE$ as a SDCS).

We can delve deeper into the scattering process and cross sections as a function of the energy of scattered electron and the solid angle into which it scatters. This is then a double differential cross section (DDCS), which must satisfy:

$$\sigma = \int \frac{d\sigma(\theta)}{dE d\Omega} dE d\Omega \quad (3.5)$$

Again, this is not the only type of DDCS; for instance, if ionization occurs we could look at the angular distribution of the ejected (instead of the scattered) electron.

Looking at equation 1.1 (and recalling momentum and energy conservation) we see that for a given incident electron momentum, the kinematics are fully determined if we know the directions of both outgoing electrons, the energy of one of the outgoing

electrons and the difference in energy between the initial and final atomic states. The cross section that describes this situation must be differential in both outgoing electron directions (i.e., Ω_{ej} and Ω_{sc}), and in the energy of one of the outgoing electrons (i.e., E_{ej} or E_{sc}). In other words, the kinematics are completely determined by the triple differential cross section (TDCS) e.g., $d^3\sigma/dE_{ej}d\Omega_{ej}d\Omega_{sc}$. Going to a higher order differential cross section does not yield any further information. Therefore, for single ionization the TDCS can also be referred to as the fully differential cross section (FDCS). (Of course if the beam of incident electrons is polarized then another kinematic parameter is added, but all of our experiments use unpolarized electrons. It should also be noted that what I refer to as the TDCS is also sometimes referred to as the *five fold differential cross section* $d^5\sigma/dE_{ej}d\Omega_{ej}d\Omega_{sc}$, which is in fact more mathematically precise since each solid angle involves two independent coordinates. However, the term TDCS seems more physically meaningful since we are dealing with three kinematic parameters.)

3.2 Elastic scattering

The work I have performed involves inelastic scattering processes. However, it seems conventional (as well as convenient) to use a discussion of elastic scattering as a lead-in to inelastic scattering. I shall not only be conventional by starting with elastic scattering, but will also base this treatment on the (rather conventional) text by Sakurai [14].

Let us start with the Hamiltonian, which can be expressed as

$$H = H_0 + V,$$

where H_0 is the kinetic energy operator (i.e., the Hamiltonian for the free particle) and V is the scattering potential. For now we will only consider the case of spherically symmetric (time-independent) potentials of limited range, so, using the position of the atom as the origin, V is a function of r only and the Hamiltonian becomes:

$$H = H_0 + V(r) \tag{3.6}$$

Since the Hamiltonian does not depend on time we can use the time-independent Schrödinger equation.

$$(H_0 + V(r)) \psi = E \psi \tag{3.7}$$

or,

$$(H_0 + V(r)) |\psi\rangle = E |\psi\rangle \quad (3.8)$$

Now for the particular case where $V(r) = 0$ the solution is that for a free particle:

$$H_0 |\phi\rangle = E |\phi\rangle \quad (3.9)$$

Therefore, the solution of 3.8 must satisfy $|\psi\rangle \rightarrow |\phi\rangle$ as $V \rightarrow 0$. From 3.9 we see that $(E - H_0) |\phi\rangle = 0$. Using this observation we manipulate 3.8 by adding 0 to both sides of the equation:

$$\begin{aligned} E |\psi\rangle + 0 &= (H_0 + V(r)) |\psi\rangle + (E - H_0) |\phi\rangle \\ (E - H_0) |\psi\rangle &= V(r) |\psi\rangle + (E - H_0) |\phi\rangle \\ |\psi\rangle &= \frac{V(r)}{E - H_0} |\psi\rangle + |\phi\rangle \end{aligned}$$

This seems a reasonable prescription for $|\psi\rangle$ except for the fact that $\frac{V(r)}{E - H_0}$ may be singular. This is remedied by making E slightly complex:

$$|\psi^\pm\rangle = \frac{V(r)}{E - H_0 \pm i\epsilon} |\psi^\pm\rangle + |\phi\rangle \quad (3.10)$$

Equation 3.10 is the Lippmann-Schwinger equation, which is in general intractable, so one or more approximations are needed to evaluate it.

The first one we will apply is the Born approximation. The (1st order) Born approximation simply suggests that if V acts as a small perturbation, then it makes sense to substitute $|\phi\rangle$ for $|\psi^\pm\rangle$ on the RHS of equation 3.10. To find arbitrarily high orders of the approximation we start by defining an operator T such that $T|\phi\rangle = V|\psi^\pm\rangle$ [14, pg 389]. Operating on equation 3.10 with the potential operator V

$$V|\psi\rangle = V|\phi\rangle + V \frac{1}{E - H_0 \pm i\epsilon} V|\psi\rangle \quad (3.11)$$

and applying the substitution $T|\phi\rangle = V|\psi^\pm\rangle$ yields

$$T|\phi\rangle = V|\phi\rangle + V \frac{1}{E - H_0 \pm i\epsilon} T|\phi\rangle. \quad (3.12)$$

We can iteratively apply this relation to itself:

$$\begin{aligned}
T|\phi\rangle &= V|\phi\rangle + V\frac{1}{E - H_0 \pm i\epsilon}T|\phi\rangle \\
&= V|\phi\rangle + V\frac{1}{E - H_0 \pm i\epsilon}V|\phi\rangle \\
&\quad + V\frac{1}{E - H_0 \pm i\epsilon}V\frac{1}{E - H_0 \pm i\epsilon}T|\phi\rangle \\
&= V|\phi\rangle + V\frac{1}{E - H_0 \pm i\epsilon}V|\phi\rangle \\
&\quad + V\frac{1}{E - H_0 \pm i\epsilon}V\frac{1}{E - H_0 \pm i\epsilon}V|\phi\rangle + \dots
\end{aligned} \tag{3.13}$$

If we now “undo” the substitution $T|\phi\rangle = V|\psi^\pm\rangle$ we get the result

$$\begin{aligned}
|\psi^\pm\rangle &= |\phi\rangle + \frac{1}{E - H_0 \pm i\epsilon}V|\phi\rangle \\
&\quad + \frac{1}{E - H_0 \pm i\epsilon}V\frac{1}{E - H_0 \pm i\epsilon}V|\phi\rangle + \dots
\end{aligned} \tag{3.14}$$

Keeping only terms up to 1st order in V on the RHS of equation 3.14 (i.e., applying the 1st order Born approximation to equation 3.10) and then going to a spatial representation yields:

$$\begin{aligned}
|\psi^\pm\rangle &= \frac{V}{E - H_0 \pm i\epsilon}|\phi\rangle + |\phi\rangle \\
\langle\mathbf{r}|\psi^\pm\rangle &= \langle\mathbf{r}|\phi\rangle + \langle\mathbf{r}|\frac{V}{E - H_0 \pm i\epsilon}|\phi\rangle
\end{aligned} \tag{3.15}$$

A few definitions are in order before we evaluate equation 3.15. The position vectors \mathbf{r} and \mathbf{r}' refer to the position of the observer and the scatterer respectively. The wave vectors \mathbf{k} and \mathbf{k}' are the vectors for the incident and scattered particles respectively. Note that for elastic scattering, $|\mathbf{k}| = |\mathbf{k}'|$. The magnitude of the wave vector and the energy are related by $E = \hbar^2 k^2 / 2m$. The spatial representation of a free wave is [14, p. 384]:

$$\langle\mathbf{r}|\mathbf{k}\rangle = \frac{e^{i\mathbf{k}\cdot\mathbf{r}}}{(2\pi)^{3/2}} \tag{3.16}$$

Now let us define the Green’s operator and its spatial representation [15]:

$$G^\pm(E) = \frac{1}{E - H_0 \pm i\epsilon} \tag{3.17}$$

$$G^\pm(\mathbf{r}, \mathbf{r}') = \frac{\hbar^2}{2m} \langle\mathbf{r}|\frac{1}{E - H_0 \pm i\epsilon}|\mathbf{r}'\rangle \tag{3.18}$$

$$= \frac{1}{4\pi} \frac{e^{\pm ik|\mathbf{r}-\mathbf{r}'|}}{|\mathbf{r} - \mathbf{r}'|} \tag{3.19}$$

It will prove useful to know $G^\pm(\mathbf{r}, \mathbf{r}')$ for the case where $r \gg r'$. Using the expansion:

$$|\mathbf{r} - \mathbf{r}'| \simeq r - \hat{\mathbf{r}} \cdot \mathbf{r}' \quad (3.20)$$

in equation 3.19 yields:

$$G^\pm(\mathbf{r}, \mathbf{r}') \simeq \frac{1}{4\pi} \frac{e^{\pm ikr}}{r} e^{\mp i\mathbf{k}' \cdot \mathbf{r}'} \quad (3.21)$$

(where $\mathbf{k}' = k\hat{\mathbf{r}}$).

Now, proceeding to evaluate equation 3.15 we look at the second term on the RHS:

$$\begin{aligned} \langle \mathbf{r} | \frac{V}{E - H_0 \pm i\epsilon} | \phi \rangle &= \int d^3 r' \langle \mathbf{r} | \frac{1}{E - H_0 \pm i\epsilon} | \mathbf{r}' \rangle \langle \mathbf{r}' | V | \phi \rangle \\ &= \int d^3 r' \frac{2m}{\hbar^2} G^\pm(\mathbf{r}, \mathbf{r}') \langle \mathbf{r}' | V | \phi \rangle \\ &= \frac{2m}{\hbar^2} \int d^3 r' G^\pm(\mathbf{r}, \mathbf{r}') V(r') \langle \mathbf{r}' | \phi \rangle \end{aligned} \quad (3.22)$$

To obtain equation 3.22 I used the relationship:

$$\begin{aligned} \langle \mathbf{r}' | V | \phi \rangle &= \int d^3 r'' \langle \mathbf{r}' | V | \mathbf{r}'' \rangle \langle \mathbf{r}'' | \phi \rangle \\ &= \int d^3 r'' V(r'') \delta^{(3)}(\mathbf{r}'' - \mathbf{r}') \langle \mathbf{r}'' | \phi \rangle \\ &= V(r') \langle \mathbf{r}' | \phi \rangle \end{aligned} \quad (3.23)$$

which is valid for time-independent spherically symmetric potentials. Substituting equation 3.22 into equation 3.15 yields:

$$\langle \mathbf{r} | \psi^\pm \rangle = \langle \mathbf{r} | \phi \rangle + \frac{2m}{\hbar^2} \int d^3 r' G^\pm(\mathbf{r}, \mathbf{r}') V(r') \langle \mathbf{r}' | \phi \rangle$$

In this equation, the vector \mathbf{r}' represents the source of the scattering potential, which for our purposes is of limited range (specifically I am restricting this discussion to potentials that drop off faster than $1/r$, although the Born approximation can also be applied to the Coulomb potential as well). The vector \mathbf{r} is the position vector for the observer. Compared to the effective range of the potential, the observer is always far away, so we are dealing with the situation $r \gg r'$, therefore equation 3.21 is applicable:

$$\begin{aligned} \langle \mathbf{r} | \psi^\pm \rangle &= \langle \mathbf{r} | \phi \rangle + \frac{2m}{\hbar^2} \int d^3 r' \frac{1}{4\pi} \frac{e^{\pm ikr}}{r} e^{\mp i\mathbf{k}' \cdot \mathbf{r}'} V(r') \langle \mathbf{r}' | \phi \rangle \\ &= \langle \mathbf{r} | \phi \rangle + \frac{2m}{\hbar^2} \frac{1}{4\pi} \frac{e^{\pm ikr}}{r} \int d^3 r' e^{\mp i\mathbf{k}' \cdot \mathbf{r}'} V(r') \langle \mathbf{r}' | \phi \rangle \end{aligned} \quad (3.24)$$

Noting that $\langle \mathbf{r} | \phi \rangle = e^{i\mathbf{k}\cdot\mathbf{r}} / \hbar^2 (2\pi)^{3/2}$ we see that the wave function

$$\psi^\pm(\mathbf{r}) \approx \frac{e^{i\mathbf{k}\cdot\mathbf{r}}}{\hbar^2 (2\pi)^{3/2}} + \frac{2m}{\hbar^2} \frac{1}{4\pi} \frac{e^{\pm ikr}}{r} \int d^3 r' e^{\mp i\mathbf{k}'\cdot\mathbf{r}'} V(r') \langle \mathbf{r}' | \phi \rangle \quad (3.25)$$

is expressed as an incoming plane wave and a spherical wave (outgoing for e^{+ikr} and incoming for e^{-ikr}) multiplied by an amplitude:

$$f = \frac{2m}{\hbar^2} \frac{1}{4\pi} \int d^3 r' e^{\mp i\mathbf{k}'\cdot\mathbf{r}'} V(r') \langle \mathbf{r}' | \phi \rangle \quad (3.26)$$

We are concerned with the case where there is an incoming (incident) plane wave and outgoing spherical wave; i.e., we want $\psi^+(\mathbf{r})$. The scattering amplitude f is then:

$$\begin{aligned} f &= \frac{2m}{\hbar^2} \frac{1}{4\pi} \int d^3 r' e^{-i\mathbf{k}'\cdot\mathbf{r}'} V(r') \langle \mathbf{r}' | \phi \rangle \\ &= \frac{2m}{\hbar^2} \frac{1}{4\pi} (2\pi)^{3/2} \int d^3 r' \langle \phi | \mathbf{r}' \rangle \langle \mathbf{r}' | V | \mathbf{r}' \rangle \langle \mathbf{r}' | \phi \rangle \\ &= \frac{2m}{\hbar^2} \frac{1}{4\pi} (2\pi)^{3/2} \langle \phi' | V | \phi \rangle \\ &= \frac{2m}{4\pi} (2\pi)^{3/2} \langle \mathbf{k}' | V | \mathbf{k} \rangle \end{aligned} \quad (3.27)$$

The probability of there being an outgoing spherical wave (i.e., the probability that scattering occurs) is proportional to the square of the scattering amplitude $|f|^2$.

3.3 Inelastic scattering

For inelastic scattering the target atom becomes excited (and/or ionized) and the magnitude of the scattered electron's momentum is in general less than that for the incident electron; i.e., $|\mathbf{k}'| < |\mathbf{k}|$. Since we must take into account the excitation (possibly to a continuum state) of the target atom we can no longer simply use a plane wave for the initial state. In other words, we must now take into account the structure of the target atom. Accordingly, we use the direct product of the incident plane wave and the initial atomic state; likewise for the final state we will use the direct product of the scattered plane wave and the final atomic state:

$$|\mathbf{k}\rangle \longrightarrow |\mathbf{k}, 0\rangle \quad (3.28)$$

$$|\mathbf{k}'\rangle \longrightarrow |\mathbf{k}', n\rangle \quad (3.29)$$

Let us now consider the scattering potential in more detail. For a multielectron atom the interaction potential (expressed in atomic units) takes the form [14, eqn. 7.12.7]:

$$V = -\frac{Z}{r} + \sum_i \frac{1}{|\mathbf{r} - \mathbf{r}_i|} \quad (3.30)$$

$$= V_1 + V_2 \quad (3.31)$$

$$V_1 = -\frac{Z}{r} \quad (3.32)$$

$$V_2 = \sum_i \frac{1}{|\mathbf{r} - \mathbf{r}_i|} \quad (3.33)$$

where \mathbf{r} is the position vector of the incident (or scattered) electron, and $\{\mathbf{r}_i\}$ is the set of vectors for the atomic electrons.

Looking at equation 3.27 and our initial and final states (equations 3.28, and 3.29) we see that in order to determine the scattering amplitude

$$f = \frac{2m}{4\pi} (2\pi)^{3/2} \langle \mathbf{k}', n | V | \mathbf{k}, 0 \rangle, \quad (3.34)$$

we need to evaluate $\langle \mathbf{k}', n | V | \mathbf{k}, 0 \rangle$. Let's split the potential into two parts as shown in equation 3.31 and consider $\langle \mathbf{k}', n | V_1 | \mathbf{k}, 0 \rangle$:

$$\langle \mathbf{k}', n | V_1 | \mathbf{k}, 0 \rangle = \int d^3r d^3r' \langle \mathbf{k}', n | \mathbf{r}' \rangle \langle \mathbf{r}' | V_1 | \mathbf{r} \rangle \langle \mathbf{r} | \mathbf{k}, 0 \rangle$$

Note that $\langle \mathbf{r}' | V_1 | \mathbf{r} \rangle = \delta^{(3)}(\mathbf{r}' - \mathbf{r}) V_1(r)$, and that the matrix element can be expressed as:

$$\begin{aligned} \langle \mathbf{k}', n | V_1 | \mathbf{k}, 0 \rangle &= \int d^3r d^3r' \langle \mathbf{k}', n | \mathbf{r}' \rangle \delta^{(3)}(\mathbf{r}' - \mathbf{r}) V_1(r) \langle \mathbf{r} | \mathbf{k}, 0 \rangle \\ &= \frac{1}{(2\pi)^3} \int d^3r e^{i(\mathbf{k}-\mathbf{k}') \cdot \mathbf{r}} V_1(r) \langle n | 0 \rangle \\ &= \frac{1}{(2\pi)^3} \int d^3r e^{i(\mathbf{k}-\mathbf{k}') \cdot \mathbf{r}} V_1(r) \delta_{n,0} \end{aligned} \quad (3.35)$$

Since this matrix element is non-zero only if the initial and final atomic states are the same, it only contributes to the cross section for elastic scattering. The momentum transfer vector \mathbf{K} was given by equation 2.1; expressed using \mathbf{k} and \mathbf{k}' it is:

$$\mathbf{K} = \mathbf{k} - \mathbf{k}' \quad (3.36)$$

Without loss of generality we can use the momentum transfer direction as our quantization axis (i.e., set $\hat{z} = \hat{K}$); therefore $e^{i(\mathbf{k}-\mathbf{k}') \cdot \mathbf{r}} = e^{iKr \cos \theta}$ and equation 3.35 can be

written:

$$\langle \mathbf{k}', 0 | V_1 | \mathbf{k}, 0 \rangle = \frac{1}{(2\pi)^3} \int d^3r e^{iK r \cos \theta} V_1(r) \quad (3.37)$$

and we carry out the integration over the angular components:

$$\begin{aligned} \langle \mathbf{k}', 0 | V_1 | \mathbf{k}, 0 \rangle &= \frac{1}{(2\pi)^3} \int dr r^2 V_1(r) \int \sin \theta d\theta d\phi e^{iK r \cos \theta} \\ &= \frac{1}{(2\pi)^3} \int dr r^2 V_1(r) \frac{2\pi}{iK r} (e^{iK r} - e^{-iK r}) \\ &= \frac{1}{2\pi^2} \frac{1}{K} \int dr r V_1(r) \sin(K r) \end{aligned}$$

We now substitute the explicit expression for $V_1(r)$ and complete the integration:

$$\begin{aligned} \langle \mathbf{k}', 0 | V_1 | \mathbf{k}, 0 \rangle &= -\frac{1}{2\pi^2} \frac{Z}{K} \int dr \sin(K r) \\ &= -\frac{1}{2\pi^2} \frac{Z}{K^2} \\ \langle \mathbf{k}', n | V_1 | \mathbf{k}, 0 \rangle &= -\frac{1}{2\pi^2} \frac{Z}{K^2} \delta_{n,0} \end{aligned} \quad (3.38)$$

Next we evaluate $\langle \mathbf{k}', n | V_2 | \mathbf{k}, 0 \rangle$:

$$\begin{aligned} \langle \mathbf{k}', n | V_2 | \mathbf{k}, 0 \rangle &= \int d^3r d^3r' \langle \mathbf{k}', n | \mathbf{r}' \rangle \langle \mathbf{r}' | \sum_i \frac{1}{|\mathbf{r} - \mathbf{r}_i|} | \mathbf{r} \rangle \langle \mathbf{r} | \mathbf{k}, 0 \rangle \\ &= \frac{1}{(2\pi)^3} \int d^3r \left\langle n \left| e^{i\mathbf{K} \cdot \mathbf{r}} \sum_i \frac{1}{|\mathbf{r} - \mathbf{r}_i|} \right| 0 \right\rangle \\ &= \frac{1}{(2\pi)^3} \left\langle n \left| \sum_i \int d^3r e^{i\mathbf{K} \cdot \mathbf{r}} \frac{1}{|\mathbf{r} - \mathbf{r}_i|} \right| 0 \right\rangle \end{aligned} \quad (3.39)$$

The integral is evaluated by shifting the coordinate variables $\mathbf{x} \rightarrow \mathbf{x} + \mathbf{x}_i$ [14, p. 431]:

$$\begin{aligned} \int d^3r e^{i\mathbf{K} \cdot \mathbf{r}} \frac{1}{|\mathbf{r} - \mathbf{r}_i|} &= \int d^3r e^{i\mathbf{K} \cdot (\mathbf{r} + \mathbf{r}_i)} \frac{1}{|\mathbf{r}|} \\ &= \frac{4\pi}{K^2} e^{i\mathbf{K} \cdot \mathbf{r}_i} \end{aligned} \quad (3.40)$$

Substituting equation 3.40 into equation 3.39 yields:

$$\langle \mathbf{k}', n | V_2 | \mathbf{k}, 0 \rangle = \frac{1}{2\pi^2} \frac{1}{K^2} \sum_i \langle n | e^{i\mathbf{K} \cdot \mathbf{r}_i} | 0 \rangle \quad (3.41)$$

Combining equations 3.34, 3.38 and 3.41 yields the first Born amplitude

$$f = \frac{2m}{(2\pi)^{3/2}} \frac{1}{K^2} \left(Z \delta_{n,0} + \sum_i \langle n | e^{i\mathbf{K} \cdot \mathbf{r}_i} | 0 \rangle \right),$$

and single differential cross section (cf. [14, eqn. 7.12.5])

$$\begin{aligned} \frac{d\sigma}{d\Omega_{sc}} &= \frac{k_{sc}}{k_0} |f|^2 \\ &= \frac{k_{sc}}{k_0} \frac{4m^2}{(2\pi)^3} \frac{1}{K^4} \left| Z \delta_{n,0} + \sum_i \langle n | e^{i\mathbf{K}\cdot\mathbf{r}_i} | 0 \rangle \right|^2. \end{aligned} \quad (3.42)$$

(The angular dependence arises from the momentum transfer direction \hat{K}). For the case of ionization the final atomic state $\langle n |$ is a direct product of the wave functions for a free electron and the ion, with the TDCS given by [16, eqn. 2]):

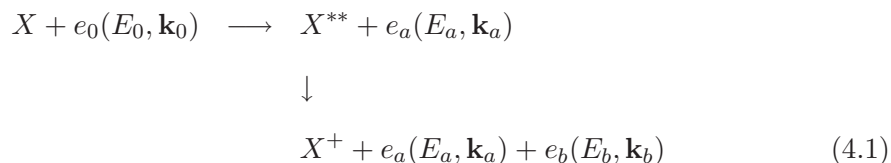
$$\frac{d^3\sigma}{dE d\Omega_{ej} d\Omega_{sc}} = \frac{k_{sc}}{k_0} |f|^2 \quad (3.43)$$

(as for most of this work, exchange effects have been ignored and the two outgoing electrons are assumed to have a difference in energy large enough that one can identify the faster electron as being the scattered electron and the slower one as being the ejected electron).

Chapter 4

Autoionization

Autoionization is a process that occurs when an atom or molecule is excited to a bound state that lies within the continuum. Once in this excited state it becomes possible for the atom or molecule to *autoionize*; i.e., without any further external influence an electron in the bound state may transition to a continuum state. All of the helium doubly excited states lie within the continuum and can lead to autoionization. Looking at this as a two step process, with an electron as the incident particle, autoionization can be expressed as:



Equation 4.1 describes an incident electron with energy E_0 impacting an atom (X) and causing the atom to become doubly excited. This process has imparted to the atom an amount of energy greater than the ionization threshold, and the atom subsequently ionizes. Naively one might assume that this process would result in some sharp, symmetric resonance superimposed on the continuum (e.g., when plotted as cross-section versus scattered energy for a fixed incident energy). However, this is not generally the case. The explanation for this was first proposed by Fano [17], and is the result of interference between direct ionization and autoionization.

Most of the treatment of autoionization I will present closely follows that of Cowan [18]. We will start by considering the case of a single continuum (which is suitable for photoionization) and then make the necessary modifications to account for multiple continua (as is required for electron impact ionization).

Let us suppose that there is a discrete state (e.g., a doubly excited state), the energy of which lies within the energy range of the continuum states $\varepsilon\ell$. This discrete state has the wavefunction φ and the (diagonal) matrix element:

$$\langle \varphi | H | \varphi \rangle = \varepsilon_\varphi \quad (4.2)$$

and the continuum state has the wavefunction ψ_ε and (diagonal) matrix element:

$$\langle \psi_{\varepsilon'} | H | \psi_\varepsilon \rangle = \varepsilon \delta(\varepsilon - \varepsilon') \quad (4.3)$$

The interaction between the two states can be expressed as:

$$\langle \varphi | H | \psi_\varepsilon \rangle = V_\varepsilon \quad (4.4)$$

If there is no interaction between the discrete and continuum states (i.e., $V_\varepsilon = 0$), the probability of absorption as a function of ε is the sum of the probabilities of absorption for the discrete and continuum states. However if there is an interaction between the discrete and continuum states (i.e., $V_\varepsilon \neq 0$ and a reaction such as that in equation 4.1 is possible) then the probability of absorption as a function of ε is the absolute square of the sum of the *amplitudes* (as opposed to the probabilities) of absorption for the discrete and continuum states.

Let us suppose that there is a wide separation in energy between the discrete state φ and any other discrete states. Then the energy eigenfunctions Ψ^ε (satisfying the time independent Schrödinger equation [TISE] $H \Psi^\varepsilon = \varepsilon \Psi^\varepsilon$) can be expressed as a superposition of the discrete state φ and a range of the continuum states:

$$\Psi^\varepsilon = a^\varepsilon \varphi + \int b_{\varepsilon'}^\varepsilon \psi_{\varepsilon'} d\varepsilon' \quad (4.5)$$

To find the mixing coefficients, a^ε and $b_{\varepsilon'}^\varepsilon$, we will substitute equation 4.5 into the TISE and left multiply by φ :

$$\begin{aligned} a^\varepsilon \langle \varphi | H | \varphi \rangle + \int b_{\varepsilon'}^\varepsilon \langle \varphi | H | \psi_{\varepsilon'} \rangle d\varepsilon' &= \varepsilon a^\varepsilon \langle \varphi | \varphi \rangle + \varepsilon \int b_{\varepsilon'}^\varepsilon \langle \varphi | \psi_{\varepsilon'} \rangle d\varepsilon' \\ \varepsilon_\varphi a^\varepsilon + \int b_{\varepsilon'}^\varepsilon V_{\varepsilon'} d\varepsilon' &= \varepsilon a^\varepsilon \end{aligned} \quad (4.6)$$

We now repeat the process, but left multiply by $\psi_{\varepsilon''}$ instead of φ :

$$\begin{aligned} a^\varepsilon \langle \psi_{\varepsilon''} | H | \varphi \rangle + \int b_{\varepsilon'}^\varepsilon \langle \psi_{\varepsilon''} | H | \psi_{\varepsilon'} \rangle d\varepsilon' &= \varepsilon a^\varepsilon \langle \psi_{\varepsilon''} | \varphi \rangle + \varepsilon \int b_{\varepsilon'}^\varepsilon \langle \psi_{\varepsilon''} | \psi_{\varepsilon'} \rangle d\varepsilon' \\ V_{\varepsilon''} a^\varepsilon + \int b_{\varepsilon'}^\varepsilon \varepsilon' \delta(\varepsilon'' - \varepsilon') d\varepsilon' &= \varepsilon \int b_{\varepsilon'}^\varepsilon \delta(\varepsilon'' - \varepsilon') d\varepsilon' \\ V_{\varepsilon''} a^\varepsilon + \varepsilon'' b_{\varepsilon''}^\varepsilon &= \varepsilon b_{\varepsilon''}^\varepsilon \\ V_{\varepsilon'} a^\varepsilon + \varepsilon' b_{\varepsilon'}^\varepsilon &= \varepsilon b_{\varepsilon'}^\varepsilon \end{aligned} \quad (4.7)$$

(note that a change of notation from ε'' to ε' has been done in the last step of equation 4.7). Solving for $b_{\varepsilon'}^{\varepsilon}$, yields:

$$b_{\varepsilon'}^{\varepsilon} = \frac{1}{\varepsilon - \varepsilon'} V_{\varepsilon'} a^{\varepsilon} \quad (4.8)$$

which is not continuous for $\varepsilon = \varepsilon'$. This presents a problem since the wavefunction (equation 4.5) typically includes this very case, therefore equation 4.8 is not complete for our purpose. To remedy this we note that $b_{\varepsilon'}^{\varepsilon}$ appears within an integral, and break the integral into two parts. The first has limits that do not include the vicinity around $\varepsilon = \varepsilon'$; this is the *principal part of the integral*, defined for our purposes as:

$$\mathcal{P} \int_{\varepsilon_1}^{\varepsilon_2} \frac{f(\varepsilon')}{\varepsilon - \varepsilon'} d\varepsilon' = \lim_{\Delta \rightarrow 0} \left[\int_{\varepsilon_1}^{\varepsilon - \Delta} + \int_{\varepsilon + \Delta}^{\varepsilon_2} \right] \frac{f(\varepsilon')}{\varepsilon - \varepsilon'} d\varepsilon' \quad (4.9)$$

With $f(\varepsilon') = V_{\varepsilon'} a^{\varepsilon}$. For the second part we integrate about $\varepsilon = \varepsilon'$, but replace $b_{\varepsilon'}^{\varepsilon}$ with, essentially, a delta function:

$$\lim_{\varepsilon' \rightarrow \varepsilon} b_{\varepsilon'}^{\varepsilon} = \pi \eta(\varepsilon) \delta(\varepsilon - \varepsilon') V_{\varepsilon'} a^{\varepsilon} \quad (4.10)$$

(the meaning of $\eta(\varepsilon)$ shall be discussed shortly). Expressed succinctly, we say:

$$b_{\varepsilon'}^{\varepsilon} = \left(\frac{1}{\varepsilon - \varepsilon'} + \pi \eta(\varepsilon) \delta(\varepsilon - \varepsilon') \right) V_{\varepsilon'} a^{\varepsilon} \quad (4.11)$$

with the understanding that integration of the first term will only be over the principal part (equation 4.9). Although $b_{\varepsilon'}^{\varepsilon}$ is not formally a function (since it includes $\delta(\varepsilon - \varepsilon')$) this representation is still appropriate since $b_{\varepsilon'}^{\varepsilon}$ appears within an integral expression.

Substituting equation 4.11 into equation 4.6 yields:

$$\begin{aligned} \varepsilon_{\varphi} a^{\varepsilon} + a^{\varepsilon} \mathcal{P} \int \frac{V_{\varepsilon'}^2}{\varepsilon - \varepsilon'} d\varepsilon' + \pi \eta(\varepsilon) V_{\varepsilon}^2 a^{\varepsilon} &= \varepsilon a^{\varepsilon} \\ \varepsilon_{\varphi} + \mathcal{P} \int \frac{V_{\varepsilon'}^2}{\varepsilon - \varepsilon'} d\varepsilon' + \pi \eta(\varepsilon) V_{\varepsilon}^2 &= \varepsilon \\ \eta(\varepsilon) &= \frac{\varepsilon - \varepsilon_{\varphi} - F(\varepsilon)}{\pi V_{\varepsilon}^2} \end{aligned} \quad (4.12)$$

$$F(\varepsilon) = \mathcal{P} \int \frac{V_{\varepsilon'}^2}{\varepsilon - \varepsilon'} d\varepsilon' \quad (4.13)$$

If we express $\psi_{\varepsilon'}$ with wave functions having asymptotic behaviour proportional to $\sin[k(\varepsilon')r + \delta]$, then the ‘‘continuum’’ part of Ψ^{ε} (equation 4.5) can be expressed as (see [17, eqn. 5]):

$$\int b_{\varepsilon'}^{\varepsilon} \psi_{\varepsilon'} d\varepsilon' \propto \sin[k(\varepsilon)r + \delta + \Delta] \quad (4.14)$$

$$\Delta = -\arctan \left[\frac{1}{\eta(\varepsilon)} \right] \quad (4.15)$$

We see that Δ represents a phase shift, and is dependent on $\eta(\varepsilon)$. This phase shift varies sharply as ε passes through the resonance at $\varepsilon_\varphi + F(\varepsilon)$. In fact Δ changes by $\sim \pi$ as ε varies from $\varepsilon_\varphi + F(\varepsilon) - V_\varepsilon^2 \rightarrow \varepsilon_\varphi + F(\varepsilon) + V_\varepsilon^2$; i.e., as ε traverses an interval of $\sim V_\varepsilon^2$ about the resonance. The quantity $F(\varepsilon)$ therefore represents a shift of the resonance position with respect to ε_φ [17, pg. 1867]. With this interpretation of $F(\varepsilon)$, the function $\eta(\varepsilon)$ “... is essentially the energy displacement from the *perturbed* position of the discrete level, measured in units of πV_ε^2 ” [18].

Having found the coefficients $b_\varepsilon^\varepsilon$, in terms of the coefficient a^ε we now need to find a^ε . We start to do this by normalizing Ψ^ε (equation 4.5) as per a continuum wavefunction:

$$\begin{aligned} \langle \Psi^\varepsilon | \Psi^\varepsilon \rangle &= \delta(\bar{\varepsilon} - \varepsilon) \\ &= a^{\bar{\varepsilon}} a^\varepsilon \langle \varphi | \varphi \rangle + \int \int b_{\varepsilon''}^{\bar{\varepsilon}} b_{\varepsilon'}^\varepsilon \langle \psi_{\varepsilon''} | \psi_{\varepsilon'} \rangle d\varepsilon' d\varepsilon'' \\ &= a^{\bar{\varepsilon}} a^\varepsilon + \int b_{\varepsilon'}^{\bar{\varepsilon}} b_{\varepsilon'}^\varepsilon d\varepsilon' \end{aligned} \quad (4.16)$$

It has been shown [17] that the second term on the right hand side can, after substituting our expression for $b_{\varepsilon'}^\varepsilon$ (equation 4.11), be expressed as:

$$\int b_{\varepsilon'}^{\bar{\varepsilon}} b_{\varepsilon'}^\varepsilon d\varepsilon' = (\pi a^\varepsilon V_\varepsilon)^2 [\eta(\varepsilon)^2 + 1] \delta(\bar{\varepsilon} - \varepsilon) - a^{\bar{\varepsilon}} a^\varepsilon \quad (4.17)$$

which, when substituted into equation 4.16 yields:

$$\begin{aligned} \delta(\bar{\varepsilon} - \varepsilon) &= a^{\bar{\varepsilon}} a^\varepsilon + (\pi a^\varepsilon V_\varepsilon)^2 [\eta(\varepsilon)^2 + 1] \delta(\bar{\varepsilon} - \varepsilon) - a^{\bar{\varepsilon}} a^\varepsilon \\ 1 &= (\pi a^\varepsilon V_\varepsilon)^2 [\eta(\varepsilon)^2 + 1] \\ (a^\varepsilon)^2 &= \frac{1}{(\pi V_\varepsilon)^2 [\eta(\varepsilon)^2 + 1]} \end{aligned} \quad (4.18)$$

$$= \frac{V_\varepsilon^2}{[\varepsilon - \varepsilon_\varphi - F(\varepsilon)]^2 + \pi^2 V_\varepsilon^4} \quad (4.19)$$

Substituting equation 4.11 into the expression for Ψ^ε (equation 4.5) yields:

$$\begin{aligned} \Psi^\varepsilon &= a^\varepsilon \varphi + a^\varepsilon \pi \eta(\varepsilon) V_\varepsilon \psi_\varepsilon + a^\varepsilon \mathcal{P} \int \frac{V_{\varepsilon'} \psi_{\varepsilon'}}{\varepsilon - \varepsilon'} d\varepsilon' \\ &= a^\varepsilon \varphi + \frac{a^\varepsilon}{V_\varepsilon} [\varepsilon - \varepsilon_\varphi - F(\varepsilon)] \psi_\varepsilon + a^\varepsilon \mathcal{P} \int \frac{V_{\varepsilon'} \psi_{\varepsilon'}}{\varepsilon - \varepsilon'} d\varepsilon' \end{aligned} \quad (4.20)$$

Since a wavefunction is in general only defined to within an arbitrary phase, and $\Psi^\varepsilon \propto a^\varepsilon$, we can choose either sign when taking the square root of a^ε (equation 4.19). Choosing

the positive root yields:

$$a^\varepsilon = \frac{V_\varepsilon}{\left([\varepsilon - \varepsilon_\varphi - F(\varepsilon)]^2 + \pi^2 V_\varepsilon^4\right)^{1/2}} \quad (4.21)$$

which is the final piece in our analytical expression of Ψ^ε . To make use of this however, we still need to do more math.

We will now depart from Cowan's treatment of the subject and take up the treatment in [17]. We return to the assumption that the asymptotic behaviour of $\psi_{\varepsilon'}$ is proportional to $\sin[k(\varepsilon')r + \delta]$. Using equation 4.15 we can express $\eta(\varepsilon)$ in terms of the phase shift:

$$\eta(\varepsilon) = -\frac{\cos \Delta}{\sin \Delta} \quad (4.22)$$

Substituting this into equation 4.18 yields:

$$\begin{aligned} (a^\varepsilon)^2 &= \frac{1}{\pi^2 V_\varepsilon^2 \left[1 + \frac{\cos^2 \Delta}{\sin^2 \Delta}\right]} \\ &= \frac{\sin^2 \Delta}{\pi^2 V_\varepsilon^2} \\ a^\varepsilon &= \frac{\sin \Delta}{\pi V_\varepsilon} \end{aligned} \quad (4.23)$$

And substituting equations 4.22 and 4.23 into equation 4.11 yields:

$$\begin{aligned} b_{\varepsilon'}^\varepsilon &= \left(\frac{1}{\varepsilon - \varepsilon'} + \pi \left[-\frac{\cos \Delta}{\sin \Delta}\right] \delta(\varepsilon - \varepsilon')\right) V_{\varepsilon'} \frac{\sin \Delta}{\pi V_\varepsilon} \\ &= \frac{\sin \Delta}{(\varepsilon - \varepsilon')} \frac{V_{\varepsilon'}}{\pi V_\varepsilon} - \cos \Delta \delta(\varepsilon - \varepsilon') \frac{V_{\varepsilon'}}{V_\varepsilon} \\ &= \frac{\sin \Delta}{(\varepsilon - \varepsilon')} \frac{V_{\varepsilon'}}{\pi V_\varepsilon} - \cos \Delta \delta(\varepsilon - \varepsilon') \end{aligned} \quad (4.24)$$

We are now in the position where we can examine an arbitrary transition matrix involving a final state Ψ^ε , i.e., $\langle \Psi^\varepsilon | T | i \rangle$.

$$\begin{aligned} \langle \Psi^\varepsilon | T | i \rangle &= a^\varepsilon \langle \varphi | T | i \rangle + \int b_{\varepsilon'}^\varepsilon \langle \psi_{\varepsilon'} | T | i \rangle d\varepsilon' \\ &= \frac{\sin \Delta}{\pi V_\varepsilon^*} \langle \varphi | T | i \rangle + \frac{\sin \Delta}{\pi V_\varepsilon^*} \mathcal{P} \int \frac{V_{\varepsilon'}^* \langle \psi_{\varepsilon'} | T | i \rangle}{(\varepsilon - \varepsilon')} d\varepsilon' - \cos \Delta \langle \psi_\varepsilon | T | i \rangle \\ &= \frac{\sin \Delta}{\pi V_\varepsilon^*} \langle \Phi | T | i \rangle - \cos \Delta \langle \psi_\varepsilon | T | i \rangle \end{aligned} \quad (4.25)$$

where

$$\Phi = \varphi + \mathcal{P} \int \frac{V_{\varepsilon'}^* \psi_{\varepsilon'}}{(\varepsilon - \varepsilon')} d\varepsilon' \quad (4.26)$$

How does the matrix element $\langle \Psi^\varepsilon | T | i \rangle$ vary as a function of ε (particularly as ε passes through the resonance at $\varepsilon_\varphi + F(\varepsilon)$)? It has already been noted that the phase shift (Δ) varies by approximately π ($\sim 0 \rightarrow \sim \pi$, see figure 4.1) as ε varies from $\varepsilon_\varphi + F(\varepsilon) - V_\varepsilon^2 \rightarrow \varepsilon_\varphi + F(\varepsilon) + V_\varepsilon^2$. Since the matrix element is of the form $A \sin \Delta - B \cos \Delta$, where A and B are assumed to be slowly varying, as Δ varies rapidly from $0 \rightarrow \pi$, the value of $\langle \Psi^\varepsilon | T | i \rangle$ will also change rapidly. Further, since *sine* is an odd function about the resonance, whereas *cosine* is even (see figure 4.2), the individual matrix elements ($\langle \Phi | T | i \rangle$, and $\langle \psi_\varepsilon | T | i \rangle$) will interfere constructively on one side of the resonance and destructively on the other. That is, the resonance profile will not be symmetric. In fact, there will be some energy $\varepsilon = \varepsilon_0$ (and corresponding phase shift, $\Delta = \Delta_0$) such that the matrix element (and therefore the probability) vanishes:

$$\begin{aligned}
\langle \Psi^{\varepsilon_0} | T | i \rangle &= 0 \\
&= \frac{\sin \Delta_0}{\pi V_{\varepsilon_0}^*} \langle \Phi | T | i \rangle - \cos \Delta_0 \langle \psi_{\varepsilon_0} | T | i \rangle \\
\tan \Delta_0 &= \pi V_{\varepsilon_0}^* \frac{\langle \psi_{\varepsilon_0} | T | i \rangle}{\langle \Phi | T | i \rangle}
\end{aligned} \tag{4.27}$$

We will now define two parameters that will (immediately) prove useful. The first is the reduced energy variable :

$$\begin{aligned}
\epsilon &= -\cot \Delta \\
&= \frac{\varepsilon - \varepsilon_\varphi - F(\varepsilon)}{\pi V_\varepsilon^2}
\end{aligned} \tag{4.28}$$

The second is the asymmetry parameter or Fano profile index :

$$q = \frac{\langle \Phi | T | i \rangle}{\pi V_\varepsilon^* \langle \psi_\varepsilon | T | i \rangle} \tag{4.29}$$

We will try to put these two parameters (along with equation 4.25) to use in evaluating

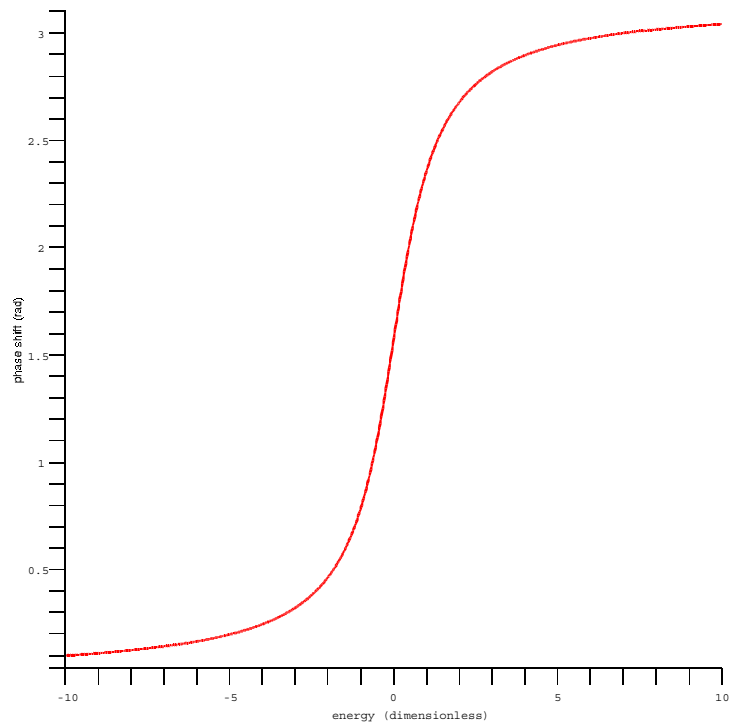


Figure 4.1: Phase shift as a function of energy. The phase shift is in radians. The graph assumes that the interaction between the bound state and the continuum (V_{ε}) is constant.

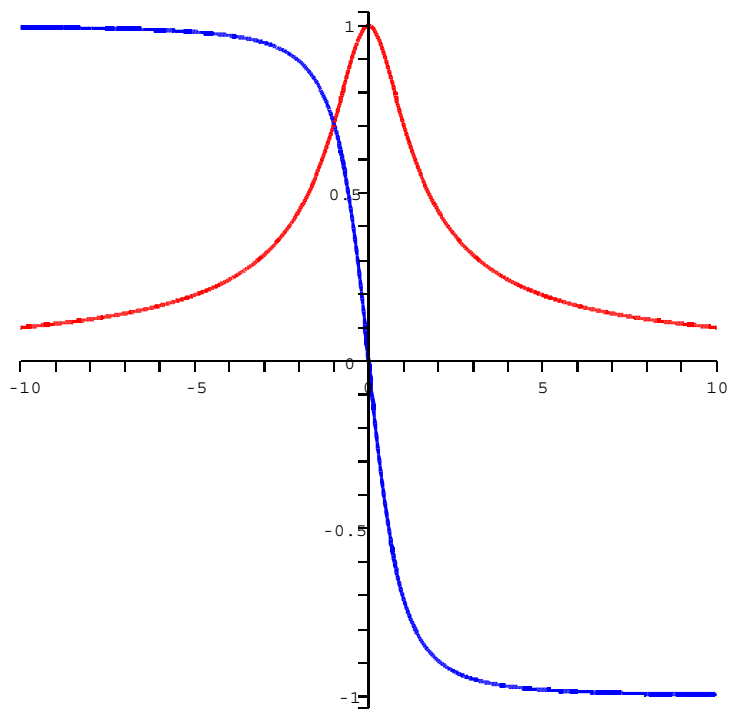


Figure 4.2: Sine (in red) and cosine (in blue) of the phase shift as a function of energy. The vertical axis is dimensionless, the horizontal axis shows values of η .

a particular ratio of probabilities:

$$\begin{aligned}
\frac{|\langle \Psi^\epsilon | T | i \rangle|^2}{|\langle \psi_\epsilon | T | i \rangle|^2} &= \frac{|\langle \Phi | T | i \rangle|^2 \sin^2 \Delta}{|\langle \psi_\epsilon | T | i \rangle|^2 \pi^2 V_\epsilon^2} + \frac{|\langle \psi_\epsilon | T | i \rangle|^2 \cos^2 \Delta}{|\langle \psi_\epsilon | T | i \rangle|^2} \\
&\quad - \frac{\langle \psi_\epsilon | T | i \rangle \langle \Phi | T | i \rangle 2 \sin \Delta \cos \Delta}{|\langle \psi_\epsilon | T | i \rangle|^2 \pi V_\epsilon} \\
&= q^2 \sin^2 \Delta + \cos^2 \Delta - 2 \sin \Delta \cos \Delta q \\
&= q^2 \sin^2 \Delta + \epsilon^2 \sin^2 \Delta - 2q\epsilon \sin^2 \Delta \\
&= [q + \epsilon]^2 \sin^2 \Delta \\
&= \frac{[q + \epsilon]^2}{1 + \epsilon^2} \tag{4.30}
\end{aligned}$$

Why have we taken the trouble to evaluate this ratio? Because the probability for direct ionization ($|\langle \psi_\epsilon | T | i \rangle|^2$) is fairly constant (at least over small variations of energy), so this ratio gives (to within a scale factor) the total probability ($|\langle \Psi^\epsilon | T | i \rangle|^2$) as a function of energy. The graph of the ratio versus the reduced energy shows the Beutler-Fano profile (see figure 4.3). We can also take the ratio of the amplitudes (instead of probabilities):

$$\begin{aligned}
\frac{|\langle \Psi^\epsilon | T | i \rangle|^2}{|\langle \psi_\epsilon | T | i \rangle|^2} &= \frac{[q + \epsilon]^2}{1 + \epsilon^2} \\
\frac{\langle \Psi^\epsilon | T | i \rangle}{\langle \psi_\epsilon | T | i \rangle} &= \frac{q + \epsilon}{\epsilon + i} \\
\langle \Psi^\epsilon | T | i \rangle &= \left[1 + \frac{q - i}{\epsilon + i} \right] \langle \psi_\epsilon | T | i \rangle \tag{4.31}
\end{aligned}$$

For electron impact ionization there are an infinite number of continua. We can use a spherical wave basis for these continuum states, in which case each continuum is characterized by a different angular momentum ℓ . In this case the discrete channel will interfere with only a few (oftentimes only one) of the continua channels. Let us assume that there is interference between the discrete channel and a single continuum channel that is characterized by angular momentum L (i.e., $\langle \varphi | H | \epsilon, \ell \rangle = 0$ for $\ell \neq L$). Rather than trying to determine the total transition amplitude which involves an unknown final state, let us *construct* it (I am basically following Balashov's method [16]). If we know the transition operator (we could for instance choose the Born operator $\sum_j e^{i\mathbf{K}\cdot\mathbf{r}_j}$) and the initial state, then we should be able to calculate any matrix element $\langle \epsilon, \ell | T | i \rangle$. To account for all of the continuum states we merely sum over all ℓ 's. We still need to account for the discrete (autoionizing) state, which can interfere with the continuum state $\langle \epsilon, L \rangle$; to do so we make use of equation 4.31, and the total transition amplitude

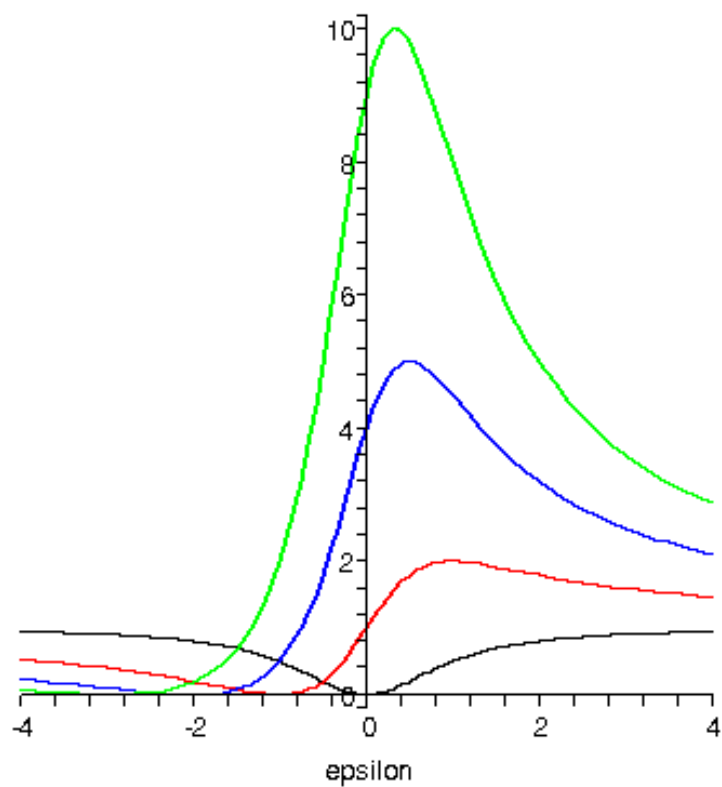


Figure 4.3: The ratio of the total transition probability to that of the direct ionization probability ($[q + \epsilon]^2/[1 + \epsilon^2]$) as a function of the reduced energy, for various values of q (black for $q = 0$, red for $q = 1$, blue for $q = 2$, and green for $q = 3$).

is:

$$\begin{aligned}\langle \Psi | T | i \rangle &= \sum_{\ell \neq L} \langle \varepsilon, \ell | T | i \rangle + \langle \varepsilon, L | T | i \rangle \left[1 + \frac{q-i}{\varepsilon+i} \right] \\ &= \sum_{\ell} \langle \varepsilon, \ell | T | i \rangle + \langle \varepsilon, L | T | i \rangle \frac{q-i}{\varepsilon+i}\end{aligned}\tag{4.32}$$

The TDCS is proportional to the modulus squared of this matrix element.

Chapter 5

Experimental apparatus

At the simplest level a scattering experiment needs three things; projectiles to shoot, targets to shoot at, and one or more detectors (for an $(e, 2e)$ experiment one must be able to detect *both* outgoing electrons, so one usually needs at least two detectors) to detect the aftermath. For our experiments the projectiles and targets have been electrons and helium atoms respectively. The apparatus used is a “conventional” $(e, 2e)$ spectrometer; figures 5.1 and 5.2 show the “guts” of the apparatus schematically and photographically (respectively). The main components shown in these figures are:

1. An unmonochromated electron gun.
2. A nozzle (with a 1 mm diameter opening) used to produce the atomic beam.
3. Two ejected electron detectors, each consisting of a set of electron-optics elements, followed by a hemispherical-sector-electrostatic energy analyzer that is terminated by a position-sensitive detector (PSD). The two ejected electron detectors are mounted opposite each other on a single turntable.
4. A scattered electron detector of the same basic design as the ejected electron detectors except for minor differences in the electron-optics and that the detector is terminated with a channel-electron-multiplier instead of a PSD. The scattered electron detector is mounted on a turntable that is coplanar with, but independent of, the turntable for the ejected electron detectors.

These components are all located within a vacuum chamber and are surrounded by a double layer of high permeability μ -metal shielding to eliminate the effects of external (principally the earth’s) magnetic fields. This shielding reduces the magnetic field at the interaction region to less than 30 mG [19, pg. 37]. Additionally, the chamber is surrounded by three pairs of Helmholtz-type coils; however, it has been found that use of these coils does not have a measurable effect on our experiments, and they are therefore left de-energized.

This apparatus was originally designed for coplanar experiments (this configuration has been described previously [20, 21]). The original configuration is described in

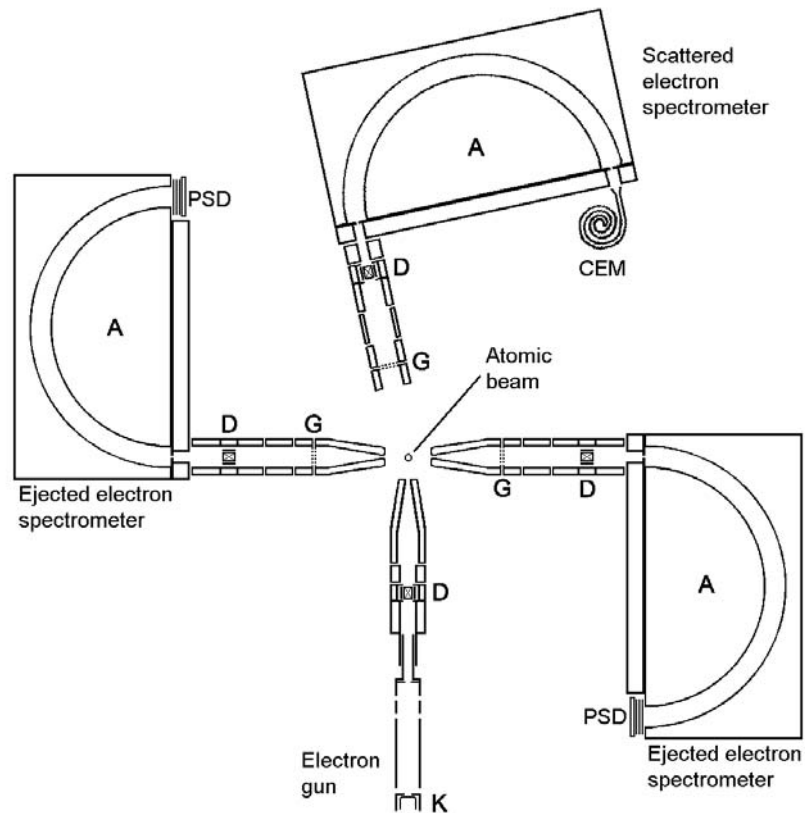


Figure 5.1: Schematic of the main components in the vacuum chamber of the $(e, 2e)$ apparatus. A—hemispherical sector energy analyzer, D—deflector, G—grids, K—cathode, CEM—channel electron multiplier, PSD—position sensitive detector.

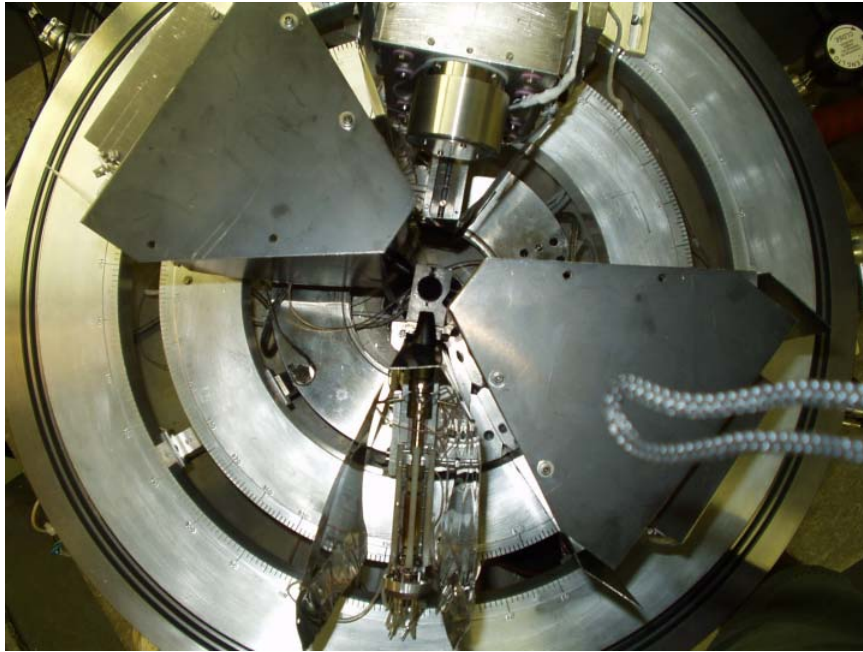


Figure 5.2: Photograph of the $(e, 2e)$ apparatus configured for coplanar measurements. There are three electron detectors; one for detecting the scattered electrons (at 1 o'clock), and two for detected ejected electrons (at 4 and 10 o'clock). The electron gun is at 6 o'clock. The strap of the photographer's camera is visible on the right side of the image.

sections 5.1 through 5.6 and was used for the experiments described in appendix A. Some minor modifications to allow for automated movement of the scattered detector turn table are described in section 5.7; these were needed to facilitate the experiments described in chapter 6. Finally, a major modification involving the incorporation of a movable electron mount and gas nozzle is detailed in 5.8; these modifications were needed to allow for the out-of-plane measurements described in chapter 7.

5.1 Vacuum system

The vacuum system is able to reach pressures as low as approximately 10^{-7} torr in the chamber (when the atomic beam is not on), and normally maintains a pressure of around 10^{-4} torr when the atomic beam is on. The major components of this system are shown in figure 5.3; not shown are the pressure gauges and the ancillary cooling systems (for the diffusion pump and the cold trap). The vacuum system consists of the following components:

1. The chamber housing the electron gun, gas nozzle, and spectrometers. The chamber is cylindrical, approximately 1 meter in diameter and 1 meter tall. The chamber is in two pieces, the body and the lid (the two halves are held together by air pressure and the weight of the lid). A rail-mounted hoist is used to lift the lid when opening the apparatus. A vacuum tight seal between the two pieces is achieved using two viton o-rings (visible in figure 5.2). There is a small space between the two o-rings that is normally evacuated using a mechanical pump (see figure 5.3).
2. Numerous feedthroughs. Sixteen feedthroughs, each with a 2.75 inch Conflat flange, circle the body of the chamber. The majority of these are used for electrical feedthroughs, with the remainder being used for ion gauges and a rotary feedthrough. The bottom of the chamber body has two rotary feedthroughs used to turn the turntables (see section 5.4), two 6 inch pumping ports connected to diffusion pumps (only one of which is in use) and two gas inlets. Two feedthroughs are located on the top of the lid, one is blanked off, the other has a window used to visually check the positions of the turntables (see section 5.4).

3. A diffusion pump (Varian VHS-6 six inch) with a cold trap.
4. A rotary mechanical pump (Sargent & Welch 1374) used to back the diffusion pump (and to “rough out” the apparatus).
5. A chiller (Neslab CC-100II) with a cold finger used to cool (normally to temperatures between -50°C and -20°C) the cold trap at the top of the diffusion pump.
6. An ion and a Pirani gauge, and associated controllers, for monitoring the pressure in the chamber (using the ion gauge) and the backing pressure (using the Pirani gauge). The controller for the ion gauge has a trip point board installed, which is used to shut down various systems in case of a leak.
7. Various valves for isolating different parts of the vacuum system.
8. Plumbing, filter, and waterflow switch for cooling the diffusion pump. If the waterflow to the diffusion pump drops below a particular amount (normally due to a dirty filter or a water outage), the waterflow switch opens which causes the diffusion pump and various other systems to be shut down.

It should be noted that the vacuum system has a few ... idiosyncrasies. The first involves the chiller used to cool the cold trap. The chiller has a defect which causes it to become progressively less efficient as time goes on (e.g., if left on continuously the temperature of the chiller’s cold finger used to cool the trap will increase to a temperature of 0°C in the course of several days). The (mostly successful) remedy for this situation is to use a timer to turn off the chiller for an hour each day. This appears to be long enough to allow the chiller to “revive” and short enough that the cold trap does not warm up significantly.

Another idiosyncrasy involves the diffusion pump oil (NEOVAC SY). This fluid is a synthetic hydrocarbon that “will not produce inorganic deposits which can cause electrostatic charge buildup on electrodes of sensitive instruments” [22]; this is supposed to be true without using trapping. Despite the fact that there is a cold trap being used, there is evidence of diffusion pump fluid entering the chamber of the apparatus and causing deposits to form: surfaces which have undergone sustained electron impact develop a bluish-black film [19], and the odor of pump oil is present when the apparatus

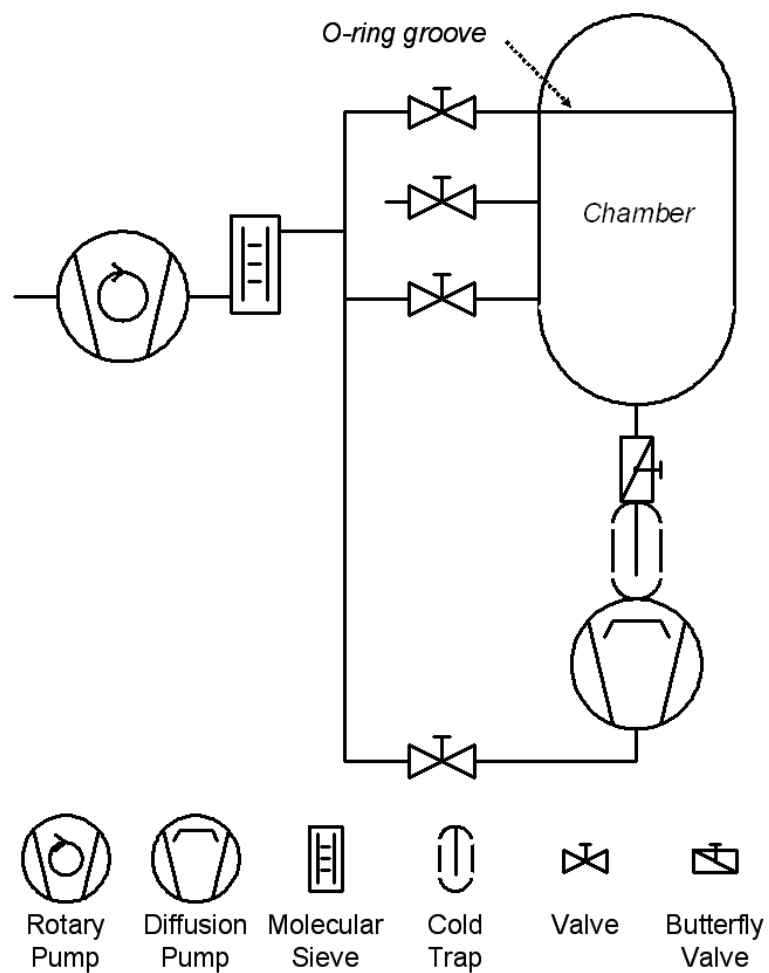


Figure 5.3: Vacuum system schematic.

is opened. Fortunately, while this has been a nuisance, it has not been a significant problem.

5.2 Electron gun

The incident electrons (i.e., the electron beam) for our experiments are produced by thermionic emission from a thoriated tungsten hairpin filament. The filament is part of a Vacuum Generators LEG 21 electron gun, to which have been added several titanium, cylindrical electro-optic lens elements (to shape the electron beam) and two pairs of deflector plates (to steer the beam). Acceleration of the electrons is achieved by holding the filament at a negative voltage relative to the interaction region. The interaction region is assumed to be at ground, therefore the absolute value of the voltage of the filament is approximately equal to the energy of the electrons in the electron beam as they enter the interaction region. A diagram of the electron gun is shown in figure 5.4.

The energy distribution of electrons produced by thermionic emission is Maxwellian. The FWHM of the distribution (ΔE), expressed in eV, is [23, p. 1654]:

$$\Delta E = 2.54 k_b T \tag{5.1}$$

where k_b is Boltzmann's constant, and T is the temperature of the filament. A tungsten filament will typically have a temperature of approximately 2900 K; resulting in an energy spread of $\Delta K \approx 0.6$ eV. Compared to the intensity of the beam, ΔE is relatively insensitive to the temperature of the filament, so $\Delta K \approx 0.6$ eV is a fairly good approximation regardless of the intensity of our electron beam.

The energy of the electron beam can be varied from approximately 40 – 550 eV, and the intensity from approximately 10 nA – 20 μ A. The electron beam has a diameter of approximately 1 mm at the interaction region, and has been determined to have an elliptical profile [19].

Tuning the electron gun (which consists of setting the voltages for the various optics elements, and the filament voltage and current) seems to be as much art as it is science. The process can be divided into three levels: coarse tuning, where the goal is simply to get some sort of electron beam; fine tuning, where quality of beam (e.g., how tight the beam is) is adjusted; and, for lack of a better name, final tuning, where the beam is adjusted to optimize whatever measurement is being made. Coarse and fine tuning are

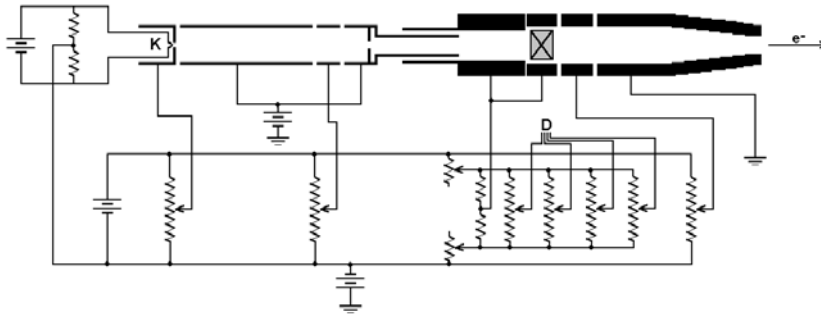


Figure 5.4: Schematic of the electron gun.(Figure from [19]).

usually only needed after significantly changing the filament voltage (which is the same as changing the beam energy), or when something has gone seriously wrong.

Fortunately the gun is mature enough that coarse tuning is simply a matter of looking up a set of voltages appropriate for the desired beam energy; my predecessor had to make use of electron optics simulation software to get these starting voltages [19].

For fine tuning we use a Faraday cup (see figure 5.5) to measure the quality of the electron beam. The Faraday cup is mounted on the scattered turntable at the $+20^\circ$ position (i.e., rotation of the scattered turntable so that $\theta_{sc} = -20^\circ$ will put the Faraday cup opposite the electron gun). There are three cylindrical electro-optic elements comprising the Faraday cup:

1. First (from the point of view of an electron emanating from the electron gun) is a grounded lens whose purpose is to limit the angular acceptance of the Faraday cup.
2. Next is a grounded cylinder terminated by a disk with a 1mm aperture that we refer to as the *outer cup*. The purpose of this lens is to capture electrons from the beam that are outside the desired beam spot. A microammeter is used to measure the current which we typically label as I_{outer} .
3. Finally there is a cylinder that is terminated by blank disk and fronted by a disk with a 2mm aperture, that we refer to as the *inner cup*. The purpose of this element is to capture electrons from the beam that are focused in the desired

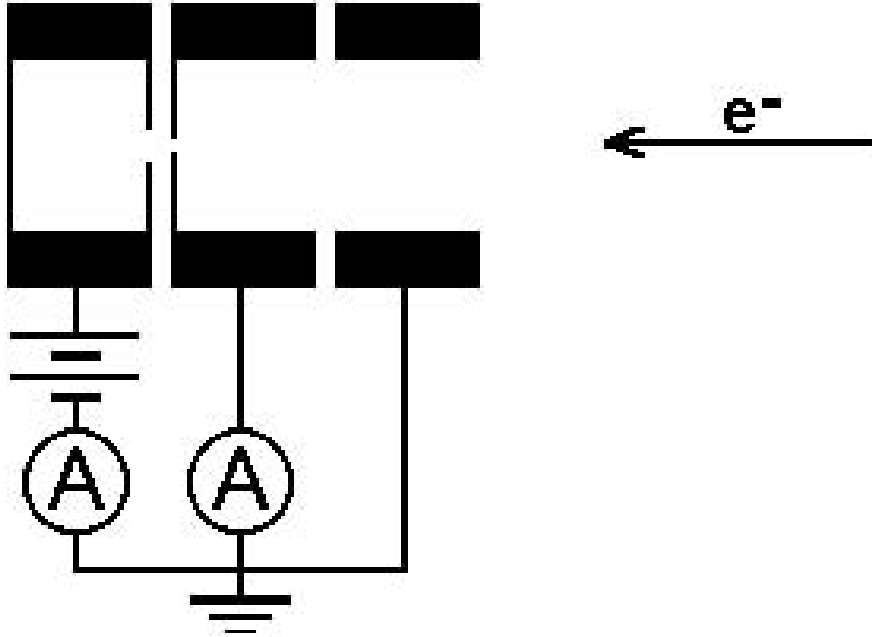


Figure 5.5: Schematic of the Faraday cup. **A** labels the microammeters. (Figure and caption from [19]).

beam spot, and the element is floated at +15V to prevent secondary emissions from reducing the measured current. A second microammeter is used to measure this current which is labeled as I_{inner} .

The actual process of fine tuning consists of adjusting the potentials for the various elements of the electron gun until the ratio I_{inner}/I_{outer} has been maximized. We typically expect to achieve $I_{inner}/I_{outer} \geq 1/10$.

Naively one might think that the only task left after fine tuning is to adjust the electron gun deflectors so that the electron beam intersects the atomic beam at the appropriate location (i.e., at a point along the axes of the various detectors). It's not that simple. The most obvious complication arises from the fact that we usually need to maximize the number of collisions between the electrons in the electron beam, and the atoms in the atomic beam. Since the atomic beam is not only of finite cross-section, but has “fuzzy” edges, we often need to change the focus of the electron beam to maximize interactions. One could spend a lot of time studying these various complications. However we tend to take the pragmatic approach of understanding that final tuning of the

electron gun varies from experiment to experiment. For the experiments in appendix A we typically adjusted the voltages for the lenses and deflectors to maximize the ejected count rates. For the experiments in chapter 6 we needed to maximize the coincidence count rate, but this count rate is too low to measure while tuning. Unfortunately if we maximized the ejected count rates the scattered (and consequently the coincidence) count rate would suffer, and vice versa. We therefore tune the electron gun so that we get some (arbitrary) combination of high (but not usually maximum) ejected and scattered count rates.

It should be noted that it has been observed that the power supply used to bias the filament (i.e., set the beam energy) fluctuates by a few tenths of a volt (over the course of a few days). This does not affect the tuning of the gun (which is immune to such small changes), nor does it affect the measurement of ejected electron energy spectra over autoionizing resonances (appendix A) since these cross-sections are also insensitive to small changes in incident energy. However this has a drastic affect on coincidence measurements since a change in incident energy changes the energy loss of the scattered electrons we are detecting. This may account for our need to periodically retune the scattered detector to increase coincidence rates.

5.3 Gas jet

Helium is allowed to flow effusively into the chamber through a metal nozzle to produce the atomic beam. For the experiments described in appendix A and chapter 6 the nozzle is stainless steel with a 1mm diameter opening and is 1cm long (see section 5.8 for details about the nozzle used for the experiments in chapter 7). The pressure in the interaction region is controlled by a mechanical leak valve and monitored by reading the background pressure (using an ion gauge) in the chamber.

5.4 Spectrometers

The word *detector* has two different (but related) usages in this work. Usually it refers to an entire assembly that is more precisely called a *spectrometer*, of which the apparatus has three (two for ejected electrons, one for scattered electrons). Each of the spectrometers consists of (a) a set of electro-optic elements for bringing electrons span-

ning some solid angle from the interaction region to the entrance aperture of (b) a 180° hemispherical sector electrostatic energy analyzer (HSA), which allows those electrons having the desired energy to pass through to (c) the detector (where we have now come to the second usage of the word *detector*, which will be the only usage for the remainder of this section).

The two ejected electron spectrometers are identical (see figure 5.6; as a matter of convenience we refer to them as being *red* and *blue*) and are similar to the scattered electron spectrometer (shown in figure 5.7). One difference is in the first (from the electron’s point of view) element of the optics; the ejected spectrometers each have a nose cone to reduce their angular acceptance (the nose cones are electrically tied together and can be isolated from ground, this was done to increase efficiency for detecting low energy electrons [19, p. 38]), while the scattered spectrometer has an open cylinder (that is grounded) to reduce secondary emissions from the incident electron beam striking it. The remainder of the optic elements are, at least functionally, quite similar. Following the first element is a grounded mesh that isolates the interaction region from the potentials of the subsequent elements. Next is another mesh, held at some negative potential, that reduces the longitudinal component of the electrons’ velocity. A pair of Einzel lenses follow for focusing the incoming electrons. Finally, there are two pairs of electrostatic deflector plates for steering the electrons into the entrance aperture of the HSA.

The three 180° hemispherical electrostatic energy analyzers (henceforth referred to as *analyzers*) each have a 3 inch central radius, 0.5 inch gap, and 0.040 inch entrance aperture. They are all identical except for the exit apertures, with the scattered analyzer having a 0.040 inch exit aperture, while the ejected analyzers do not have exit apertures. As a first approximation one can consider the trajectories of the electrons travelling through the analyzer as being described by straightforward orbital mechanics (as detailed in Goldstein [24] for instance) since electrostatic and gravitational potentials are both proportional to $1/r$.

The pass energy E_0 of the analyzer is the energy needed by an electron entering the middle of the entrance aperture to get to the diametrically opposed position, and is found (if we neglect the effects of fringe fields) by equating the centripetal and electrostatic

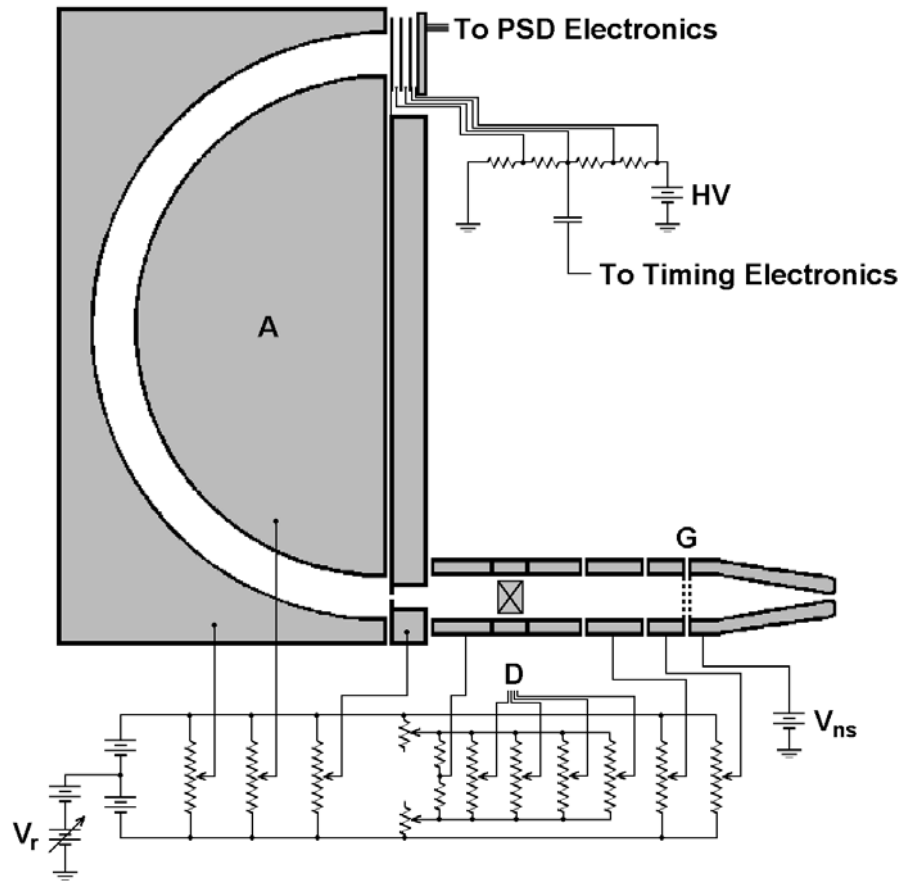


Figure 5.6: Schematic of the ejected electron spectrometer.(Figure from [19]).

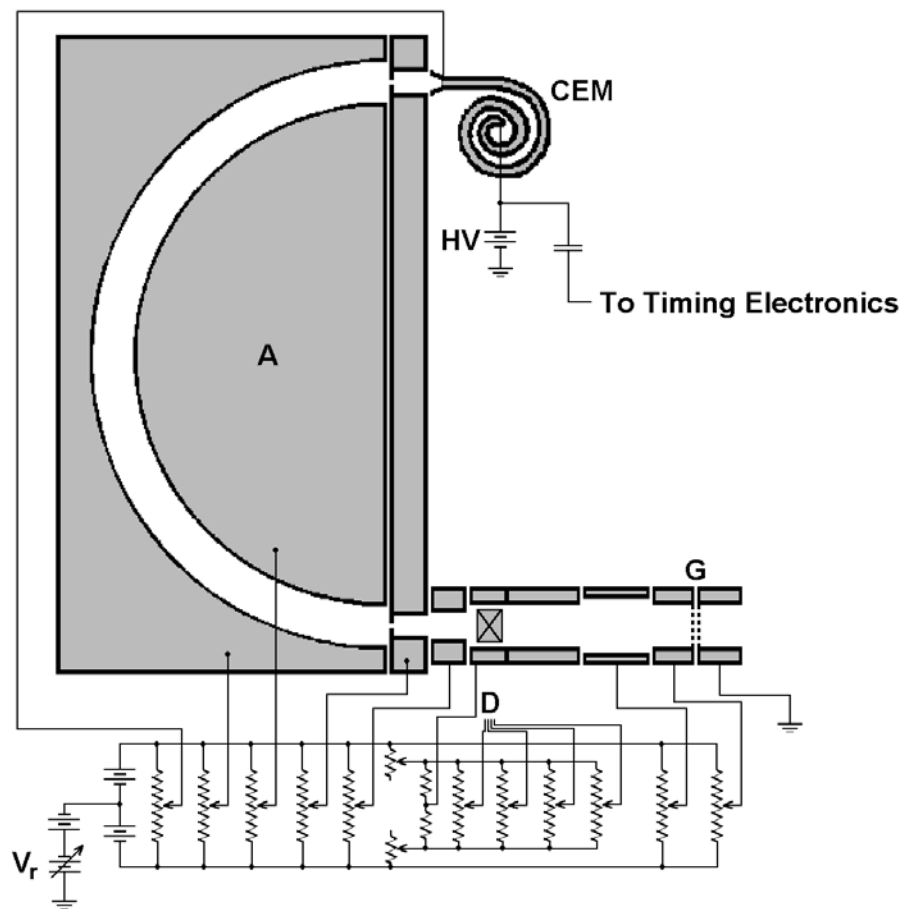


Figure 5.7: Schematic of the scattered electron spectrometer.(Figure from [19]).

forces (i.e., meet the requirements for a circular orbit)

$$\frac{m_e v^2}{r} = E e, \quad (5.2)$$

where m_e is the mass of the electron, v is its velocity, r is the distance from the entrance aperture to the origin of the hemispheres, E is the electric field, and e is the charge of the electron. Since \hat{E} is radial (as long as we ignore fringing fields) we can imagine the electric field as arising from some charge Q at the origin (i.e., $E = \frac{Q}{4\pi\epsilon_0 r^2}$ where r is the distance of the entrance aperture from the origin). The magnitude of the charge is determined by the voltage across the hemispheres ΔV and the radii of the outer and inner hemispheres (r_a and r_b respectively):

$$\begin{aligned} \Delta V &= \frac{Q}{4\pi\epsilon_0} \left(\frac{1}{r_b} - \frac{1}{r_a} \right) \\ &= \frac{Q}{4\pi\epsilon_0} \left(\frac{r_a - r_b}{r_a r_b} \right) \\ Q &= \Delta V 4\pi\epsilon_0 \frac{r_a r_b}{r_a - r_b} \end{aligned} \quad (5.3)$$

Equation 5.2 then becomes:

$$\begin{aligned} \frac{mv^2}{r} &= \frac{e}{4\pi\epsilon_0 r^2} \Delta V 4\pi\epsilon_0 \frac{r_a r_b}{r_a - r_b} \\ \frac{1}{2}mv^2 &= e\Delta V \frac{1}{2r} \frac{r_a r_b}{r_a - r_b} \\ E_0 &= e\Delta V \frac{r_a r_b}{2r(r_a - r_b)} \\ &= \frac{143}{48} \Delta V \\ &\approx 3 \Delta V \end{aligned} \quad (5.4)$$

(where the values $r = 3$ in., $r_a = 3.25$ in., and $r_b = 2.75$ in. have been used, and the pass energy is expressed in eV). The energy resolution ΔE of the analyzer is directly proportional to E_0 and (to first order) the diameter of the entrance aperture (see for example [19, 25, 26]).

Since the size of the entrance aperture is fixed, we set the pass energy for our desired resolution. However the energy of the electrons we wish to detect does not, in general, match the pass energy. The plate holding the entrance aperture is therefore set at a (usually negative) potential to adjust the energy of the electrons. When taking an energy spectrum we wish to have the same resolution throughout, therefore we step

the plate voltage to scan through energy (rather than stepping the pass energy). The voltages for the plate, hemispheres, and the optics elements all float on one of two *ramp* voltages (labeled V_r in figures 5.6 and 5.7, there is one ramp voltage for both ejected spectrometers, and a second ramp voltage for the scattered spectrometer), and can therefore be changed simultaneously simply by altering V_r .

Recall that the ejected analyzers do not include an exit aperture (although there is an 0.5 inch diameter “entrance” aperture for the detector following each analyzer), therefore electrons with a range of energies (roughly centered about the pass energy) are passed by these analyzers. The width of this band is proportional to the pass energy. Knowledge of the position within the 0.5 inch gap where the electrons exit the analyzer allows us to determine their energy [27]. To gain this information each ejected analyzer is followed by a position sensitive detector (PSD), each PSD consisting of a stack of three micro-channel plates (MCPs) followed by a 1 inch square (of which we only use a 0.5 inch diameter circle) two dimensional resistive anode, which allows us to determine both when, and where, the electron arrives at the detector. The MCPs act as amplifiers, for each electron striking the first MCP a large burst of electrons subsequently leaves the third MCP and then strikes the resistive anode. The second MCP in each stack also provides a signal to the NIM (nuclear instrument module) units indicating the arrival of an electron (see section 5.5). From each of the four corners of the resistive anode a signal is sent to a preamplifier and then a Quantar Technologies model 2401B position decoder. The decoder provides the x and y position of the electron as two 8-bit parallel signals – effectively dividing the surface of the resistive anode into 0.004^2 inch² squares.

Since we use less than half of the surface of each resistive anode we are able to use a single position decoder and set of preamplifiers to handle both resistive anodes (which provided a significant cost savings). To do so we physically use one half of each resistive anode (i.e., rather than the entrance aperture for the detector being centered on the resistive anode, it is shifted to one side) and mix the signals (which in this case is simply a matter of connecting the signal wires together) at the input to the preamplifiers. The results, as this system was originally implemented, are shown graphically in figure 5.8. However, over time the surface of each resistive anode (specifically the part of the surface that is being bombarded by electrons) appears to have become stained; this causes a

false shift in the encoded position of each electron towards the middle of the resistive anode. The shift means that the images from the two PSDs now partially overlap. To determine which PSD has detected an electron we send the (timing) signal from the MCP to a “tagger” (see section 5.6).

For $(e, 2e)$ experiments we need to detect scattered electrons with a range of energy losses corresponding to the range of ejected electron energies that are being detected; i.e., we need to detect a wide range of energies. Therefore, for the scattered electron spectrometer, we set the pass energy very high, and use a channel electron multiplier (CEM or channeltron) as the detector.

5.5 Timing circuitry

The apparatus I have been describing is used for $(e, 2e)$ experiments, therefore it must be able to detect the arrival of two electrons, and determine if their arrival times fall within some interval that is indicative that they may have come from the same event (specifically an event described by equation 1.2). One usually accomplishes this by using a signal that marks the arrival of the faster particle to start a timer that is then stopped by a signal marking the arrival of the slower particle. If the amount of elapsed time falls within the specified interval, the event is recorded. In our case the scattered electrons are fast and the ejected electrons are slow. However, for most experiments we detect far more scattered than ejected electrons, and it is simpler to use the arrival of the ejected electron to start the clock (with a delay line used to postpone the stop signal from the scattered spectrometer).

A block diagram showing the major components of the timing circuitry is shown in figure 5.9. The actual timing is performed by a time-to-amplitude converter TAC, and starts when a signal from the middle MCP in one of the ejected spectrometers arrives (via a pulse transformer, preamp, timing filter amplifier TFA, and constant fraction discriminator CFD) at the start gate. Timing stops when a signal from the scattered spectrometer (specifically the channeltron) arrives (via a similar path as for the ejected signal, plus a delay line) at the stop gate of the TAC. The interval between the arrival of the ejected and scattered signals is then sent as an analog signal to an analog-to-digital converter installed in an Apple IIe computer.

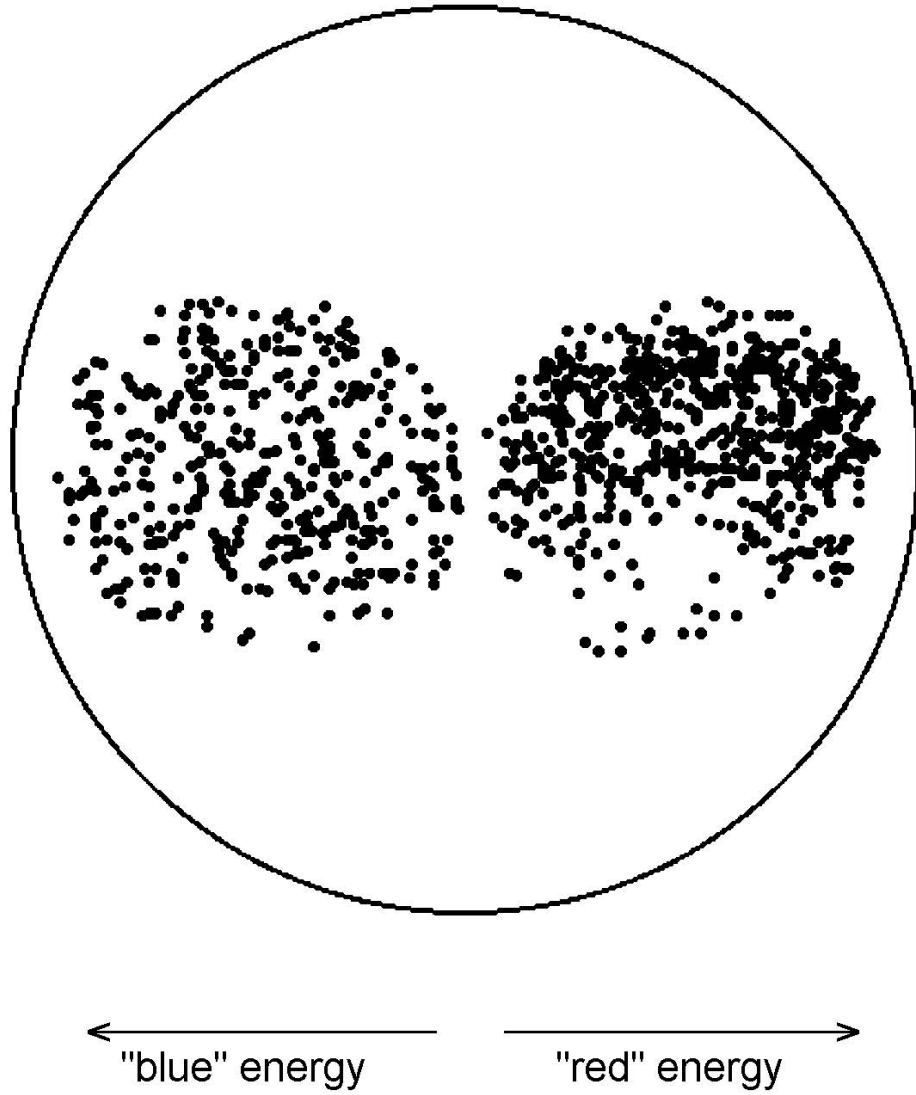


Figure 5.8: Combination of the signals from the two PSDs forming two non-overlapping images as it was originally implemented. (Figure reproduced from [19, fig. 3.7]).

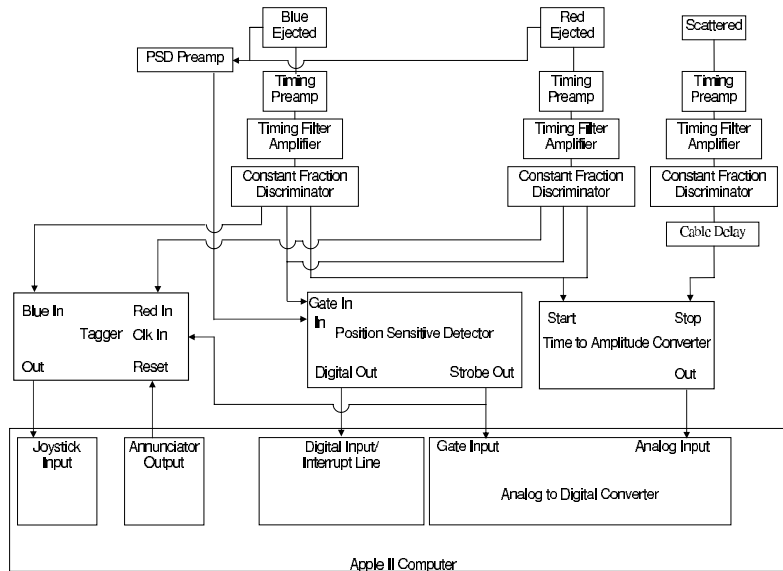


Figure 5.9: Block diagram of timing and signal processing circuitry.

Figure 5.10 shows an idealized distribution of the difference in arrival time of ejected and scattered electrons. The time differences are not absolute since they are affected by the amount of delay line we use for the scattered signal as well as delays (both inherent and adjusted) in the various units in the signal paths. We should note that the mere fact that we receive a scattered and an ejected electron within the appropriate time interval does not guarantee that they both originated from the same event; in fact we can never be sure of this. Looking at figure 5.10 we see that there is a constant rate of accidental coincidences in addition to the distribution of “true” (i.e., actually coming from the same event) coincidences. The distribution of arrival time differences for the true coincidences is affected by both the timing resolution of the spectrometers (two electrons with the same energy may arrive at the detector at slightly different times if they take different paths through the spectrometer) and the energy width of the incident electron beam (because two scattered electrons with the same energy loss may have different energies due to the energy width of the electron beam). To find the true coincidence rate we examine a window of arrival time differences spanning $50 \rightarrow 400$ ns (the time interval from $0 \rightarrow 50$ ns is discarded because of observed non-linear effects [19, pgs. 32-33]). For low count rates the accidental coincidence rate is

effectively constant throughout this interval¹. We divide this interval into two windows, a 50 ns *up* window that is (ideally) centered temporally on the true coincidence peak (which is less than 50 ns wide), and a *down* window consisting of the remaining (non-contiguous) 300 ns. To find the number of accidental coincidences that occur during the up window, we take the number of counts in the down window N_D (which should all be accidental coincidence counts) and scale them by the ratio n of the duration of the down window to the duration of the up window. The number of true coincidence counts N_T is then the total number of counts in the up window N_U less the number of accidental coincidences $N_T = N_U - N_D/n$. Assuming that these quantities follow Poisson statistics (i.e., $\sigma_{N_U} = \sqrt{N_U}$ and $\sigma_{N_D} = \sqrt{N_D}$) the uncertainty for N_T is:

$$\begin{aligned}\sigma_{N_T} &= \sqrt{\left(\sigma_{N_U} \frac{\partial N_T}{\partial N_U}\right)^2 + \left(\sigma_{N_D} \frac{\partial N_T}{\partial N_D}\right)^2} \\ &= \sqrt{N_U + \frac{N_D}{n^2}}\end{aligned}\tag{5.5}$$

We therefore express the number of true coincidence counts as:

$$N_T = N_U - \frac{N_D}{n} \pm \sqrt{N_U + \frac{N_D}{n^2}}\tag{5.6}$$

where for our experiments $n = 6$.

5.6 Computer control and data collection

Control of the experiment and data collection are accomplished using an Applesoft BASIC program and an assembly language interrupt routine, both developed in-house and running on an Apple IIe computer. Control (which is accomplished by the BASIC program) entails setting the pass energy of the spectrometers (i.e., setting the ramp voltage described in section 5.4), and (for some experiments) the positioning of the scattered spectrometer (see section 5.7) or the electron gun (see section 5.8). The ramp

¹The constancy (or lack thereof) of the accidental coincidence rate can be understood by dividing the interval into a set of bins, and then comparing the probability that a count will occur in bin N (which I will call P_N), and the probability that it will occur in bin $N + 1$ (which I will call P_{N+1}). The thing to remember is that these bins represent the time after a scattered electron has been detected, and that once we detect an ejected electron the timing starts (i.e., for each detected scattered electron we will count, at most, a single ejected electron). Therefore, to get a count in bin $N + 1$ we must *not* get a count in bin N ; i.e., $P_{N+1} = (1 - P_N)P_N$. If the count rate R is low, and/or the interval τ is short (i.e., $R\tau \ll 1$), then P_N will be small, $P_{N+1} \approx P_N$, and the accidental coincidence rate will be approximately constant.

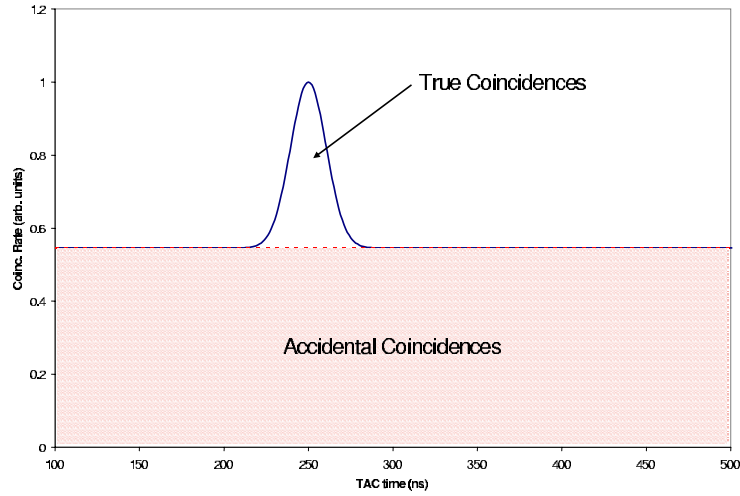


Figure 5.10: Distribution of electron arrival times.

voltages are set using two (one for each ramp) digital to analog converters (DACs) connected to a Super Serial expansion card on the Apple. The DACs each provide a range of ramp voltages $0 < V_r \leq 10V$ with 16 bit resolution.

Additionally, the BASIC program sets up the memory locations where data is to be stored, sets various parameters to be used for processing data, and periodically transfers data (to a PC) over a serial line. The actual processing of data is accomplished using an interrupt routine that is triggered by the PSD. For all experiments the interrupt routine reads data from (a) the PSD to determine the energy of the ejected electron that was detected (b) the tagger (which is connected to the joystick input, and basically latches the timing signal from the MCPs [28]) to determine which (*red* or *blue*) detector detected the ejected electron, and (c) the TAC (via an ADC card) to check if an up or down count should be recorded. Connections between the sources of these various signals and the Apple IIe are shown in figure 5.9. The interrupt routine also bins the data (i.e., a histogram of the data, as opposed to the raw data, is stored in memory).

The processing of the interrupt routine determines the maximum rate at which data can be taken. The microprocessor in the Apple IIe normally runs at a clock rate of 1 MHz, however the installation of a TransWarp accelerator card increases this rate to

3.6 MHz (technically it entirely replaces the microprocessor, but this is transparent to the user). Keep in mind that all assembly instructions require at least two clock cycles to execute, so the rate at which instructions are executed is actually less than 1.8 MHz (refer to [29, pg. 40] for a table showing the number of clock cycles required for the various instructions). Since the interrupt routine executes several scores of instructions, its processing takes a greater amount of time than the processing of signals by the PSD (which in turn takes a longer time than the timing circuitry).

5.7 Scattered turntable modification

To perform the experiments detailed in chapter 6 it was necessary to automate the positioning of the scattered spectrometer. Apparently the apparatus had been configured with this capability during its previous life in Southampton, UK, and some of the parts (a continuous drive DC motor, and a motor driver that interfaces to a paddle output on the Apple) were still in place and quickly put into service (to the extent that the turntable could be moved for a specified amount of time, but not to a specific position) by adding a large o-ring as a drive belt between the motor and a rotary feedthrough that was (and continues to be) used to manually position the scattered turntable. What was not available were the components and software for detecting the position of the spectrometer (and consequently to position it).

To determine the position of the spectrometer we fixed a section of drive-belt to the turntable (see figure 5.11, the drive-belt spans an arc of approximately 80°). As the turntable rotates, the drive-belt turns a pulley mounted on a ten-turn potentiometer (across which we read a voltage drop to determine the position of the turntable). The potentiometer is held by a swing arm that is mounted to one of the turntable supports. We apply a voltage across the potentiometer using an external DC power supply and connect the ground and slider to the Apple II (see figure 5.12). The Apple has a built in 8 bit analog-to-digital converter capable of handling voltages from 0 to +5V. The greatest span of angles we have in a single experiment is $-30^\circ \rightarrow +30^\circ$; by adjusting the external DC power supply so the potentiometer slider varies from 0 to 5V over this range of angles the best angular resolution we can expect is slightly better than $1/4^\circ$. However, since we tend to position the scattered spectrometer at integral valued angles,

it is desirable to have a resolution of $1/n^\circ$, where n is some integer value. We therefore adjust the power supply so that $0 \rightarrow 5V$ corresponds to a span of 64° and an angular resolution of (not better than) $1/4^\circ$.

Holding the pulley firmly against the drive belt (or at least firmly enough that the pulley is consistently driven by the belt) was problematic; i.e., the potentiometer kept slipping. The problem with slippage is that it leads to inaccuracies in the potentiometer reading of position. Originally, the design fixed the position of the swing arm; the idea being to push the swing arm so that the pulley was hard against the turntable, then to lock the arm in place. The surface to which the belt is mounted is not perfectly round however, and there would inevitably be positions where the pulley lost contact with the belt. Further, pushing the pulley hard enough to minimize this loss of contact would unacceptably increase the amount of torque needed to turn the turntable. The use of springs to reduce slippage was rejected since they tend to be magnetic (and magnetic fields are to be avoided in our types of experiments). The final solution was to use a weight (consisting of a pair of spare chunks of copper) suspended by copper wire to pull the swing arm (and therefore pulley) against the belt. (The wire is draped over a support so that the downward direction of the weight is redirected). Despite these efforts, there was still some amount of slippage. During a typical experiment (that makes use of this modification) the position of the scattered spectrometer is repeatedly scanned from one angle to another and back again, usually in 2° increments. As an experiment progressed the slippage caused an increasing uncertainty in the position of the turntable. To deal with these uncertainties we installed a calibration switch (see figure 5.12) that is physically depressed as the turntable passes through the $\theta_{sc} = 0^\circ$ position as the turntable rotates towards larger angles, or as the turntable passes through the $\theta_{sc} = +2.5^\circ$ position as the turntable rotates towards smaller angles. (The difference in positions where the switch is depressed is because the switch remains closed for 2.5° of travel). At the beginning of each scan a flag that indicates whether or not the switch has been closed is reset. For the duration of the scan, as the turntable is moved through a 2° step the status of the switch is checked repeatedly (as long as the flag is not set); if the switch is found to be closed we set the flag, calibrate the position, and no further checks of the switch are performed for the remainder of the scan.

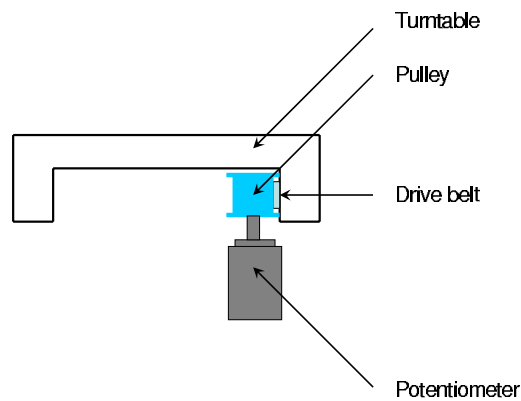


Figure 5.11: Cross-sectional view of the scattered turntable showing the drivebelt mounted to the turntable, and the pulley and potentiometer that are turned by the drivebelt as the turntable moves. Not shown is the swing arm holding the pulley, and the weight that pulls the potentiometer against the drive belt.

So far I have mentioned two sources of error (finite angular resolution and slippage) in positioning the scattered spectrometer. There is a third source; tension in the o-ring drivebelt (used to couple the motor to the rotary feedthrough) can cause the turntable to move after the motor stops. This problem is dealt with in the routine that handles positioning the spectrometer; after the spectrometer is within $1/4^\circ$ of the desired location, the routine goes into the following loop

```

BEGIN LOOP
    PAUSE A FEW SECONDS
    MEASURE POSITION
    IF AT DESIRED POSITION, EXIT LOOP
    ELSE, NUDGE TURNTABLE TOWARDS DESIRED POSITION
REPEAT

```

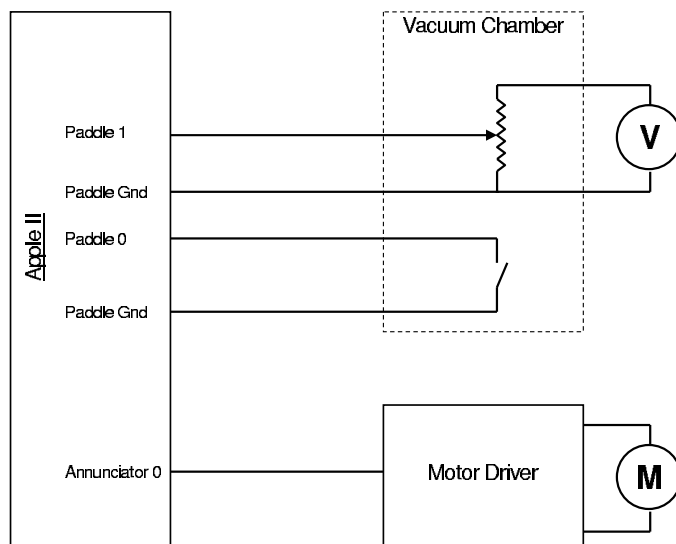


Figure 5.12: Block diagram for the scattered turntable modification. The potentiometer measures the angular position of the scattered turntable (a constant voltage is maintained across the potentiometer by the external power supply labelled V). The (calibration) switch is closed when the position is between 0° and $+2.5^\circ$. The motor (labelled M) turns the turntable.

In general we have found that we can consistently position the scattered spectrometer to $\pm 1/2^\circ$ using these modifications.

5.8 Movable electron gun mount

Out-of-plane measurements can be achieved either by moving the ejected electron detectors out of the scattering plane or by rotating the scattering plane about some axis while keeping the ejected electron detectors fixed. Space constraints make the former impracticable in our apparatus. The scattering plane can be rotated about two obvious axes, the incident electron direction \hat{k}_0 , and the scattered electron direction \hat{k}_{SC} . In fact the experiments of interest to us involve measuring ejected electron angular distributions in a plane perpendicular to both the scattering plane and the scattered electron direction \hat{k}_{SC} . We therefore rotate the scattering plane about the scattered electron direction \hat{k}_{SC} – i.e., we move the electron gun. This is advantageous because the electron gun in our apparatus is smaller (and considerably lighter) than the scattered electron detector, and a movable gun mount is therefore more compact.

The geometry of our apparatus is shown in figure 5.13 and its implementation is shown in figure 5.14. The scattered and ejected electron detectors are fixed, and the gun moves on what amounts to the surface of a cone, with axis $-\hat{k}_{SC}$, and of half-angle equal to the scattering angle θ_{SC} . This is equivalent to rotating the ejected electron detectors around \hat{k}_{SC} while keeping the gun and scattered electron detector fixed. Thus as the gun position is varied from $\phi = 0 \rightarrow 180^\circ$ the ejected detector on the left effectively varies from $\phi' = 0 \rightarrow -180^\circ$, and the ejected detector on the right effectively varies from $\phi' = 180 \rightarrow 0^\circ$, with a combined range equal to the full $\phi' = 0 \rightarrow 360^\circ$ of a plane. To achieve this geometry the electron gun has been mounted to an arm that is in turn attached to a shaft, the axis of which is aligned with the scattered electron detector (see figure 5.14).

Trial experiments were carried out using the original fixed gas nozzle. For small to moderate scattering angles, and perfect alignment between the electron and atomic beams, the change in interaction region volume is expected to be small (less than 10%) as the gun is moved. However, we found that the scattered electron count rate, which should have echoed this change since θ_{sc} is constant, in fact varied by more than a factor

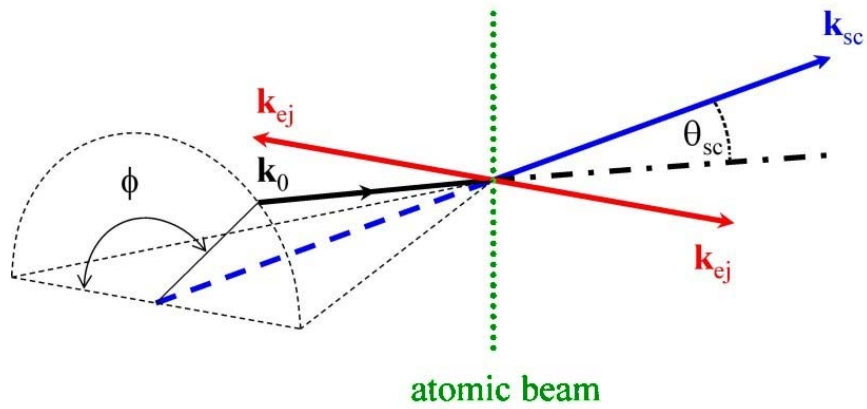


Figure 5.13: Geometry of the modified apparatus. The incident \mathbf{k}_0 , and detected ejected \mathbf{k}_{ej} and scattered \mathbf{k}_{sc} electron directions are as indicated. The atomic beam is directed upwards.

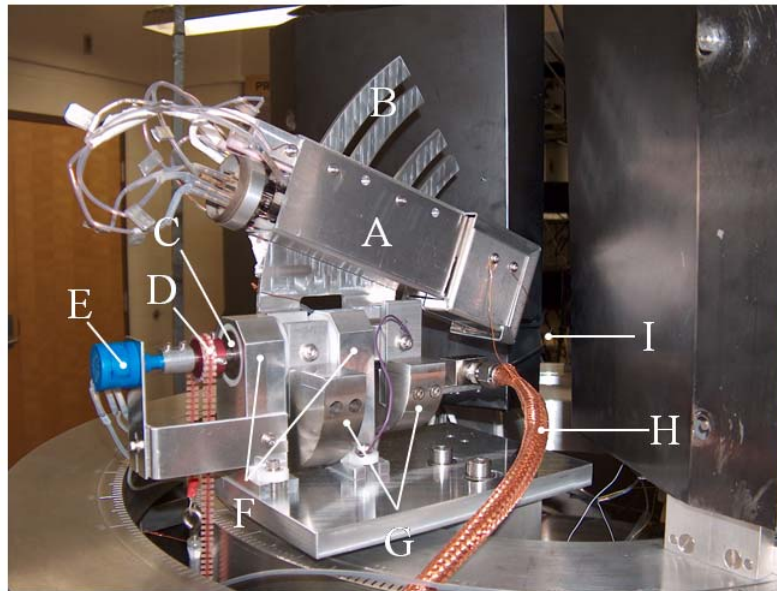


Figure 5.14: Photograph of the modified electron gun/gas nozzle assembly (A) electron gun (and associated electrostatic shielding), (B) mounting arm, (C) shaft, (D) belt driven gear, (E) potentiometer (for position sensing), (F) shaft supports, (G) counter weights, (H) gas supply hose, and (I) gas nozzle.

of two. We believe this was due to small misalignments between the electron and atomic beams resulting in large changes in the interaction region volume. Therefore the gas nozzle has been mounted on the shaft for the electron gun (i.e., the nozzle moves with the gun) so that the intersection between the electron and gas beams is constant. The nozzle is positioned such that it forms an approximately 45° angle with the axis of the shaft, and is approximately 4 mm away from the interaction region. This distance is necessary to avoid the ejected electron detectors “seeing” the nozzle when ϕ is close to 0° or 180° .

The electron gun is positioned on the arm using special alignment tools that ensure that the conical surface, described by the electron beam as the shaft is rotated, has a vertex which is located at the center of the interaction region (see figure 5.13, and refer to section 5.8.1 for the alignment procedures). The shaft for the electron gun can be rotated through a range of approximately 200° (in figure 5.13 this corresponds to $-10^\circ \leq \phi \leq 190^\circ$). A typical experiment involves making measurements with the electron gun at various positions ($0^\circ \leq \phi \leq 180^\circ$). As stated above, having two, diametrically opposed, ejected electron detectors means that as the shaft is rotated through 180° , combining the spectra obtained from the detectors yields an angular distribution that covers the entire 360° of a plane. In fact, mirror symmetry in the scattering plane means that the angular distributions obtained by the two ejected electron detectors should be mirror images of one another. Thus having two ejected electron detectors in our configuration not only increases the rate at which we obtain data, but also allows us to compare the two detectors and determine possible instrumental effects.

Movement of the electron gun is accomplished using a microprocessor controlled stepper motor external to the vacuum chamber. The motor drives a rotary feedthrough followed by a drive belt that couples the feedthrough to the shaft for the electron gun. A pair of counterweights (one fixed, the other adjustable) are attached to the electron gun shaft to minimize the required torque. Despite the relatively low torque required, we experienced problems with drive belt slippage until we installed a W.M.Berg Flex-E-Belt® [30]. The angular position of the electron gun shaft is determined using a potentiometer, attached to the shaft, that is read by the microprocessor.

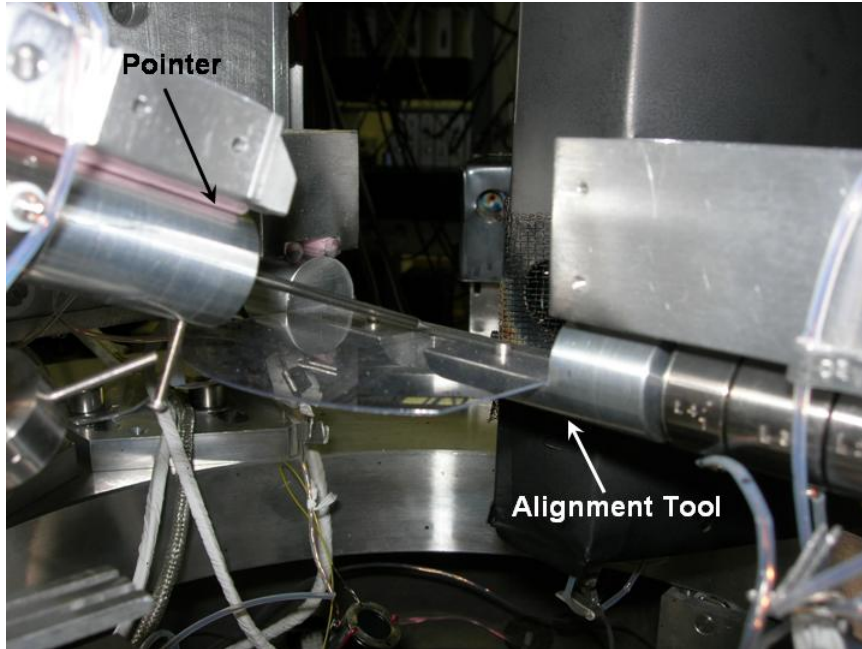


Figure 5.15: Aligning the axis of rotatable gun mount and the gun angle. The alignment tool has been mounted to the optical benches for the ejected electron detectors (after removal of the nose cones). The pointer has been mounted in place of the nose cone and final lens element of the electron gun.

5.8.1 Alignment

The mechanical alignment of the rotatable gun mount (henceforth simply referred to as the *mount*) must ensure that

- a. the axis of the shaft is coaxial with the optics for the scattered electron spectrometer (this ensures that the scattering angle will be constant).
- b. the conical surface, described by the electron beam as the shaft is rotated, has a vertex which is located at the center of the interaction region (this ensures that the gun is pointed at the proper location for the interaction region, see figure 5.13).
- c. the gun is mounted at the correct angle (i.e., the scattering angle will be correct).
- d. the gas nozzle is oriented so that the interaction region is situated correctly.

There are three tools used to accomplish these tasks: an alignment tool, a pointer, and a plug gauge (figure 5.15 shows the alignment tool and pointer, figure 5.16 shows the

pointer and plug gauge). Alignment begins by positioning the ejected turntable at 90° , removing the nose cones of the two ejected detectors, and then mounting the alignment tool to the optical benches of the two detectors so that it is centered (see figure 5.15). If the two ejected spectrometers and the scattered spectrometers are properly aligned then the center spot on the alignment tool will be approximately $1/16$ in. below the ideal location for the interaction region (see figure 5.17). Next the nose cone and final lens element of the electron gun are removed and the pointer is mounted to the gun's optical bench (figure 5.15). To check the height of the mount, rotate the gun to $\phi = 0^\circ$. The diameter of pointer shaft is $7/64$ in., so if the shaft is just above the alignment tool (i.e., $1/64$ in.) then the mount is at the correct height (to date the shaft mounts have not required any shimming to meet this requirement). The alignment tool has a built in protractor. The angle indicated by the intersection of the pointer and the scale on the protractor will, once items a and b are satisfied, be the scattered angle; but for now I will refer to it as β . If the shaft of the mount is coaxial with the scattered optics then the scattering angle will be constant as the electron gun is moved. We check the alignment of the shaft by noting what β is when the mount is at $\phi = 0^\circ$ and $\phi = 180^\circ$, and move the mount until β is the same at both positions ("same" in this case means within $15'$). We have (hopefully) ensured that the shaft is coaxial with the scattered optics (item a in the above list).

Items b and c are accomplished together by extending the pointer so that the point is above the middle of the center dot of the alignment tool, and adjusting the position of the electron gun on the arm so that the angle indicated on the protractor is as desired. Of course the shaft is repeatedly rotated between the $\phi = 0^\circ$ and $\phi = 180^\circ$ positions to ensure that the point of the pointer remains in the same place and the β remains the same.

For the final mechanical alignment the alignment tool is removed (one must be careful not to alter the pointer while removing the alignment tool) and a suitably sized plug gauge is placed in the gas nozzle (figure 5.17, note that the nozzle currently being used has a significantly smaller inside diameter, and the plug gauge is therefore thinner and somewhat flexible). The nozzle is then adjusted so that the plug gauge touches the point of the pointer (perfect alignment would have the point touching the *center* of the

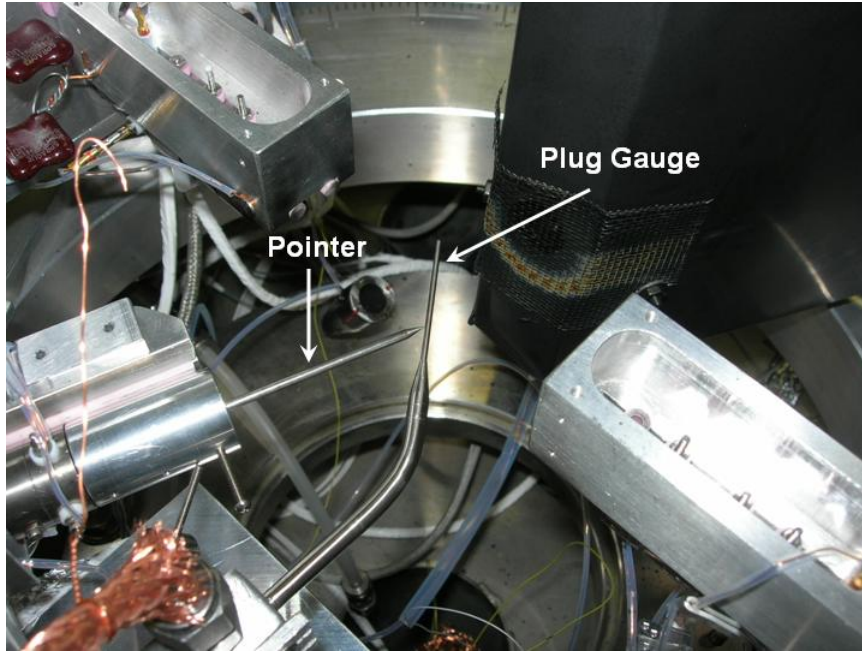


Figure 5.16: Aligning the gas nozzle. The pointer has been mounted in place of the nose cone and final lens element of the electron gun. The plug gauge has been inserted into the end of the gas nozzle (note that this is not the currently used gas nozzle).

gauge, so the gauge should have a slight flex).

5.8.2 Ejected angular distribution

A series of helium direct ionization ejected angular distributions were taken (these were non-coincidence measurements detecting 34.1 eV electrons ejected as the result of ionization from 488 eV incident energy electrons) with the electron gun fixed at $\phi = \{0^\circ, 90^\circ, 180^\circ\}$ (i.e., ejected angular distributions were obtained for each of these values of ϕ). There were three goals for these measurements. The first was to see if the angular acceptance of the ejected spectrometers is significantly asymmetric. As stated previously (section 5.4) the spectrometers do not exhibit cylindrical symmetry (i.e., the coplanar and out-of-plane angular acceptances are not necessarily the same). Simulations (see appendix B) suggest that this asymmetry increases as the angular acceptance of the spectrometer increases, therefore, if there was a detectable asymmetry it would be more pronounced for the ejected electron spectrometers (since the ejected electron spectrometers are tuned to have a greater angular acceptance than the scattered electron spectrometer). The second purpose was to check the operation of the apparatus

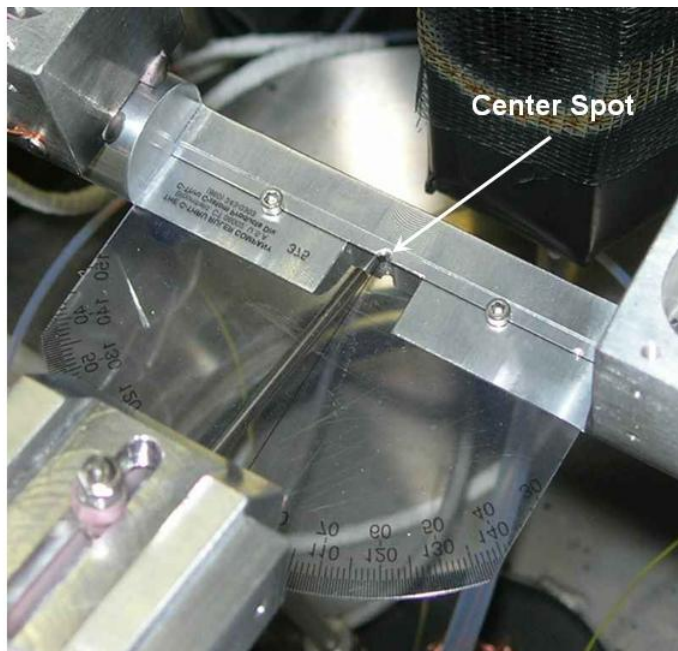


Figure 5.17: Closeup of the alignment tool. The center spot (a black dot on the protractor that is built into the alignment tool) is slightly below the ideal location for the interaction region.

against available benchmark data. Finally, these ejected angular distributions would prove useful in calibrating data taken during our planned out-of-plane experiments.

The terms coplanar and out-of-plane do not pertain to a DDCS (specifically in this case an ejected angular distribution where the scattered electron is ignored) since only one outgoing particle is considered. However, I will continue to use these terms with the understanding that the spectrometers and electron gun are positioned as they would be for a coplanar or out-of-plane ($e, 2e$) experiment. To check the symmetry of the angular acceptance we obtained ejected angular distributions for three different gun positions: $\phi = \{0^\circ, 90^\circ, 180^\circ\}$ (figure 5.18).

When the gun is positioned at $\phi = 90^\circ$ (an out-of-plane configuration) we are able to obtain an angular distribution with a wider range of ejected angles (approximately 69° to 111°) than when the gun is positioned at $\phi = \{0^\circ, 180^\circ\}$ (coplanar configurations). The blue and red error bars in figure 5.18 show the ejected angular distributions for $\phi = 90^\circ$ obtained with the blue and red spectrometers, respectively (recall there are two separate, diametrically opposed, ejected electron spectrometers mounted on a single

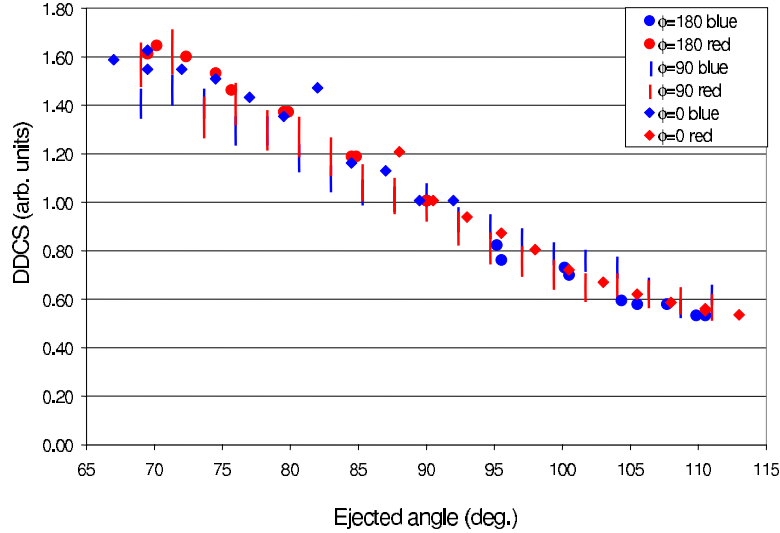


Figure 5.18: Comparison of ejected angular distributions obtained from coplanar and out-of-plane geometries. The distributions have been normalized at 90° .

turntable). The datapoints for $\phi = \{0^\circ, 180^\circ\}$ have been plotted without error bars. I have done this for visual clarity and because the majority of datapoints clearly lie within the angular distribution without having to take into account their error. To create a “coplanar” angular distribution for one of the ejected detectors that spans the same angular range as the “out-of-plane” angular distribution requires combining the data taken for $\phi = 0^\circ$ with that taken with $\phi = 180^\circ$.

Looking at figure 5.18 we can see that for each type (coplanar or out-of-plane) of angular distribution there is reasonable agreement between the two detectors. Minor deviations between the two sets of distributions may result from the gun not being positioned precisely at the desired position; all values of ϕ have a tolerance of $\pm 1/4^\circ$. More importantly, we see that there is only a minimal difference (which falls within the error bars) between the coplanar and out-of-plane angular distributions. Admittedly, distributions having better statistics would be expected to show a more discernible difference between the two geometries, but for our current experiments we judge the asymmetry in angular acceptances to be negligible.

For figure 5.19 I have averaged the distributions for the two detectors with $\phi = 90^\circ$.

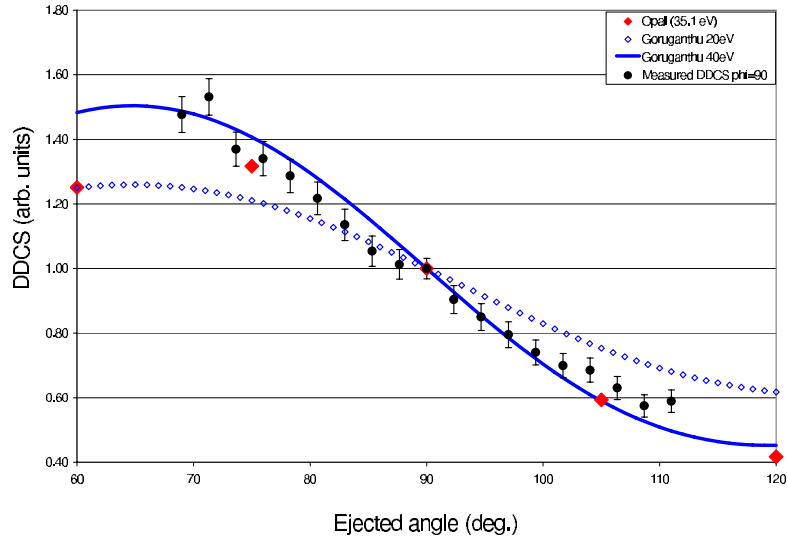


Figure 5.19: Comparison of measured and reported ejected angular distributions. The distributions have been normalized at 90° .

For comparison, I have also plotted some of the results of Opal, et al. [31] which cover this ejected energy (with a slightly different incident energy of 500 eV). However, since the number of angles in their distribution is rather limited I have also included the results of Goruganthu, et al. (specifically the results of a Legendre polynomial fit of their experimental data from [32, table VIII]). Unfortunately, their results are for ejected energies that are substantially lower (20 eV) and slightly higher (40 eV) than ours; but, as a simple check of our apparatus, it seems reasonable to check that our results lie somewhere in between the 20 eV and 40 eV measurements. Looking at figure 5.19 we see that our results do in fact agree well with previously published results.

5.8.3 Calibration

The electron gun and gas nozzle both rotate about the axis of a shaft. As long as the point of intersection between the electron and atomic beams is at a point coaxial with the axis of the shaft, the position of the interaction region will be stationary as the shaft rotates. Unfortunately there is always some amount of misalignment, with the result that the interaction region moves relative to the detectors as the electron gun moves.

This movement of the interaction region results in the efficiency of the detectors varying as a function of electron gun position. Note however, that the size of the interaction volume is fixed since the electron gun and gas nozzle are fixed relative to each other. As a result it is known that the true rate at which events occur is independent of the position of the electron gun.

The measured coincidence spectrum is predominately affected by the ejected electron spectrometers' instrument function. It seems reasonable that these instrument functions might depend on the position of the electron gun (because, for example, misalignments may cause the interaction volume to move relative to the spectrometers, and the coplanar and out-of-plane angular acceptances of a spectrometer may differ). Regardless, we know what the ejected electron angular distribution is supposed to be, and are therefore able to normalize to it. We have found that applying this correction to the coincidence spectrum sufficiently alleviates discrepancies resulting from the ejected electron spectrometers' instrument functions.

Chapter 6

Coplanar momentum transfer dependence

6.1 Introduction

As mentioned in chapter 2 the experimenter generally fixes four of the five parameters in an $(e, 2e)$ experiment and varies the remaining one. Conventional experiments seeking to obtain an angular distribution of the TDCS fix all of the energies and the scattered electron direction (E_0 , E_{sc} , E_{ej} , and \hat{k}_{sc}) while varying the direction from which ejected electrons are detected; i.e., the angular distribution of ejected electrons detected in (delayed) coincidence with electrons scattered into some fixed solid angle is obtained. Since the incident and scattered momenta are fixed, the momentum transfer is also fixed for this type of experiment. The very first $(e, 2e)$ experiments [9] were of this conventional type, and experimenters continue to perform these experiments (e.g., Catoire, et al. [33] or a fairly recent review by Lahmam-Bennani [34]).

In this chapter I will describe a less typical set of experiments where angular distributions of *scattered* electrons detected in (delayed) coincidence with electrons *ejected* (as a result of direct ionization) into a fixed solid angle were obtained. Since the scattered momentum varies (while the incident momentum is fixed) the magnitude and direction of the momentum transfer varies. The magnitude of the momentum transfer varied by almost an order of magnitude ($K = 0.38 \rightarrow 3$ au) for some of these experiments, providing a stringent test of the theoretical understanding of collision dynamics.

While unusual, this is certainly not a unique experiment; early examples can be found in [35] and [36]. A significant difference between the experimental technique used for these experiments and those previously reported by other groups, is that we make measurements for two diametrically opposed ejected electron directions simultaneously. The advantages of this technique have been discussed previously [37, 21] but will be repeated now.

The angular distribution of scattered electrons detected in coincidence with electrons ejected in the fixed direction \hat{k}_{ej} can be expressed using a partial wave expansion:

$$I(\hat{k}_{sc}, \hat{k}_{ej}) = \left| \sum_{\ell, m} A_{\ell, m} Y_{\ell, m}(\hat{k}_{ej}) \right|^2 \quad (6.1)$$

where the $Y_{\ell,m}(\hat{k}_{ej})$ are spherical harmonic functions and the expansion coefficients are $A_{\ell,m} = |A_{\ell,m}|e^{i\delta_{\ell,m}}$. Noting that $Y_{\ell,m}(\hat{z}) = 0$ for $m \neq 0$ I use the freedom to rotate my reference frame to let $\hat{z} = \hat{k}_{ej}$ which simplifies equation 6.1:

$$\begin{aligned} I(\hat{k}_{sc}, \hat{k}_{ej}) &= \left| \sum_{\ell} A_{\ell,0} \right|^2 \\ &= \sum_{\ell, \ell'} |A_{\ell,0}| |A_{\ell',0}| \cos(\delta_{\ell,0} - \delta_{\ell',0}) \end{aligned} \quad (6.2)$$

Our experiments involve ionization from the s -shell, in which case there is direct correspondence between this partial wave expansion and a multipole expansion (i.e., the $\ell = 0$ partial wave term corresponds to the monopole term, $\ell = 1$ to the dipole term, etc.). For high incident energies and small momentum transfer values the $\ell = 1$ (dipole) term dominates. The domination of the dipole term lessens as the value of the momentum transfer increases, and for $K \geq 1$ the remaining terms become as important as the dipole term. In other words, by varying K significantly we provide benchmark data for which theoretical descriptions must properly handle various multipole moments.

To provide even more useful data, it would be desirable to isolate the contribution from the dipole term, and that from the remaining terms. It turns out that this is (to some degree) possible. Looking at equation 6.2 we see that terms having $\ell \neq \ell'$ have parity $(-1)^{\ell+\ell'}$ (with respect to the ejected electron direction) and contain phase information, while terms with $\ell = \ell'$ have even parity and do not contain phase information. Now let us consider a pair of angular distributions (I^+ and I^-) of scattered electrons detected in coincidence with electrons ejected in the fixed direction $+\hat{k}_{ej}$ or $-\hat{k}_{ej}$ [i.e., $I^{\pm} = I(\hat{k}_{sc}, \pm\hat{k}_{ej})$]. It is useful to define symbols for the even and odd parity terms of I^+ :

$$I_e^+ = \sum_{\ell+\ell'=even} |A_{\ell,0}| |A_{\ell',0}| \cos(\delta_{\ell,0} - \delta_{\ell',0}) \quad (6.3)$$

$$I_o^+ = \sum_{\ell+\ell'=odd} |A_{\ell,0}| |A_{\ell',0}| \cos(\delta_{\ell,0} - \delta_{\ell',0}) \quad (6.4)$$

Expressing I^+ and I^- in terms of I_e^+ and I_o^+ yields:

$$I^+ = I_e^+ + I_o^+ \quad (6.5)$$

$$I^- = I_e^+ - I_o^+ \quad (6.6)$$

If we then take the sum ($I^+ + I^-$) and difference ($I^+ - I^-$) of these distributions (which I will hereafter refer to as sum and difference spectra respectively) we get:

$$(I^+ + I^-) \propto I_e^+ \quad (6.7)$$

$$(I^+ - I^-) \propto I_o^+ \quad (6.8)$$

Since the sum spectrum strips off the odd parity terms, the dipole term is enhanced; while the difference spectrum eliminates the dipole term entirely and allows one to examine odd parity crossterms. Hence, by measuring angular distributions for diametrically opposed ejected angles we are able to at least enhance certain terms in the multipole expansion. Further, by taking the ratio of the difference to the sum spectrum, we are able to compare our relative cross-sections to absolute theoretical calculations without having to perform normalization. (So far this ratio has not actually been useful distinguishing between theories as will be shown later).

The experiments detailed in this chapter were performed at two different incident energies, first at $E_0 = 488$ eV then at $E_0 = 150$ eV. At each of these incident energies two different pairs of ejected electron directions were used, $\theta_{ej} = +90^\circ, -90^\circ$ and $\theta_{ej} = +75^\circ, -105^\circ$; making for a total of four experiments. In each case the detected ejected electrons were products of direct ionization and had an energy of $E_{ej} = 34.5$ eV (this was a convenient energy as the apparatus had previously been tuned for obtaining ejected electron spectra with $32 \text{ eV} \leq E_{ej} \leq 41 \text{ eV}$).

For the initial experiment we wanted a (relatively) high incident energy so that exchange and post-collision interaction (PCI) effects would be minimized; 488 eV was the highest incident energy we could obtain without modifications to the apparatus being necessary. The choice of $E_0 = 150$ eV for later experiments was made because trial calculations indicated that a theoretically predicted “zig-zag” feature, that we were unable to resolve at $E_0 = 488$ eV, would be more apparent at lower incident energies (see panel (d) of figures 6.8 and 6.10). Performing experiments with $\theta_{ej} = \pm 90^\circ$ allowed us to determine the relative efficiencies of the two ejected electron detectors since $I^+(\theta_{sc}) = I^-(-\theta_{sc})$. Experiments with $\theta_{ej} = +75^\circ, -105^\circ$ allowed us to examine the asymmetric case where I^+ was near the binary peak while I^- was near the recoil peak.

6.2 Theory

Theoretical calculations of the absolute cross sections for the kinematic regimes covered by our experiments were performed by Chen and Madison [21, 38] and are shown in figures 6.1 through 6.4. The names of three of the types of calculations (PPP, PPC, and PCC) refer to the type of wave (P for plane wave, C for Coulomb wave) used to describe the incident, scattered and ejected electrons respectively (e.g., PPC means that plane waves were used for the incident and scattered electrons, while a Coulomb wave was used for the ejected electron). The PPP calculations are the same as plane-wave Born approximation (PWBA) calculations, while the PPC and PCC calculations are distorted-wave Born approximation (DWBA) calculations. The BBK (standing for Brauner, Briggs and Klar) [39] calculation is a DWBA calculation using a plane wave for the incident particle and Coulomb waves for both outgoing particles (i.e., it is similar to the PCC calculations) and also includes post-collision interactions between the two outgoing electrons. All of the above calculations (PPP, PPC, PCC and BBK) were performed for incident energies of both 488 and 150 eV. Additionally, a BBK calculation that also included exchange effects, labelled as BBKX, was performed for an incident energy of 150 eV to investigate whether such effects are important at this relatively low energy.

A few observations regarding figures 6.1 through 6.4 are in order. Looking at the two sets of calculations for $\theta_{ej} = \pm 90^\circ$ we see that the two members of each pair are mirror images of each other (i.e., $I^+(\theta_{sc}) = I^-(-\theta_{sc})$), reflecting the symmetry (pun intended) for this configuration. Meanwhile the calculations for $\theta_{ej} = +75^\circ, -105^\circ$ are quite dissimilar, as is to be expected since in one case the angular distribution is calculated (relatively) near the binary peak, while the other is near the (less intense) recoil peak. Looking at figures 6.3 and 6.4 we see little difference in the BBK and BBKX plots; conversely, there is a large difference between the PCC and BBK plots, indicating (at least as far as theory reflects reality) that exchange effects are rather minor in comparison to PCI effects at 150 eV incident energy (this is further corroborated when these theoretical values are fitted to the experimental results, see section 6.4). In all cases, the minimum for the theoretical calculations does not occur at $\theta_{sc} = 0^\circ$. This results in the “zig-zag” feature in the $(I^+ - I^-)$ angular distribution (as well as the ratio

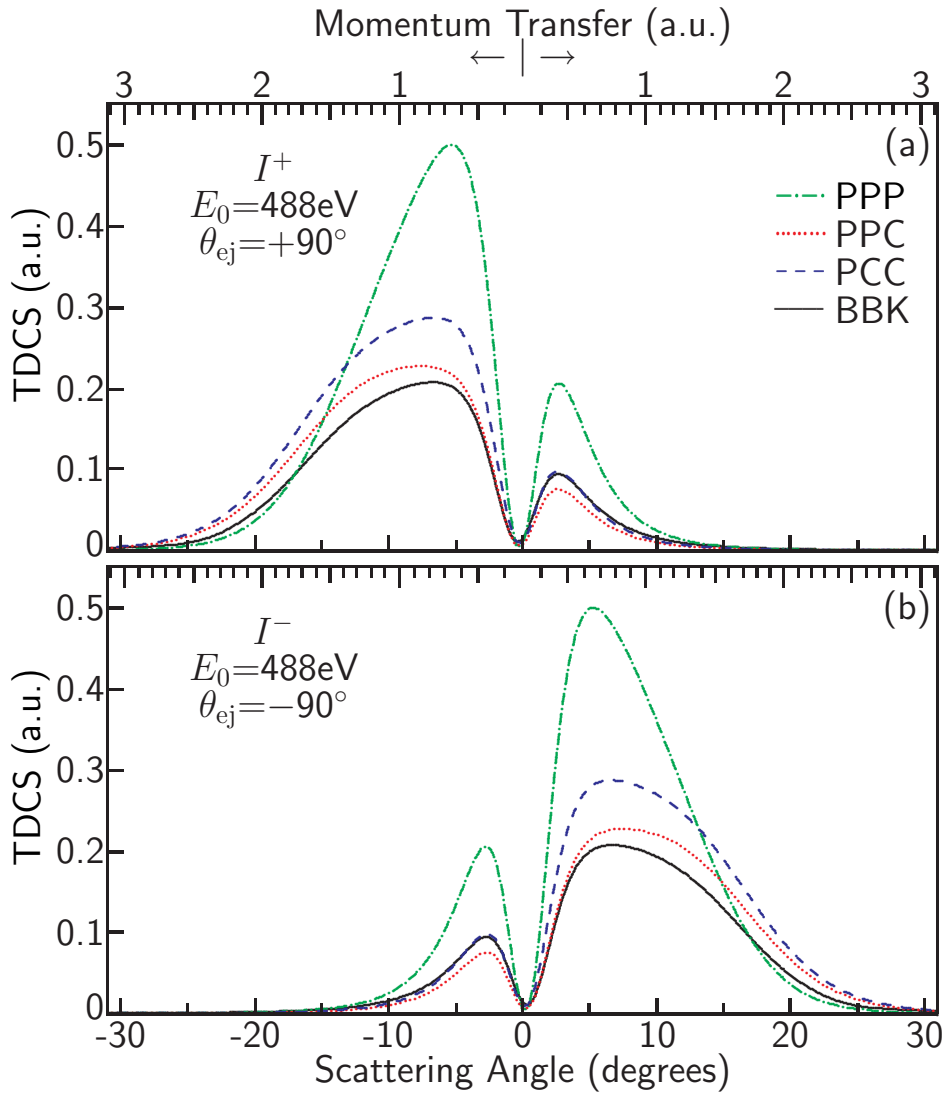


Figure 6.1: Calculated absolute TDCS for the electron impact ionization of helium in coplanar asymmetric geometry as a function of scattering angle for an ejected electron energy of 34.5 eV. The incident electron energy is 488 eV and the ejected electron direction is fixed at (a) $+90^\circ$, (b) -90° . Also shown at the top is the corresponding momentum transfer range; the minimum value (at $\theta_{sc} = 0$) is indicated by the vertical line. The four calculations all use incident plane waves; the scattered and ejected electrons are described by different combinations of plane (P) and Coulomb (C) waves. BBK is a PCC calculation that includes PCI effects.

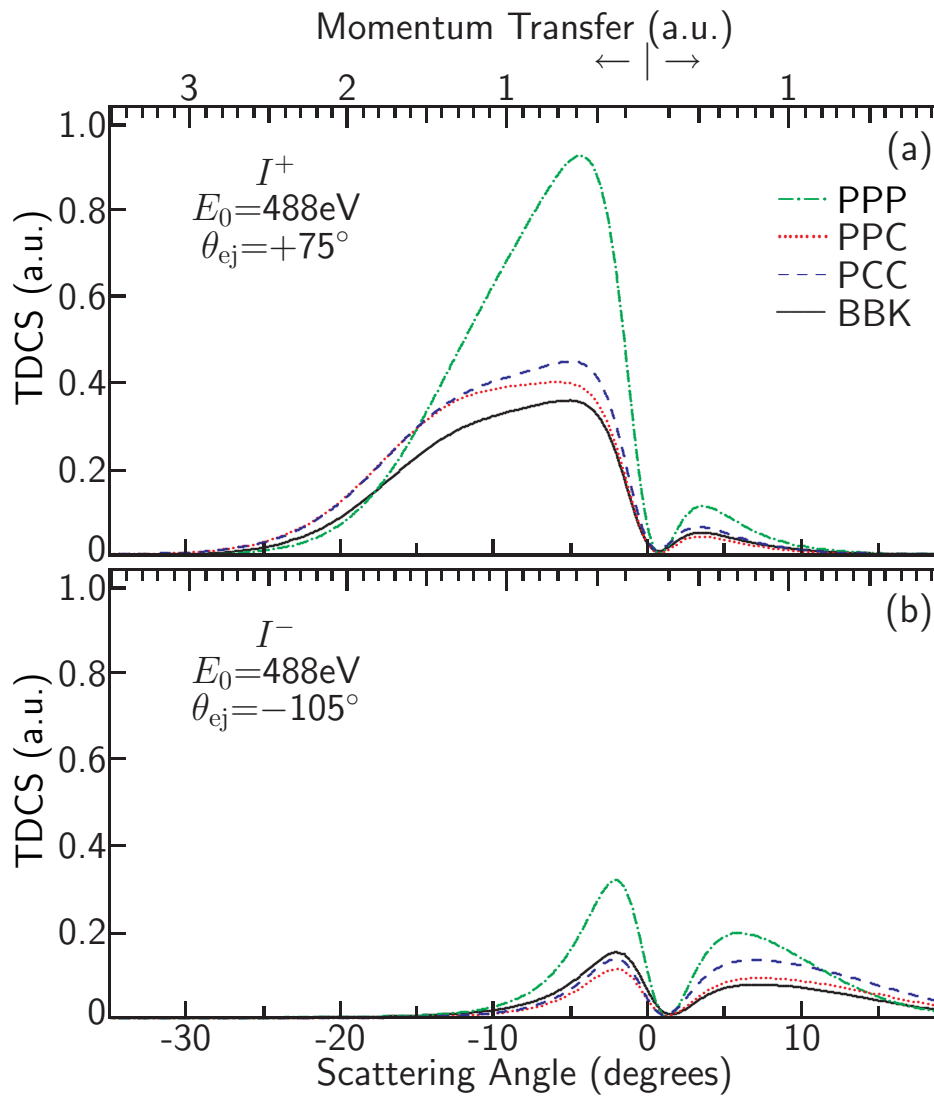


Figure 6.2: As figure 6.1 but for ejected electron directions fixed at (a) $+75^\circ$, (b) -105° .

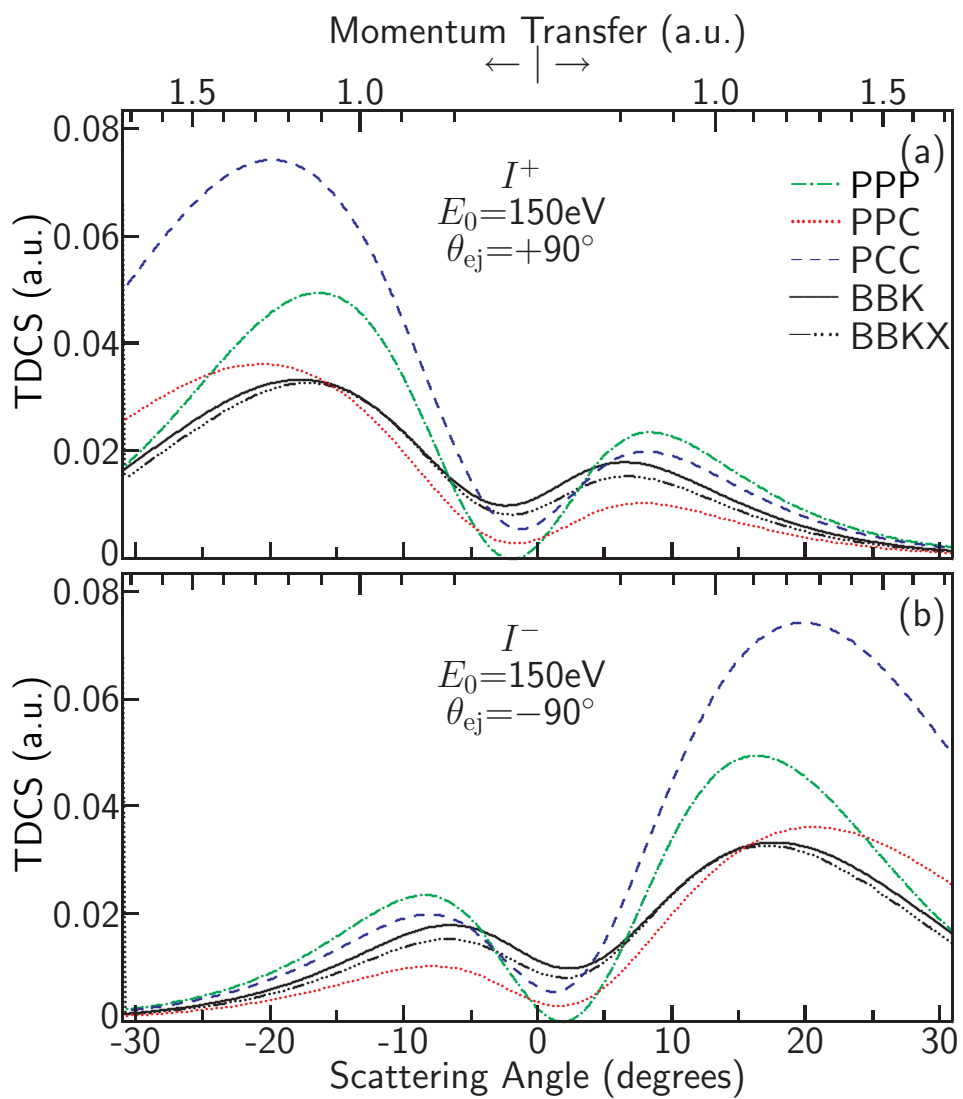


Figure 6.3: As figure 6.1 but for incident electron energy of 150 eV. BBKX is a BBK calculation that includes exchange effects.

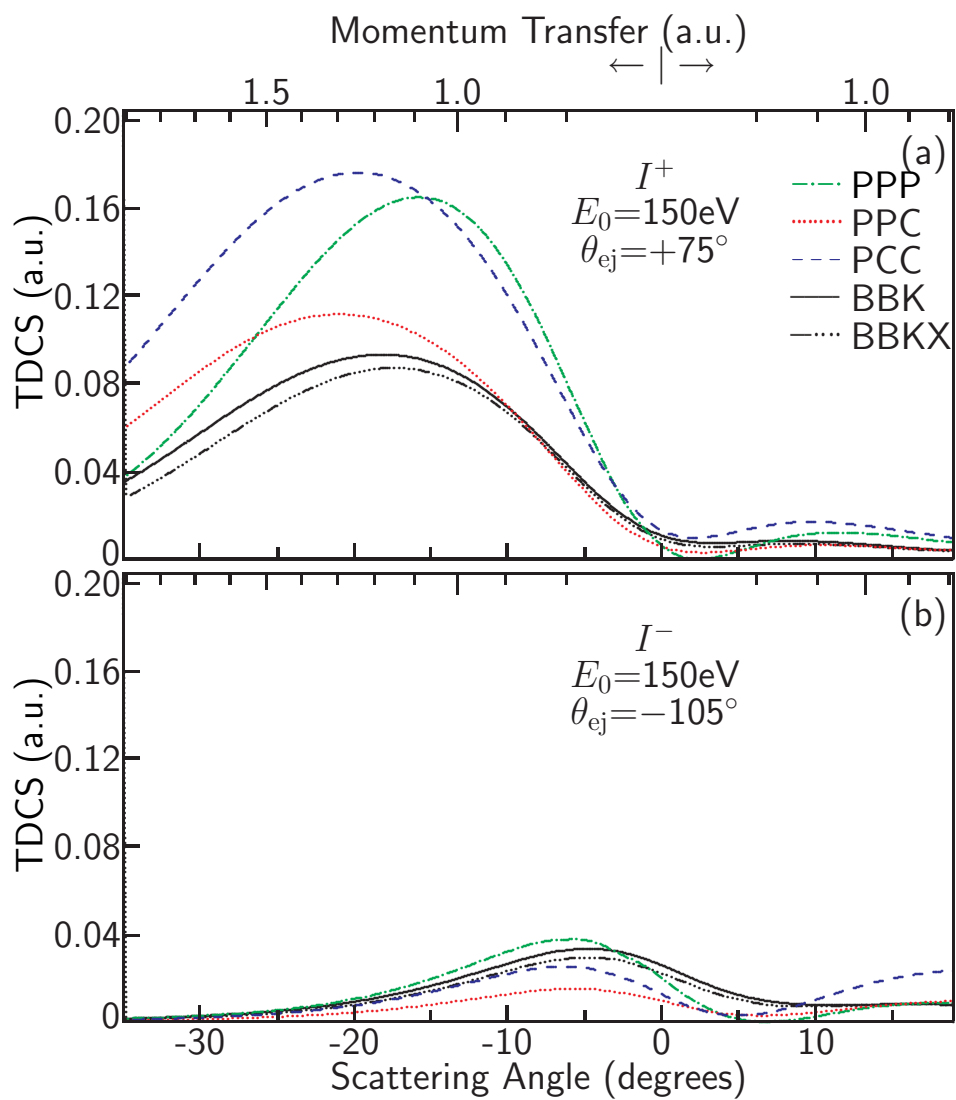


Figure 6.4: As figure 6.3 but for ejected electron directions fixed at (a) $+75^\circ$, (b) -105° .

$(I^+ - I^-)/(I^+ + I^-)$) mentioned in the introduction.

6.3 Experimental details

The angle convention used for our experiments is shown in figure 6.5. Looking down at the apparatus, trajectories that are clockwise from a line corresponding to 0° scattering are positive, while those that are counter-clockwise are negative. While the scattered electron detector is mounted on its own turntable (coaxial and independent from the turntable for the pair of ejected electrons detectors), the range through which it can be positioned is limited by the position of the ejected detectors (i.e., the scattered detector can “bump” into the ejected detectors if it is moved too far one way or the other). With the ejected detectors positioned at $\theta_{ej} = \pm 90^\circ$ the scattered detector could be positioned such that $-30^\circ \leq \theta_{sc} \leq +30^\circ$, while for $\theta_{ej} = +75^\circ, -105^\circ$ the range was $-34^\circ \leq \theta_{sc} \leq +18^\circ$. During an experimental run the scattering angle was repeatedly scanned from the most negative to the most positive angle and back in 2° increments (accumulating data at each angle for approximately 4 minutes) to provide a pair of scans [38].

The two ejected electron detectors have differing efficiencies that must be corrected for when analyzing the data. For a given incident electron energy the correction factor is obtained by comparing the ejected electron angular distributions (angular meaning with respect to the angular position of the *scattered* detector) for the two detectors with $\theta_{ej} = \pm 90^\circ$. This is non-coincident data (i.e., a count indicates an ejected electron detected without regard to whether or not it was coincident with a scattered electron) that is collected as part of each experiment. Ideally we would obtain an angular distribution that is totally flat, since we are not moving the ejected electron detectors. Figure 6.6 shows the angular distributions obtained for $E_0 = 488$ eV. The two distributions are nearly flat. The largest features are at $\theta_{sc} = \pm 6^\circ$; at these angles the incident electron beam strikes the front edge and sides of the electron-optics for the scattered electron detector, causing large numbers of secondary electrons. Summing the counts in each distribution and dividing the larger by the smaller yields a ratio (correction factor) of 1.376. Finding the correction factor for each individual scattering angle (keeping in mind that the ratio is $I_{ej}^+(\theta_{sc})/I_{ej}^-(-\theta_{sc})$ as opposed to $I_{ej}^+(\theta_{sc})/I_{ej}^-(\theta_{sc})$) yields 1.38 ± 0.02 ,

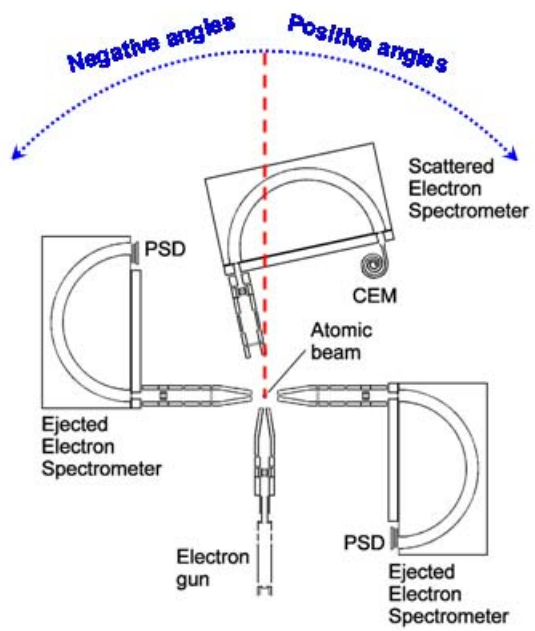


Figure 6.5: Cartoon of the apparatus showing the angle convention used for our coplanar experiments.

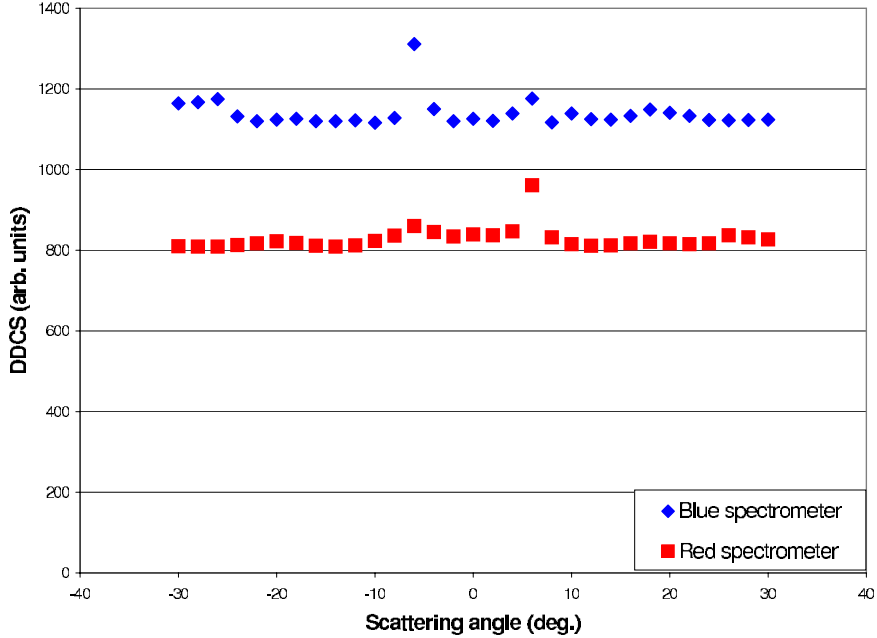


Figure 6.6: Comparison of ejected electron counts as a function of scattering angle. Ideally both distributions would be flat (since the ejected angle is constant).

indicating that although the position of the scattered detector does have some effect on the intensity of the ejected signals, it does not have a significant effect on their relative efficiencies.

The (non-coincident) scattered electron angular distribution should be symmetric about $\theta_{sc} = 0^\circ$. Further, the shape of the distribution should remain stable with time (i.e., the distribution from a scan taken early in an experiment should, within the statistical uncertainties, look like one from a scan taken later in the same experiment; scans would last a couple of hours, experiments lasted several days). This was the case for experiments performed with $E_0 = 488$ eV. However, for $E_0 = 150$ eV the scattered angular distribution was only stable and well behaved (i.e., monotonically decreasing with θ_{sc}) for positive scattering angles. The angular distribution for negative scattering angles changed with time and would eventually have a local minimum around $\theta_{sc} = -6^\circ$. This appears to be the result of contamination (possibly by either diffusion or mechanical pump oil) of the surfaces of one or more electron-optics elements, which in turn caused surface charges to form. Cleaning of the electron-optics would remove/reduce these deleterious effects, but only for several days at best. This was a sufficient amount of time for the experiment with $\theta_{ej} = \pm 90^\circ$ and any effects were minimized by adding

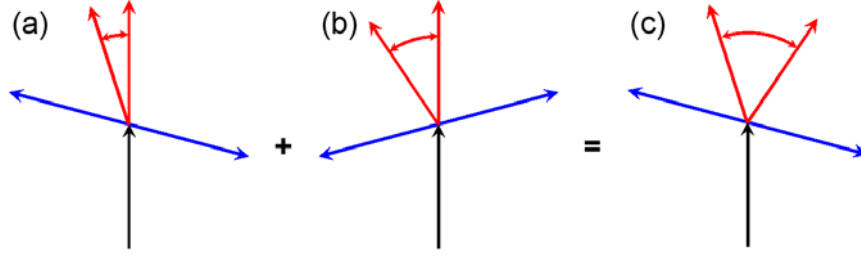


Figure 6.7: Combining two experiments at $E_0 = 150$ eV to obtain the angular distributions for fixed ejected electron directions $\theta_{ej} = +75^\circ, -105^\circ$. For each figure, the incident electron direction is shown in black, the ejected electron directions in blue and the range of scattered electron directions in red. The geometries for the actual experiments are shown in (a) $\theta_{ej} = +75^\circ, -105^\circ$ and $0^\circ \leq \theta_{sc} \leq +18^\circ$, and (b) $\theta_{ej} = +105^\circ, -75^\circ$ and $0^\circ \leq \theta_{sc} \leq +34^\circ$. Symmetry about the incident direction allows the kinematics of (a) and (b) to be combined to yield our desired kinematics: $\theta_{ej} = +75^\circ, -105^\circ$ and $-34^\circ \leq \theta_{sc} \leq +18^\circ$ which is shown in (c).

together data from $\pm\theta_{sc}$, i.e., the angular distribution presented for $E_0 = 150$ eV, $\theta_{ej} = \pm 90^\circ$ is $I(\theta_{sc}) = I^+(\theta_{sc}) + I^-(-\theta_{sc})$. To obtain satisfactory statistics the experiments with $\theta_{ej} = +75^\circ, -105^\circ$ required long run times. We therefore decided to perform the experiment in a way that allowed us to ignore positions of the scattered electron detector where its performance was unstable (i.e., we would ignore negative scattering angles). We did this by dividing the experiment into two parts; for the first part we fixed $\theta_{ej} = +75^\circ, -105^\circ$ and used scattering angles from $0^\circ \rightarrow +18^\circ$, for the second part we fixed $\theta_{ej} = +105^\circ, -75^\circ$ and used scattering angles from $0^\circ \rightarrow +34^\circ$. Symmetry about the incident electron direction allows these two experiments to be combined to obtain the angular distribution for fixed ejected electron directions of $\theta_{ej} = +75^\circ, -105^\circ$ and varied scattering angles $-34^\circ \leq \theta_{sc} \leq +18^\circ$ (see figure 6.7).

Another problem encountered with the experiments performed at $E_0 = 150$ eV was that at $\theta_{sc} = 0^\circ$ for all ejected angles, and additionally at $\theta_{sc} = +2^\circ$ for $\theta_{ej} = +105^\circ, -75^\circ$ (this was “reflected” about the incident direction so that it appears as $\theta_{sc} = -2^\circ$ for $\theta_{ej} = +75^\circ, -105^\circ$ in our results) the data obtained was anomalous, and has been discarded. We conjecture that this was a result of the incident electron beam entering the electron-optics and hemispherical energy analyzer.

E_0 (eV)	θ_{ej} (deg)	BBKX	BBK	PCC	PPC	PPP
488	+90	–	5.8	19	22	85
488	+75	–	2.5	6.4	10	48
150	+90	1.3	1.3	6.5	7.5	2.6
150	+75	1.9	2.3	4.7	6.8	3.9

Table 6.1: Reduced chi-squared values resulting from the fits of theory to experiment shown in panel (a) of figures 6.8 - 6.11.

6.4 Results

Our experimental results, and the corresponding theoretical calculations, are shown in figures 6.8 - 6.11. For each figure, our “raw” data are shown in panels (a) I^+ and (b) I^- . “Raw” in this case means an angular distribution for a single fixed ejected electron direction, i.e., it is not a sum, difference, or ratio of different angular distributions. The sum ($I^+ + I^-$) and difference ($I^+ - I^-$) of each pair of “raw” angular distributions is shown in panels (c) and (d) respectively. Panel (e) shows the ratio $(I^+ - I^-)/(I^+ + I^-)$. For each of these figures the TDCS is given in arbitrary units, set so that the maximum of the experimental I^+ angular distribution has a value of 1.

We measure *relative* cross-sections, with which we want to compare theoretically calculated *absolute* cross-sections; we therefore had to scale the calculations. To find appropriate scaling factors we carried out single parameter reduced chi-squared fits on the I^+ data for each experiment and type of theoretical calculation (for a total of 18 scaling factors). It is interesting that if our data followed Poisson statistics, then it would have been possible to find each scaling factor analytically (i.e., fitting would not be required); the derivation of this analytical expression is given in appendix D. (Scaling factors obtained using the analytical method were close to those found using the fitting procedure). These same fitted scaling factors were then used for the theoretical values for I^- , $(I^+ + I^-)$, and $(I^+ - I^-)$ (i.e., the computations shown in panels (b)-(d)). Since the ratio $(I^+ - I^-)/(I^+ + I^-)$ is intrinsically absolute, the computations shown in each panel (e) did not require scaling.

The chi-squared value for each scaling factor is shown in table 6.1. For a theoretical distribution that perfectly describes some physical measurement (i.e., a perfect theory), the difference between the theoretical and experimental value should be proportional to the statistical uncertainty. Therefore the chi-squared value obtained by comparing

(a perfect) theory with experiment will be immune (within reason) to the statistical uncertainty of the experiment. However, the differences between theoretical values produced by an “imperfect” theory, and experimental values should not, in general, be proportional to the statistical uncertainty; therefore the chi-squared value comparing an imperfect theory and experiment is not immune to changes in the statistical uncertainty of the experiment. Let us examine these statements more closely. A chi-squared value can be expressed as [40, eqn. 12.11]:

$$\chi^2 = \sum_n \left(\frac{\text{observed value} - \text{theoretical value}}{\text{standard deviation}} \right)^2 \quad (6.9)$$

If the *theoretical value* is correct, then there is some probability that the *observed value* will be within one standard deviation of the *theoretical value*, resulting in (observed value - theoretical value)/(standard deviation) being one or less. This is true no matter what the standard deviation (or statistical uncertainty). Since the probability of getting a particular value of (observed value - theoretical value)/(standard deviation) is unaffected by the statistical uncertainty, the χ^2 value should be unaffected by the statistical uncertainty as well (of course there will be statistical fluctuations, but the expected value of χ^2 is unaffected). Now let us suppose the theory (and therefore the *theoretical value*) is wrong; for the sake of illustration let us assume that it is grossly wrong. For small standard deviations the difference (observed value - theoretical value) should be effectively constant (since the theoretical value is grossly wrong), therefore the ratio (observed value - theoretical value)/(standard deviation) should be inversely proportional to the statistical uncertainty and the value of χ^2 will vary as a function of the statistical uncertainty. Presumably all of the theoretical calculations presented here are, at least to some extent, imperfect. This means that although the chi-squared values in table 6.1 provide a figure of merit with which to compare the various theories for a single experiment, one cannot use them to make comparisons across different experiments.

Looking at these chi-squared values, we clearly see that for each experiment a BBK type calculation (BBKX in the specific case of $E_0 = 150$ eV and $\theta_{ej} = +75^\circ$) gave the best agreement with the experimental values. This is not surprising, considering that of the calculations presented here BBK is the only to account for PCI effects. It is interesting to note that there is little difference in the chi-squared values for BBK and

BBKX (the only difference between the two theories being the inclusion of exchange effects) at $E_0 = 150$ eV, while the chi-squared value for BBK is significantly less than that for PCC (the major difference between these theories being that BBK includes PCI effects while PCC does not); this indicates that PCI effects play a much greater role than do exchange effects.

The results from our first experiment, performed with $E_0 = 488$ eV and $\theta_e j = \pm 90^\circ$, are shown in figure 6.8. The range of scattering angles correspond to a range of momentum transfer values $0.38 \leq K \leq 3.4$ au (i.e., the momentum transfer varies by almost an order of magnitude for this experiment). In panels (a)-(c) it is clear that the BBK calculations give the best description of our experimental data. The curves for the PPC and PCC calculations are qualitatively similar to the curve for BBK, the main difference being in the ratio of their positive and negative scattering angle peaks. The PPP calculations yield a qualitatively different looking curve, with a poor fit to the experimental data. In panel (d) the BBK, PCC and PPC calculations yield almost identical results, which are in good agreement with experiment.

The fact that BBK, PCC and PPC give different results for $(I^+ + I^-)$, but the same results for $(I^+ - I^-)$ indicates all three theories correctly calculate the magnitudes and phases of the odd parity cross terms (equation 6.4) but differ in their calculation of the combined multipole cross sections (which do not incorporate a phase) and even parity cross terms (equation 6.3) that appear in the sum [2].

It was our hope that we could use the ratio $(I^+ - I^-)/(I^+ + I^-)$ (shown in panel (e)) to quantitatively compare (and discriminate between) the various theories. However, in this regime all theories give essentially the same result (which agrees well with the experimental data) at small and medium scattering angles. The theories start to diverge at near our maximum scattering angle of $\pm 30^\circ$, where our statistical uncertainties are too large to discriminate between the theories.

As can be seen in panels (d) and (e), the theoretically predicted “zig-zag” feature in the difference and ratio angular distributions cannot be resolved at this incident energy. (Taking data at smaller than 2° increments still did not resolve the feature, presumably because the approximately 1° angular resolution of the scattered electron detector washes out the feature).

The results for $E_0 = 488$ eV and $\theta_{ej} = +75, -105^\circ$, are shown in figure 6.9. The “raw” angular distributions (I^+ and I^- shown in panels (a) and (b)) have significantly different relative intensities because I^+ is in the binary lobe while I^- is in the (much smaller) recoil lobe. Looking at figure 6.9(a) we see that there is good qualitative agreement between all of the theoretical calculations of I^+ , except PPP, and the experimental data.

Let us recall that (i) the theoretical calculations have been fitted to I^+ , and (ii) the relative intensity of I^- is different than that of I^+ . It then follows that comparison of theory and experiment for I^- should give some indication with how well theory treats the binary/recoil ratio; looking at figure 6.9(b) we see that while all of the theories (including PPP) appear to have qualitative agreement, only PPC seems to give good quantitative agreement. It seems a fair statement that none of the theories gives good quantitative agreement over all angles of I^+ and I^- .

Since I^+ is relatively large compared to I^- , the sum angular distribution shown in figure 6.9(c) is similar to that of I^+ (figure 6.9(a)). As for $\theta_{ej} = \pm 90^\circ$ there is a theoretically predicted “zig-zag” feature for the difference and ratio angular distributions which we have not been able to resolve (panels (d) and (e) of figure 6.9).

Figure 6.10 shows the result of an experiment with $E_0 = 150$ eV and $\theta_{ej} = \pm 90^\circ$. For this experiment the I^- angular distribution has been created from the I^+ distribution using the transformation $\theta_{sc} \rightarrow -\theta_{sc}$; the reasons for this were discussed in section 6.3. The experimental data shown in figures 6.10(a) and 6.10(b) are therefore mirror images of each other. The experimental data shows a non-zero minimum for I^+ , which is predicted by all of the theories except PPP. Both BBK and BBKX describe the data well, with BBKX doing a slightly better job describing I^\pm and the sum (figures 6.10(a-c)), and BBK doing a better job describing the difference (figure 6.10(d)). Meanwhile PCC and PPC have problems both with predicting the peak position (surprisingly PPP does a better job predicting this) and with the ratio of the positive scattering angle peak to the negative scattering angle peak amplitude.

At this energy the predicted “zig-zag” feature is approximately twice as wide (width being measured in degrees of scattering angle) as for $E_0 = 488$ eV, and has been resolved in both the difference and ratio angular distributions (see figures 6.10(a,b)).

This brings us to the last of this series of experiments, $E_0 = 150$ eV and $\theta_{ej} = +75^\circ, -105^\circ$; the results of which are shown in figure 6.11. While BBK and BBKX do the best job of describing I^+ , they do the worst job at describing I^- (figures 6.11(a and b) respectively). The sum and difference distributions are not well described by any of the theories except PPP, which does a creditable job [38]. Unfortunately our statistical uncertainties do not allow examination of the “zig-zag” feature in the ratio of the difference to the sum angular distributions in this kinematic regime (figure 6.11(e)).

6.5 Conclusions

A series of four $(e, 2e)$ experiments involving the direct ionization of helium have been described. Two of the experiments were conducted at an incident energy of 488 eV, at which the ratio E_{sc}/E_{ej} was 12.4; and the experiments spanned a range of scattering angles that corresponded to momentum transfer values $K = 0.38 \rightarrow 3.4$. The other two experiments were performed at an incident energy of 150 eV, at which the ratio E_{sc}/E_{ej} was 2.6; and the experiments spanned a range of scattering angles that corresponded to momentum transfer values $K = 0.8 \rightarrow 1.7$. In short the experiments spanned a wide range of kinematic conditions.

Each experiment was compared to four or five sets of theoretical calculations. Examination of table 6.1 suggests that BBK is the best of the theories presented here. However, while the use of the chi-squared values in table 6.1 is justified, one cannot use them blindly. The chi-squared values are affected by the distribution of statistical uncertainties in our data and, as is to be expected, our data generally have regions where the statistical uncertainties are relatively small, and other regions where they are relatively large. Perusal of figures 6.8 - 6.11 indicates that no single theory describes the data flawlessly in all regions [38]; but there is, nevertheless, very good agreement in most cases.

Our overall conclusion is that existing theories describe electron impact ionization of helium quite well over a wide range of coplanar kinematic conditions [38].

However, despite the fact that for a coplanar geometry each of the theories is – like the curate’s egg – good in parts [41], we will see in chapter 7 that investigations out of the scattering plane are more like going into a forest where something seems awry [42,

p. 279].

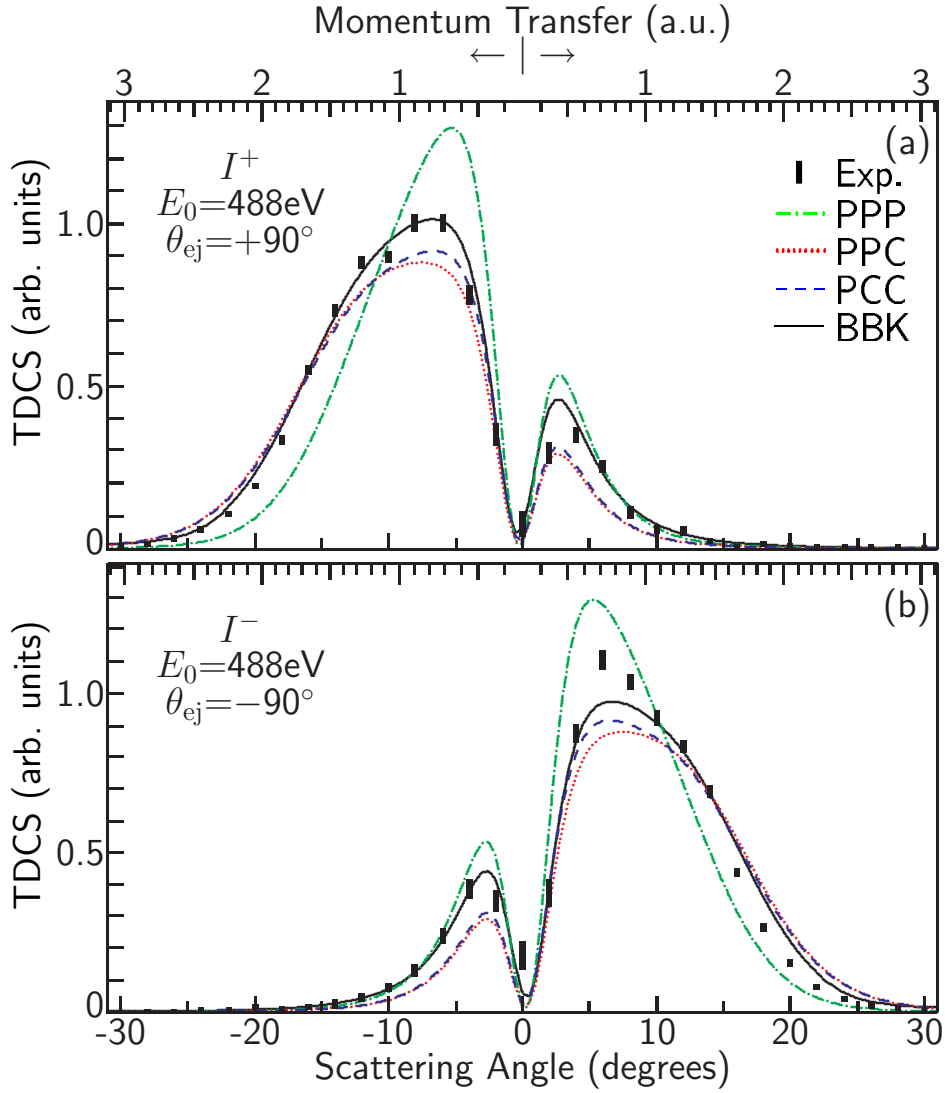


Figure 6.8: Panels (a) and (b): experimental relative TDCS (I^+ and I^-) corresponding to the calculations of figure 6.1 for an incident electron energy of 488 eV and ejected electron energy of 34.5 eV and fixed directions $\pm 90^\circ$. The data are normalized to unity at the maximum in I^+ . Each calculation of figure 6.1 is then separately fitted to the experimental I^+ to provide a set of scale factors that are used and in panels (b)-(d). Panels (c) and (d): the sum and difference of the data in (a) and (b). Panel (e): the ratio of the data in (d) to that in (c).

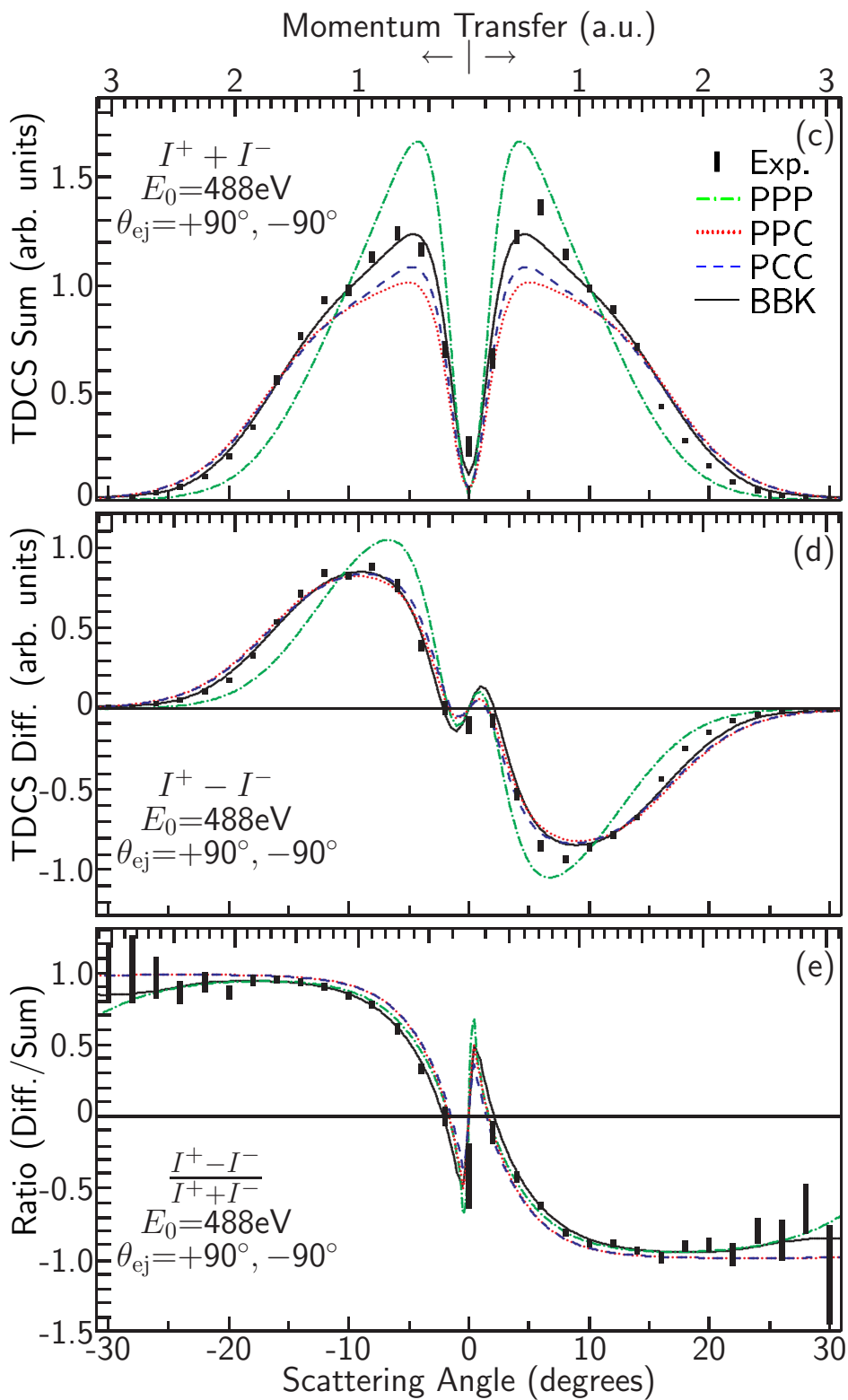


Figure 6.8 continued.

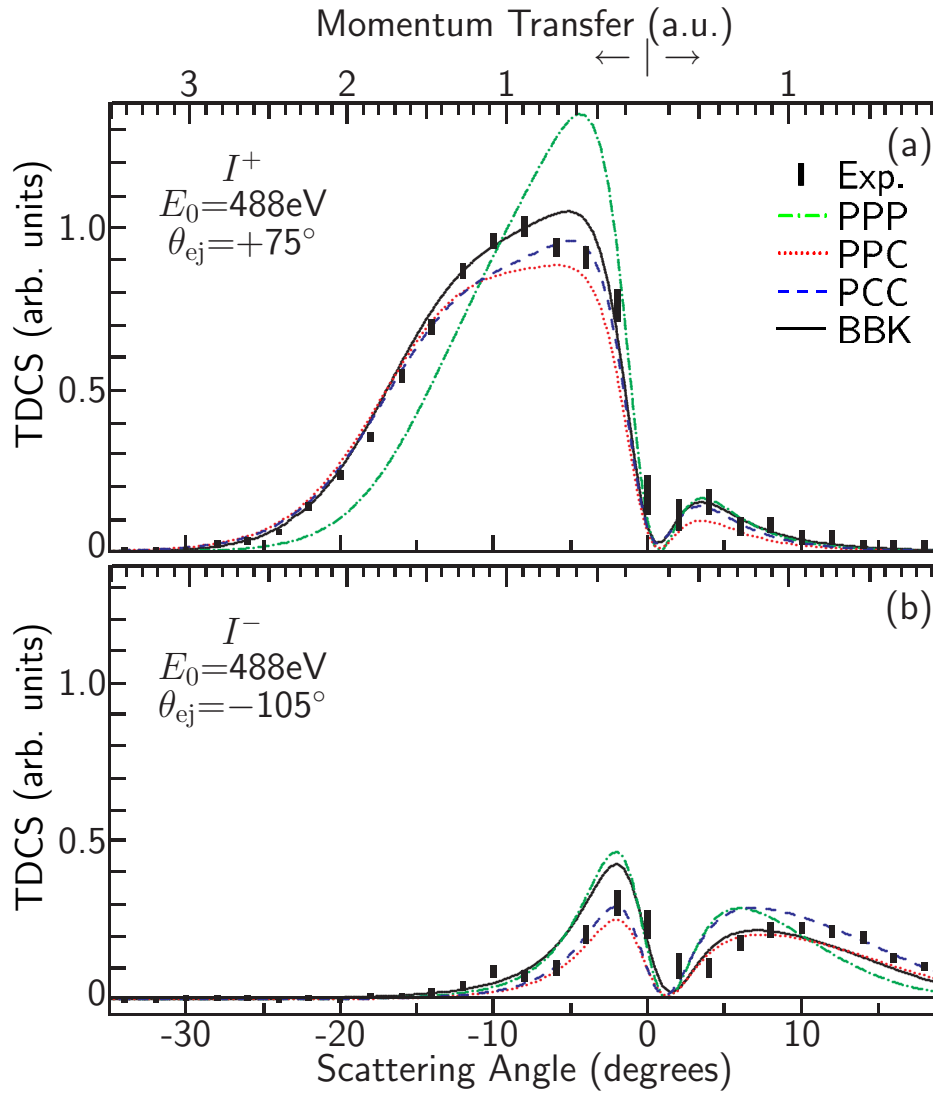


Figure 6.9: As figure 6.8 but for ejected electron directions fixed at (a) $+75^\circ$, (b) -105° . The data are compared with the calculations of figure 6.2.

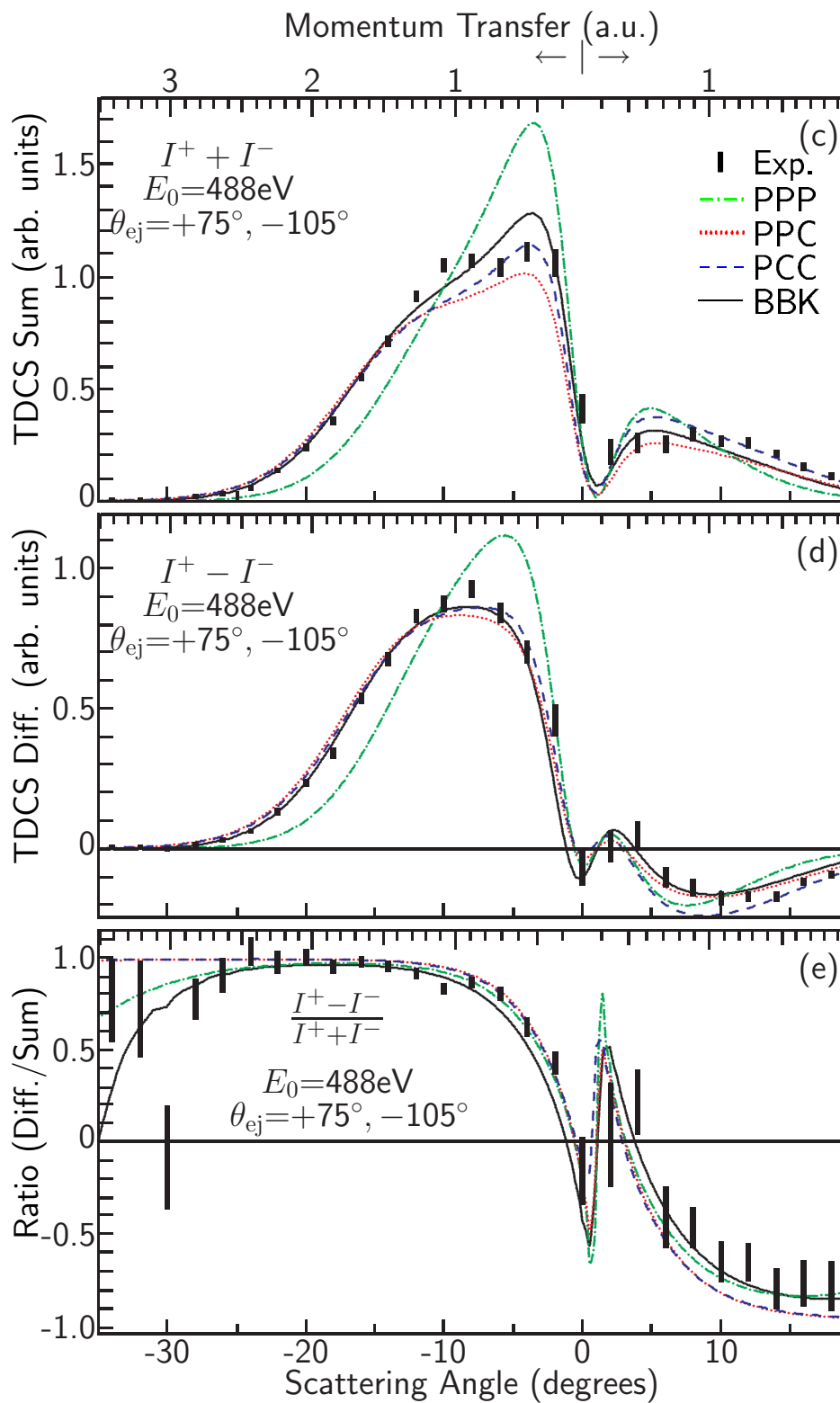


Figure 6.9 continued.

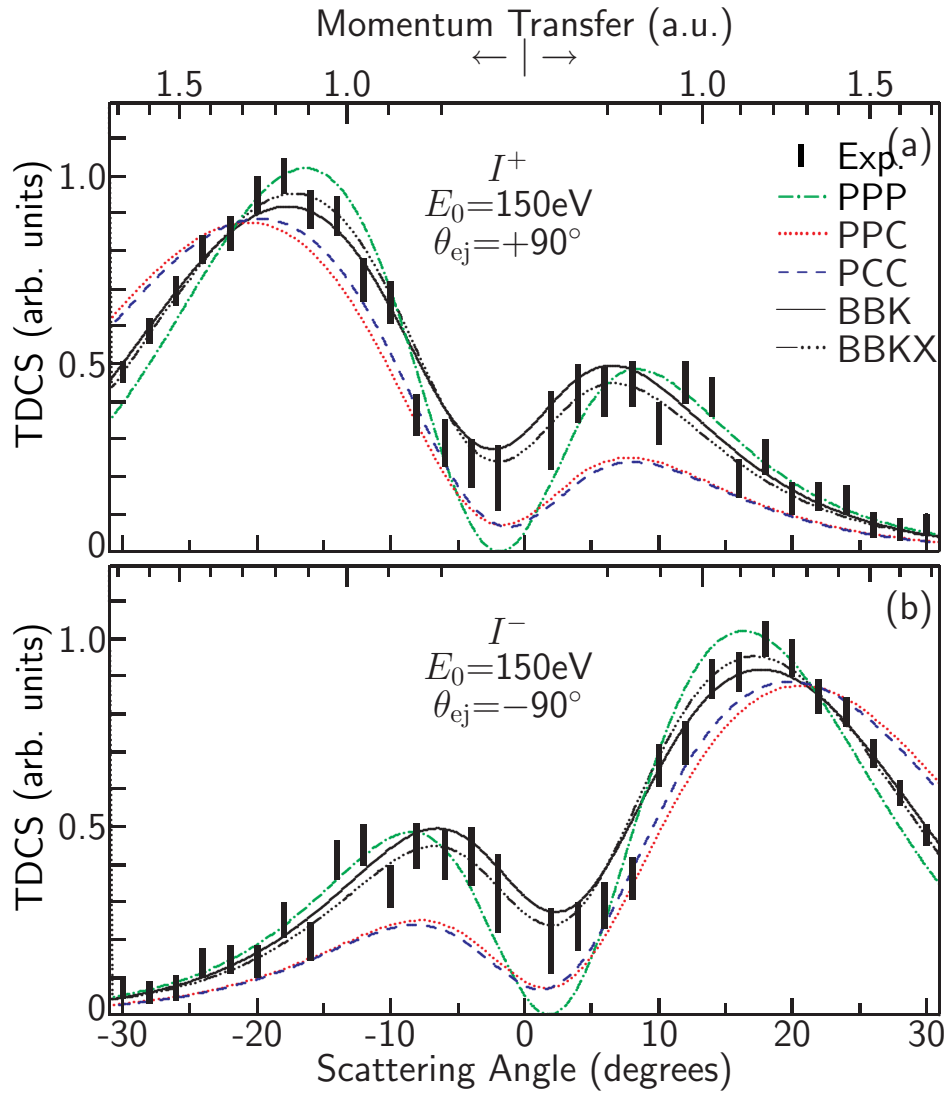


Figure 6.10: As figure 6.8 but for an incident electron energy of 150 eV. The data are compared with the calculations of figure 6.3.

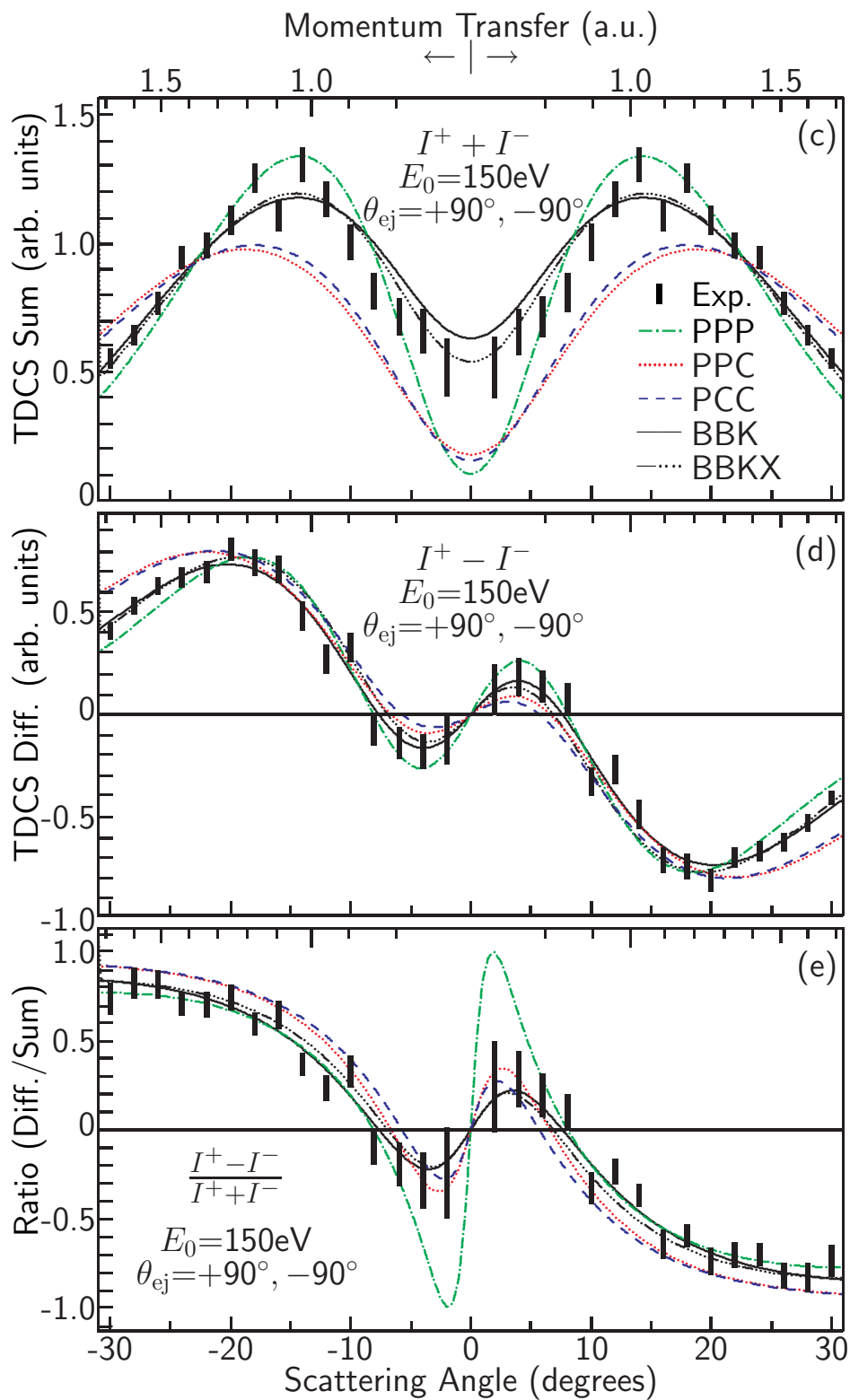


Figure 6.10 continued.

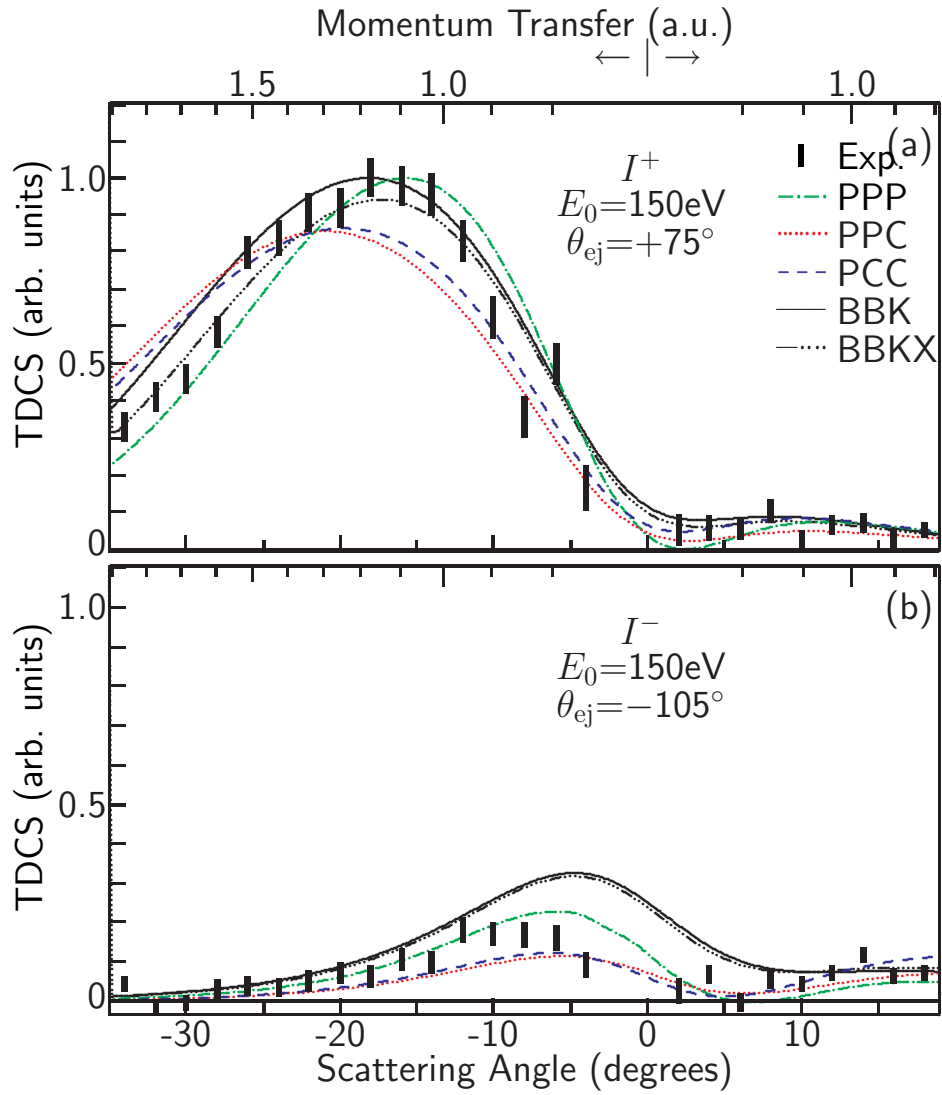


Figure 6.11: As figure 6.10 but for ejected electron directions fixed at (a) $+75^\circ$, (b) -105° . The data are compared with the calculations of figure 6.4.

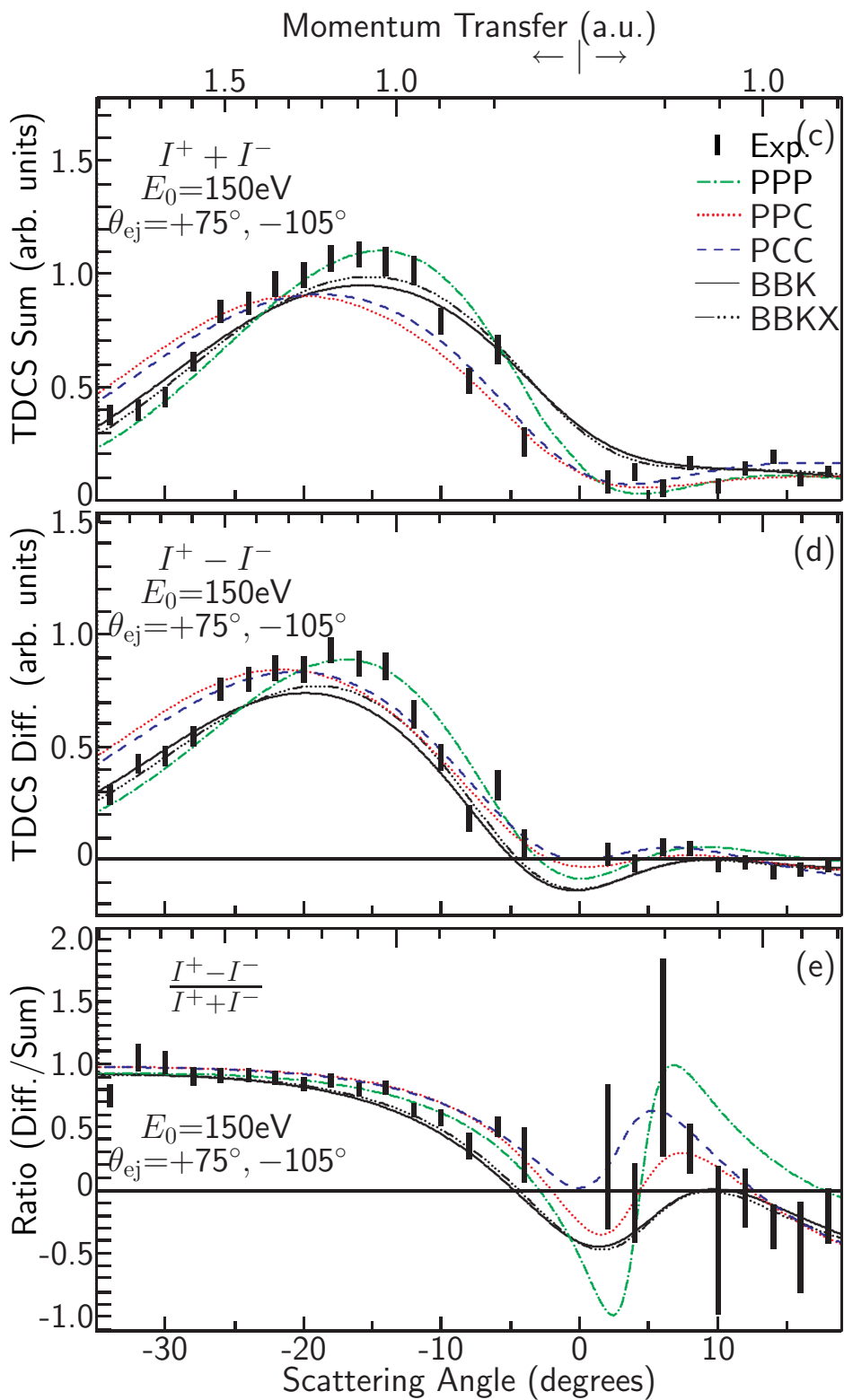


Figure 6.11 continued.

Chapter 7

Out of plane studies

7.1 Introduction

In chapter 6 I described a series of coplanar ($e, 2e$) experiments that were well described by theory. In fact, by the dawning of this millennium most atomic theorists (not to mention the various funding agencies) would probably have considered it a foregone conclusion that theory would accurately describe scattering from helium atoms (at least for relatively high incident particle energies).

However, over the past few years there have been several kinematically complete experiments incorporating an out-of-plane geometry and involving charged particle impact ionization of a variety of atomic targets. These experiments measured the angular distribution of ejected electrons detected in coincidence with incident particles scattered through a fixed angle. Examples where data were obtained using COLTRIMS (COLD Target Recoil-Ion Mass Spectroscopy [43]) spectrometers include single ionization of helium by C^{6+} impact [44], 102 eV electrons [45], and 1 keV electrons [46]. An example where data were obtained using a more traditional spectrometer involves single ionization of magnesium by 400 – 3000 eV electron impact [47]. Each of these studies has shown that while theoretical descriptions of coplanar experiments tend to be very good, there are large discrepancies in their description of out-of-plane experiments, providing ample motivation for further experimental studies.

The majority of recent out-of-plane experiments have involved COLTRIMS spectrometers. The ability of these spectrometers to simultaneously collect data spanning a solid angle of (practically) 4π for low energy electrons makes them a superb tool in many regimes. It may seem that these spectrometers have made traditional spectrometers obsolete. However, their ability to collect data through a large solid angle depends on the energy of the detected electrons being relatively low. One should also note that although the coincidence rates are significantly higher than for a traditional ($e, 2e$) spectrometer, the rate *is* limited (generally, COLTRIMS requires low electron beam fluxes); with this in mind, the fact that the entire 4π angular distribution (across a wide range of energies) is being collected simultaneously means that one may still have

long run-times when looking at events with small cross-sections (since most of the large amount of data being obtained are from other events). For these reasons traditional spectrometers, which can reject unwanted events and may therefore operate at high electron beam intensities, may still be the tool of choice when working in many regimes.

In this chapter I will present the first out-of-plane ($e, 2e$) ejected electron angular distributions on autoionizing levels: the three singlet He levels $(2s^2)^1S$, $(2p^2)^1D$, and $(2s2p)^1P$ [48]. Additionally, data will be presented for direct ionization of helium (where the ejected electron energy is 34.1 eV; this energy is between, but well separated from, the 1S and 1D autoionizing resonances). These experiments were performed with a traditional ($e, 2e$) spectrometer (modified for out-of-plane operation as described in section 5.8) using 488 eV incident electrons.

One of the original motivations for these experiments was to investigate the possibility that the disagreement between theory and experiment is caused by a failure of theory to take into account higher order effects, especially a two-step mechanism proposed by Schulz, et al. [44]. Their proposal was that some significant number of projectile–atom interactions involved two scattering events. The first event is a binary projectile–electron interaction resulting in single ionization of the atom. In the second event the projectile elastically scatters from the ion core, with additional momentum being transferred. Essentially this means that the observed scattering plane is not the same as the scattering plane for the interaction that caused the ionization of the atom. At our relatively high incident electron energies the behaviour of this second scattering event should be significantly different depending on whether the first event causes direct ionization or autoionization. This is because the doubly excited state that leads to autoionization is relatively long lived, and the incident electron will have typically traveled several hundred atomic diameters before the autoionizing state decays to the continuum [48]; i.e., the target of the second scattering event will be significantly different depending on which ionization process is involved. It should be noted that Foster, et al. [49] have claimed that the three-distorted wave (3DW) approach does include such higher-order effects. Regardless, it is our hope that these experiments will provide insight into the importance of such effects.

Straightforward direct ionization of helium can be reduced to a three-body problem

because the 1s electron common to the ground state atom and the ion acts as a spectator [50]. Electron impact autoionization of helium involves both direct ionization and doubly excited states (a four-body process). A further motivation for our experiments is to test theoretical treatments of four-body dynamics.

7.2 Theory

For each angular distribution we also present a Born type calculation. For our direct ionization data this is a straightforward first Born approximation (FBA) calculation. For each of the autoionizing levels we use a formalism developed by Balashov, et al. [16]. Atomic units will be used in this section unless otherwise specified. The TDCS in the vicinity of an isolated autoionizing resonance can be expressed as:

$$\frac{d^3\sigma}{d\hat{k}_{ej} d\hat{k}_{sc} dE_0} = \frac{4}{K^4} \frac{k_{sc}}{k_0} |f(\mathbf{k}_{ej}, \mathbf{K})|^2, \quad (7.1)$$

The scattering amplitude $f(\mathbf{k}_{ej}, \mathbf{K})$ can be expressed as a sum of the amplitudes for direct ionization, and for excitation and decay of the doubly excited state. Recalling equation 4.32, this expression of the amplitude can be written as:

$$f(\mathbf{k}_{ej}, \mathbf{K}) = \sum_{\ell} \langle \varepsilon, \ell | T | i \rangle + \langle \varepsilon, L | T | i \rangle \frac{q_L - i}{\epsilon_L + i}, \quad (7.2)$$

where q_L is the Fano profile index (see equation 4.29), and ϵ_L is the reduced energy (see equation 4.28) which indicates the energy away from the resonance position in units of the resonance halfwidth $\Gamma/2$. The partial wave $\langle \varepsilon, L | T | i \rangle$ can, in turn, be expressed as:

$$\langle \varepsilon, L | T | i \rangle = c_L P_L(\cos \theta_0), \quad (7.3)$$

where P_L is a Legendre polynomial, θ_0 is the angle between the ejected electron and momentum transfer directions (i.e., $\cos \theta_0 = \hat{k}_{ej} \cdot \hat{K}$) and c_L is given by:

$$c_L = \frac{\int t(\vec{k}_{ej}, \vec{K}) P_L(\cos \theta_0) d\hat{k}_{ej}}{\int P_L(\cos \theta_0)^2 d\hat{k}_{ej}} \quad (7.4)$$

where

$$t(\vec{k}_{ej}, \vec{K}) = \sum_{\ell} \langle \varepsilon, \ell | T | i \rangle \quad (7.5)$$

The dimensionless ratio $c_L / \sqrt{\int t^2 d\vec{k}_{ej}}$ was calculated as having the values 0.012, 0.127, 0.104 for $L = 0, 1, 2$, respectively [48].

Table 7.1: Helium autoionizing levels and relevant parameters obtained from the literature [51, 52, 53].

	E_L (eV)	E_{ej} (eV)	Γ_L (meV)
$2s^2\ ^1S_0$	57.84	33.25	120
$2p^2\ ^1D_2$	59.91	35.32	57
$2s2p\ ^1P_1$	60.15	35.56	38

7.3 Experimental Details

Table 7.1 gives details of the three doubly excited states we have examined. In order to increase count rates we have purposefully decreased our resolution to approximately 120 meV; this value is based on the fitting of non-coincidence ejected electron energy spectra (taken with the current configuration and at a variety of electron gun positions) to a Fano profile. The Fano profile is expressed using Shore parameters, and there is a fitting parameter for the resolution (which is folded with the Fano profile). For our experiments we are integrating over an energy range of approximately 480 meV, which covers each resonance entirely.

Figure 7.1 shows a cartoon of a PWBA calculation (with $K \approx 0.7$ au) of the ejected electron angular distribution for direct ionization. Note that the value of K used for this figure is substantially different than the one used for our actual experiments (0.7 au for the figure versus 2.1 au for the experiment), and was chosen to provide a good illustration of the binary and recoil lobes. The value of K used in our experiments leads (for direct ionization) to an angular distribution with a large binary lobe, but an insignificant recoil lobe. The geometry of our experiment is such that we are covering the entire 2π of plane III in this figure (the plane is outlined in blue). This plane is perpendicular to the scattering plane (labeled as I, and outlined in red) and contains the momentum transfer direction. (For comparison purposes, the out-of-plane cuts shown by Schulz, et al. [44] and Dürr, et al. [46] correspond to plane II in figure 7.1).

The kinematics for these experiments are such that the scattered electron direction and the momentum transfer vector are perpendicular (and as a result the plane in which we are making our measurements is perpendicular to the scattering direction as well as the scattering plane). The scattering angle that allows for these kinematics satisfies the

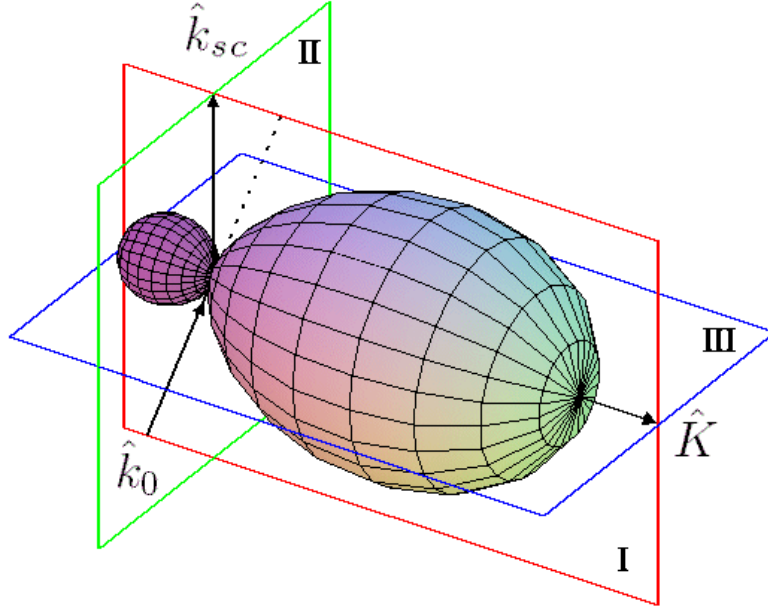


Figure 7.1: Cartoon of a PWBA calculation of the ejected electron angular distribution for direct ionization.

relationship:

$$\theta_{sc} = \arccos \sqrt{1 - \frac{E_L}{E_0}} \quad (7.6)$$

where E_0 is the incident electron energy and $E_L = E_0 - E_{sc}$ is the energy lost by the incident electron (E_{sc} is the scattered electron energy). The magnitude of the momentum transfer is then $K = \sqrt{2E_L}$ and is independent of the incident energy. The values of these various kinematic parameters used for our experiments are given in table 7.2.

Table 7.2: Basic kinematic parameters for our experiments.

Parameter	Value
E_0	488 eV
E_L	60 eV
θ_{sc}	20.5°
K	2.1 au

During an experimental run the gun (detailed in section 5.8) was repeatedly scanned from $\phi = 0^\circ \rightarrow 180^\circ$ and back in 15° increments to provide a pair of scans. Looking at figure 7.2 we see that for $\phi = 0^\circ$ all of the vectors are coplanar. We also see that the ejected detector at $+90^\circ$ (using the convention for positive and negative angles shown in figure 6.5) is detecting electrons ejected in the same direction as the momentum transfer (i.e., $I^+(\phi = 0^\circ) = I^+(\hat{K})$) and the detector at -90° is detecting ejected electrons in the opposite direction (i.e., $I^-(\phi = 0^\circ) = I^-(-\hat{K})$). As $\phi = 0^\circ \rightarrow 180^\circ$ we have the detector at $+90^\circ$ making measurements in plane III of figure 7.1 from \hat{K} counter-clockwise to $-\hat{K}$ while the other detector makes measurements from $-\hat{K}$ counter-clockwise to \hat{K} ; the entire 2π radians of the plane are covered. Since there is mirror symmetry about the scattering plane, we combine the results from the two ejected electron detectors to create a single ejected angular distribution spanning 180° .

Coincidence data was accumulated for approximately 20 minutes per angle per scan. This amount of time was chosen as a (rather arbitrary) compromise between the need to have many short scans (so that changes in apparatus performance would be “spread” over all of the angles) and the desire to maximize the amount of time spent taking data (it takes about a minute to rotate the gun mount through 15° , spending 20 minutes at each angle means that approximately 95% of the time is spent taking data).

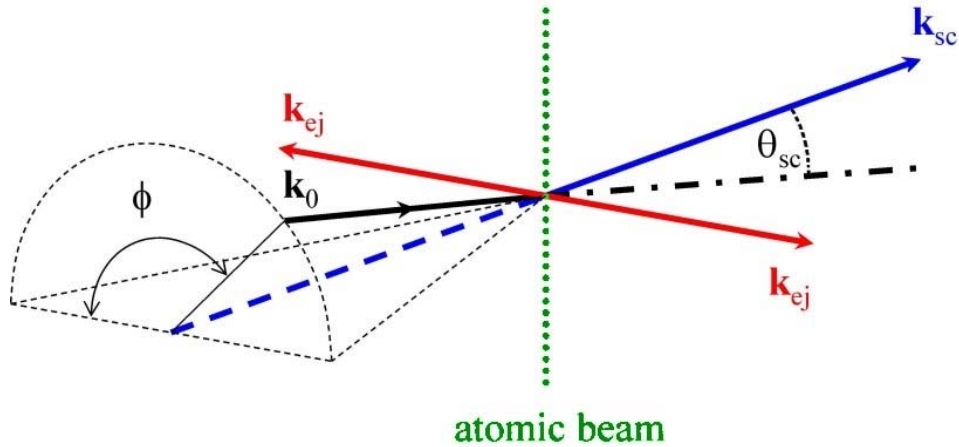


Figure 7.2: Geometry of the apparatus. The incident \mathbf{k}_0 , and detected ejected \mathbf{k}_{ej} and scattered \mathbf{k}_{sc} electron directions are as indicated. The atomic beam is directed upwards.

Table 7.3: Comparison of calculated [54] and fitted values of q^L .

Resonance	Calculated range of values [54]	Fitted value
$2s^2\ ^1S_0$	$(-1 \rightarrow -2.8)$	-15
$2p^2\ ^1D_2$	$(-1.5 \rightarrow -2)$	-6.3
$2s2p\ ^1P_1$	$(-0.2 \rightarrow -0.6)$	-4.8

7.4 Results and discussion

The bars in figures 7.3(a)-(d) are our experimental results for direct ionization and the 1S , 1D , and 1P autoionizing resonances respectively; the associated theoretical calculations are shown as solid lines. The angle $\theta_0 = 0^\circ$ is the momentum transfer direction \hat{K} (binary peak) while $\theta_0 = 180^\circ$ is the direction of $-\hat{K}$. These two positions are in the scattering plane, while all others are out-of-plane. Our experimental results, and theoretical calculations, have been normalized at $\theta_0 = 0^\circ$.

In panel (a) the calculation shown is a PWBA calculation for direct ionization. The calculations shown (as solid lines) in panels (b)–(d) are PWBA calculations making use of the Balashov formalism detailed in section 7.2; these calculations required the fitting of q_L to get good agreement with the data. The fitted values of q_L are shown, along with theoretically predicted values, in table 7.3. Additionally, the PWBA calculation for direct ionization is shown, for the purpose of comparison, as a dotted line in each of the panels showing data for the autoionizing levels.

Looking at figure 7.3(a) we see that the angular distribution for direct ionization has a large binary peak, and a negligible recoil peak. The PWBA calculation describes the experimental data well throughout the angular range, and corroborates that the cross-sections for the recoil peak are tiny. However, figures 7.3(b)-(d) show that for autoionization there is a significant recoil peak. Since the cross-section for direct ionization in the recoil lobe is insignificant, the significant cross-section shown in figures 7.3(b)-(d) is wholly attributable to excitation to a doubly excited state followed by autoionization. This in turn means that for the recoil lobe of the resonances shown, the angular distribution is proportional to its corresponding partial wave (i.e., $I(\theta_0) \propto |\langle \varepsilon, L|T|i \rangle|^2 \propto P_L^2(\theta_0)$, see equation 7.3); therefore it is to be expected that each autoionizing level (or at least the part of its angular distribution that lies within the recoil lobe) will be described by its corresponding Legendre polynomial (e.g., the data for the recoil lobe for the 1P

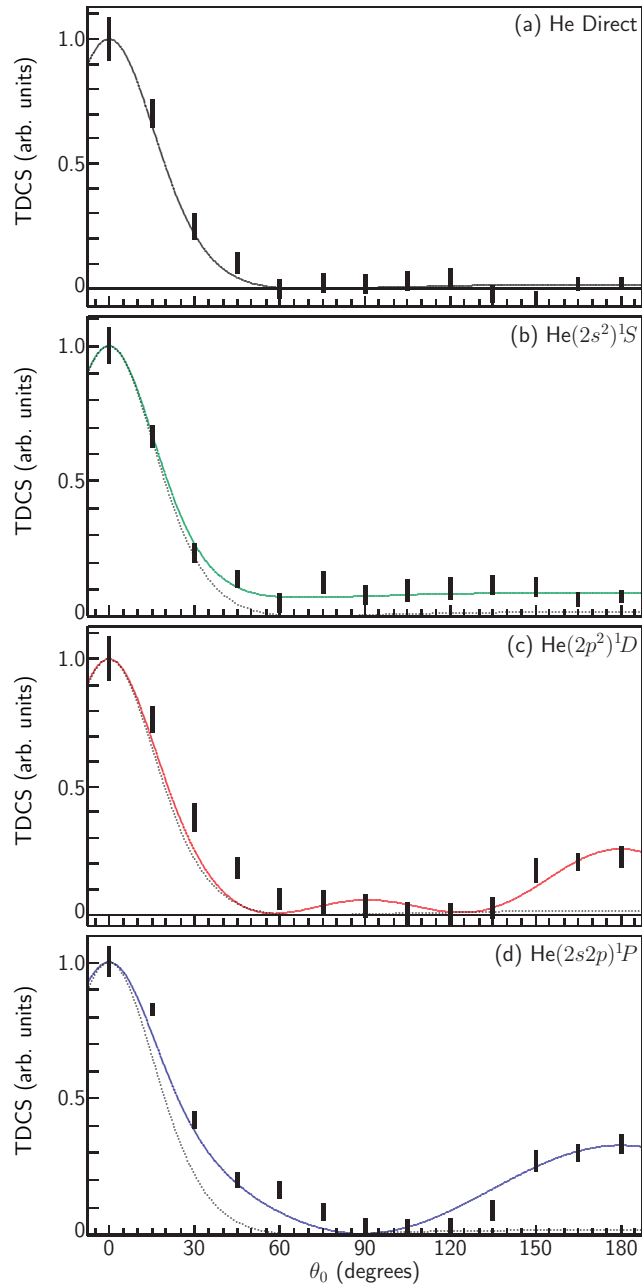


Figure 7.3: He out-of-plane ($e, 2e$) ejected electron angular distributions for 488 eV electrons scattered through 20.5° . Vertical bars are experimental results and include both statistical and systematic errors. (a) Direct ionization with 34.1 eV ejected electrons. (b)–(d) Autoionization via $(2s^2)^1S$, $(2p^2)^1D$, $(2s2p)^1P$. Solid and dotted lines are the PWBA calculations described in the text.

resonance should be described by $P_1^2(\theta_0)$. Figure 7.3(b) shows the angular distribution for the 1S level; the data are non-zero for the entire angular range and our calculations are consistent with the data. Specifically, the data for the portion of the angular distribution within the recoil lobe are described well by $P_0^2(\theta_0)$ (which is a constant). Data for the 1D level are shown in figure 7.3(c). Agreement between our theoretical calculations and the data is not as good here as it was for direct ionization and the 1S resonance. However, there is a distinctly different (compared to the 1S level) “signature” in the recoil lobe and it is suggestive of $P_2^2(\theta_0)$. Similarly the data for the 1P resonance (shown in figure 7.3(d)) has a distinct “signature” which is suggestive of $P_1^2(\theta_0)$. Our calculations for this level have reasonable, but not great, agreement with the data.

It should be noted that our calculations indicate that the binary lobe for direct ionization, and the 1S and 1D resonances should have the same shape, while that for the 1P resonance should be somewhat fatter. Examination of the data suggests that this is true for the 1S and 1P resonances, but the 1D resonance is broader than expected. This may be the result of some overlap from the 1P level arising from the relatively poor energy resolution we are using for these experiments.

7.5 Conclusions

We have performed ($e, 2e$) measurements of ejected electron angular distributions, covering all 360° of a plane perpendicular to the scattering plane and containing the momentum transfer direction. These measurements were performed for the case of He direct ionization ($E_{ej} = 34.1$ eV) and for three autoionizing levels, used 488 eV incident energy electrons, and had a momentum transfer value of approximately 2.1. The presence of autoionization has a significant effect on the recoil lobe, with each autoionizing resonance presenting its own “signature”. We have found that the data is qualitatively described well using a PWBA calculation, but that quantitative agreement required values of q_L that disagree with previously (theoretically) determined values. As a final note, Klaus Bartschat has recently performed a set of first-order and second-order hybrid distorted-wave + convergent R -matrix with pseudo-states calculations that indicate that a second-order model is required to correctly reproduce the recoil lobe of our

out-of-plane measurements over autoionizing resonances [48].

Appendix A

The ejected electron spectrum of He below the $N = 2$ threshold

This appendix has been previously published as [53].

A.1 Introduction

The spectrum of helium from an excitation energy of 57 eV to the He^+ $N = 2$ threshold at 65.4 eV, contains many Rydberg series of autoionizing levels embedded in the He^+ $1sE\ell$ continuum. Only the five lowest levels $2s^2\ ^1S_0$, $2s2p\ ^3P$, $2p^2\ ^1D_2$, $2s2p\ ^1P_1$, and $2p^2\ ^1S_0$ may be described in a single configuration approximation. For the higher members of these series, and all members of other series, the strong electron-electron correlation effects present in He preclude a single configuration description and the $(sp, 2n\pm)$ scheme (originally called the $(2n\pm)$ scheme [55]) may be used for the optically allowed series while the ${}_N(K, T)_n^A$ classification scheme [56] (also written as ${}_n(K, T)_N^A$ [57, 58, 59]) may be used for both optically allowed and optically forbidden series. The quantities K, T correspond to angular, and A radial, correlations of the two electrons in a hyperspherical coordinate description of He. A discussion of these schemes is given in Ref. [59], for example.

Since the *number* of basis states is the same in any classification scheme, it is possible to use the familiar single configuration basis to predict the number of $(sp, 2n\pm)$ or ${}_N(K, T)_n^A$ Rydberg series for a given L, S . Thus, for example, the number of $^1D^e$ series which contain $n = 2$ is one, corresponding to the configuration $2p^2$. For $n = 3$ there are two series corresponding to the basis configurations $2p3p, 2s3d$, and for $n \geq 4$ there are three series corresponding to a $2pnp, 2snd, 2pnf$ basis. (Note that correlation effects do not affect the validity of the LS coupling scheme used, but that at very high n , spin orbit effects become significant [60].) Figure A.1 gives the positions (up to $n = 6$ or 7) of all sixteen series for $L \leq 2$; the $n = 2$ positions are experimental [52] and the remainder are calculated values [56].

The most prominent of the dipole allowed series, $(sp, 2n+)$, was first seen in the pioneering synchrotron experiments of Madden and Codling [61]. Since then all three dipole allowed series have been extensively studied up to high n with high resolution absorption experiments using synchrotron radiation [62, 51], and the $(sp, 2n\pm)$ series

have also been observed in high resolution photoelectron experiments [63]. Recently, the $2p^2\ ^1D_2$ *quadrupole* level has been observed in a photoelectron experiment via dipole-quadrupole interference effects [64]. Other synchrotron experiments have investigated the effect of applied electric fields on the spectrum of He below the $N = 2$ threshold [65, 66] and Stark mixing has been used to observe optically forbidden even parity $^1P^e$ levels in photon induced fluorescence spectra [67].

The four lowest $n = 2$ levels, $2s^2\ ^1S_0$, $2s2p\ ^3P_1$, $2p^2\ ^1D_2$, and $2s2p\ ^1P_1$, have been extensively studied in a variety of charged particle impact experiments using electron, proton, and ion projectiles. The electron impact experiments fall into three main categories: energy loss [68, 69], ejected electron [70, 71] and $(e, 2e)$ [72, 73, 74, 21], where – in addition to the singlet levels – the triplet level may be seen at low incident energy. Energy loss spectra also contain non-autoionizing levels such as $2p^2\ ^3P$ [75]. Post collision interaction (PCI) effects for incident electron energies less than 10 eV above threshold cause line shape distortion and a shifted resonance energy [76, 77]. Such PCI effects can also be very important in ion [78, 79] and proton [80] impact experiments.

There is less experimental data on the $n > 2$ optically forbidden levels. In an ion-atom collision experiment a survey spectrum for $\text{Li}^+ + \text{He}$ showed some $n = 3$ levels, but the resolution was insufficient to resolve them [79]. Levels up to $n = 5$ (resolved up to $n = 4$) have been identified in an experiment that created autoionizing levels by double electron capture of low-energy He^{2+} ions colliding with Ba atoms [81], and the energies of some levels up to $n = 5$ have been extracted from VUV photoemission studies [82]. Because of the nature of these two experiments there was no line profile information and the intensity variation with increasing n of well behaved Rydberg series, associated with charged particle impact spectra, was not present. In addition, the data of [81] included PCI effects which precludes the extraction of accurate level energies.

There is one detailed electron impact study which includes the $n > 2$ optically forbidden levels [70]. Levels up to $n = 5$ are tabulated, but only levels up to $n = 3$ were resolved. Because of the low count rates associated with the small helium cross section, the statistics of these experiments were relatively poor. In the present work, our apparatus incorporates a position sensitive detector (PSD) which results in an effective count rate more than an order of magnitude higher than those obtained in earlier exper-

iments. Thus the experiments presented in this paper represent an advance over those of Ref. [70] because the improved statistics of our spectra, taken with a PSD, enable weak features, not seen in their work, to be observed, and also enable the resolution of closely spaced features. The good statistics of our data allow us to fit line profiles to obtain accurate profile parameters and enable the accurate manipulation of two spectra taken at different ejected electron directions.

In section II we give details of the experimental method, in section III we present and discuss the experimental results, and section IV contains the summary and conclusions.

A.2 Experimental method

The present He ejected electron experiments use part of an $(e, 2e)$ apparatus which has been described in detail elsewhere [20]. An unmonochromated electron gun intersects a gas beam that effuses through a 1 mm diameter aperture approximately 2 mm below the interaction region. The ejected electron detector, which uses a hemispherical-sector electrostatic type analyzer terminated in a position sensitive detector, is mounted on a turntable. During an experiment energies are scanned repetitively to minimize the effect of any drift in, for example, the electron beam intensity. Each scan took approximately one hour and consisted of stepping through 1250 points in 7.5 meV increments. Each spectrum presented in this paper took between one and four days to acquire.

The energy resolution of the present He spectra is just under 50 meV, somewhat larger than the 40 meV obtained in heavier targets [20]. We believe that the inferior resolution in helium is due, at least in part, to Doppler broadening. Although the helium beam emerges from a thin tube of length 10 mm and diameter 1 mm, and is therefore fairly well collimated, there is a substantial background He pressure of $\sim 10^{-5}$ Torr. (Experiments are carried out at the maximum possible beam intensity in order to maximize the count rates from small e-He cross sections.) For an electron ejected with energy E_{ej} from an atom in thermal equilibrium at temperature T the Doppler effect contributes a width [83]

$$W = \sqrt{11.1\gamma_M k T E_{ej}}, \quad (\text{A.1})$$

where γ_M is the ratio of the electron to the atomic mass and k is Boltzmann's constant. The autoionizing region of He is particularly affected because of the small atomic mass

and the large ejected electron energies of ~ 35 eV. For helium at 300 K and an ejected electron energy of 35 eV we find $W = 37$ meV. If this is added (in quadrature) to our nominal resolution of 40 meV we obtain an upper limit for the effective resolution of 54 meV.

In section III we present the results of fitting generalized line profiles to the spectra. It has been shown that, in the absence of PCI effects and provided none of the resonances overlap, an ejected electron spectrum, observed at angles θ and ϕ , due to charged particle impact will take the form [84]

$$I(E, \theta, \phi) = \sum_{\mu} \frac{\alpha_{\mu}\eta_{\mu} + \beta_{\mu}}{1 + \eta_{\mu}^2} + \gamma, \quad (\text{A.2})$$

where the sum is over the autoionizing levels labelled by μ , and the ejected electron energy E enters via the definition $\eta_{\mu} = 2(E - E_{\mu})/\Gamma_{\mu}$, which is the energy, in halfwidths ($\Gamma_{\mu}/2$), away from the μ^{th} resonance position E_{μ} [17]. The parameters $\alpha_{\mu}(\theta, \phi)$ and $\beta_{\mu}(\theta, \phi)$ depend on the collision dynamics and describe a resonance line profile. The parameter $\gamma(E, \theta, \phi)$ describes the direct ionization background and is a slowly varying function of E . We found that the empirical function

$$\gamma = \gamma' + \frac{\gamma''}{E}, \quad (\text{A.3})$$

where γ', γ'' are constants for a given spectrum, gave an excellent fit to all the data. When fitting Eq. (A.2) to our spectra it is necessary to fold in the instrument function. We found that it was not possible to fit both the $n = 2$ and $n = 3$ regions of a spectrum with a Gaussian type instrument function: the required width for $n = 2$ was too large for the $n = 3$ region. In fact we found that a fixed Voigt profile of 48.5 meV full width at half maximum (FWHM), formed by folding a Gaussian of FWHM 46.5 meV with a Lorentzian of FWHM 6.5 meV, gave a good fit to all regions of all the spectra presented in this paper. (It is possible that the Doppler broadening is in some way responsible for this instrument function; in previous experiments on Xe [20] a pure Gaussian was adequate to explain the experimental results.)

A.3 Results and discussion

In principle it is not usually possible to unambiguously assign a feature in an ejected electron spectrum to a particular final ion state; however, He is a special case because

the maximum possible ejected electron energy, for a transition leaving the ion in a state $N > 1$, is one Rydberg (≈ 13.6 eV), which is the difference between the double ionization potential (79.0 eV) and the $N = 2$ threshold (65.4 eV). Thus for the ejected electron spectra below, which begin at 32 eV, the final ion state is $N = 1$. To convert ejected electron energies to level positions we have used a first ionization potential of 24.587 eV.

Below we discuss spectra taken at the three incident electron beam energies 550 eV, 150 eV, and 75 eV, for the three ejected electron directions 60° , 90° , and 120° at each energy. There are some general rules that apply to the spectra: (1) 120° seems to be the best angle for seeing non-dipole levels at all incident energies. Presumably this is because interference effects between these levels and opposite parity continua enhance the line shapes relative to those in the 90° spectra. (In contrast the same effects, with opposite sign, suppress these levels in 60° spectra.) (2) 550 eV spectra show singlets (not triplets that require exchange excitation) of both dipole and non-dipole levels. The 150 eV spectra show singlet levels for all n , and show the $n = 2$ triplet as a weak feature. In the 150 eV spectra, non-dipole singlet levels are enhanced (relative to dipole) when compared with the 550 eV spectra. Therefore the 150 eV spectra are useful for observing and assigning non-dipole singlet levels. (3) The 75 eV spectra show both singlet and triplet non-dipole levels; comparison with the 150 eV spectra enables the triplet levels to be assigned.

Figure A.2 (a) shows the He photoabsorption spectrum below the $N = 2$ threshold, taken from Ref. [62], in which the optically allowed $(sp, 2n\pm)$ 1P levels are labeled. Figure A.2 (b) shows our survey spectrum for 550 eV incident energy and an ejected electron direction of 90° with respect to the incident beam direction. Three prominent Rydberg series are present whose lowest members are the well known $2s^2$ 1S_0 , $2p^2$ 1D_2 , and $2s2p$ 1P_1 autoionizing levels. For the higher members of each series the $(sp, 2n\pm)$ scheme is used for the optically allowed series while the ${}_N(K, T)_n^A$ classification scheme is used for most of the optically forbidden series. With our resolution the unresolved Rydberg series appear up to $n = 7$; the 1S_0 levels may be resolved from the other two up to $n = 5$. The level positions indicated for the three series are from Brink *et al.* [52] for $n = 2$ and are the theoretical values of Chen [56] for $n > 2$. As can be seen, at high incident electron energy and for this ejected electron direction the optically allowed

1P levels closely mimic the asymmetric profiles of their photoionization counterparts in panel (a); the reason for this is discussed below. Also present in panel (b) of the figure are two other features: the $2p^2\ ^1S_0$ level at about 37.5 eV, and the very weak $(sp, 23-)\ ^1P_1$ level; this is the first time that the latter has been seen in an electron impact experiment.

The $(sp, 23-)\ ^1P_1$ level may be seen more clearly in Fig. A.3 which shows a high quality, background subtracted spectrum of the $n = 3$ region for an incident energy of 550 eV and an ejected electron direction of 120° . In the electron impact spectrum the $(sp, 23-)\ ^1P_1$ level is about 22 times weaker than the $(sp, 23+)\ ^1P_1$ level, in qualitative agreement with the photoabsorption ratio of about 1/30.

Figure A.4(a) shows a survey ejected electron spectrum for 550 eV incident energy and an ejected electron direction of 120° . The line profiles for the 1S_0 and 1D_2 levels are dramatically different from those for 90° . As in Fig. A.2 the line profiles of the lowest members of each series are repeated for the higher members of the series. This is to be expected for a well behaved Rydberg series of autoionizing levels, where both the widths and the excitation probabilities scale in the same way with principal quantum number. The left half of figure A.4(b) shows the results of a least squares fit of Eq. (A.2) to the three $n = 2$ levels. The resulting three sets of line profile parameters α_μ, β_μ , and the common parameter $\gamma(E)$, together with Chen's calculated values [56] of the positions and widths of all levels, were then used to synthesize the spectrum in the right half of the figure. Figure A.4(c) shows (b) superimposed on (a). The shape of the $n \geq 3$ series is correctly given by the synthesized spectrum but the magnitude is too large. Note that the apparent change in the ratio of the $^1D/^1P$ intensity with increasing n is in fact due to the finite experimental resolution – the n^1P levels are narrower than the n^1D levels and hence their height appears to decrease more rapidly with increasing n ; with perfect resolution a well behaved Rydberg series has an n -independent peak intensity. This region is shown in more detail in Fig. A.5 with the synthesized spectrum of Fig. A.4(b) given by the broken curve. The solid curve is given by the same procedure as in Fig. A.4, but using a fit to the $n = 3$ levels. The agreement of the synthesized $n \geq 4$ spectrum with the experimental spectrum is very good, from which it may be deduced that the electron impact excitation matrix elements for $n \geq 3$ scale approximately as expected

for well behaved Rydberg series.

Figure A.6 shows a survey ejected electron spectrum for 550 eV incident energy and an ejected electron direction of 60° . The line profiles are very different from both the 90° and 120° spectra in Figs. A.2 & A.4, respectively. Almost all non-dipole levels for 60° have a mainly “window” resonance character – a notable exception is $2p^2\ ^1S_0$ at 37.5 eV (the lowest member of the $2(-1, 0)_n^+ \ ^1S$ series) which is enhanced relative to its appearance in the other two spectra.

As stated above, we ascribe the differences between the lineshapes in the three spectra to interference effects between autoionizing levels and opposite parity continua which change sign for ejected electrons 180° apart. A detailed discussion of such interference effects is given in Ref. [85] in the context of Xe ejected electron spectra, and in Ref. [21] for He ($e, 2e$) spectra. For the Xe spectra we found that the summation of spectra for ejected electron directions 50° and 130° removed the interference terms and resulted in a spectrum almost identical to the 90° spectrum; clearly it is of interest to see if the same is true of He. In order to do this, the $n = 2$ portions of the 120° and 60° data in Figs. A.4 & A.6 were fitted to Eq. (A.2) and the summed spectrum created by adding the two sets of α, β, γ . This procedure was necessary in order to align the energy scales of the spectra as accurately as possible; it was found that even a small misalignment profoundly affected the summed spectrum. The summed spectrum is shown in Figure A.7. As can be seen it is very similar to the 90° data; in particular the asymmetry of the 1P level is almost identical in the summed and 90° spectra. Note that for the line profiles to be n independent requires that the interference effects which lead to the highly angular dependent spectral shapes must scale the same way with energy (i.e., n) which in turn implies that the electron impact direct ionization matrix elements for all multipoles scale the same way with energy.

Figure A.8 shows the mainly $n \geq 3$ portion of a spectrum for 150 eV incident energy and 120° ejected electron direction. Three weak features are indicated by vertical dotted lines. The first of these is the $(sp, 23-)\ ^1P_1$ level with an intensity relative to $(sp, 23+)\ ^1P_1$ similar to that seen at 550 eV incident energy. The second is the $2(1, 0)_3^+ \ ^3P$ level; this lies close to the $2(1, 0)_3^- \ ^3D$ level, but the latter is expected to be absent at this incident energy. The third is a previously unseen quadrupole level, the

first ($n = 3$) member of the ${}_2(0,1)_n^0 \ ^1D$ series.

Figure A.9 is a survey spectrum for 75 eV incident energy and ejected electron direction of 60° . As stated in the introduction of this section, for this direction destructive interference suppresses many series; an exception is the ${}_2(1,0)_n^+ \ ^3P$ series which stands proud of the adjacent ${}_2(1,0)_n^+ \ ^1S$ series, and hence may be resolved up to $n = 5$, as indicated in the figure. At this incident energy the main $L = 1$ triplet and singlet series, ${}_2(1,0)_n^+ \ ^3P$ and $(sp, 2n+) \ ^1P_1$, are of comparable intensity; i.e., exchange processes are of equal importance to direct processes. Figure A.10 shows the (mainly) $n = 3$ region for 120° where four weak features of similar intensity are identified. The first and third are the lowest members ($n = 3$) of the previously unobserved ${}_2(1,0)_n^- \ ^3S$ and ${}_2(0,1)_n^- \ ^3P$ series. The second is the $(sp, 23-) \ ^1P_1$ level seen in the spectra for all incident energies. The fourth feature peaks at an energy that corresponds almost exactly with the calculated ${}_2(-1,0)_3^+ \ ^1S$ (i.e., $2p3p \ ^1S$) level. This feature appears in a number of other spectra and in all cases its lineshape closely mimics that of the well resolved $2p^2 \ ^1S$ level whose asymmetry is a strong function of incident electron energy and ejected electron emission angle. We therefore deduce that the levels that are calculated to lie on either side of the $2p3p \ ^1S$ level (see figure) do not contribute significantly to this feature.

A series of least squares fits to the generalized line profile Eq. (A.2) were carried out to obtain the positions and (where possible) the widths of the levels in the spectra. Table A.1 lists all the levels that have been observed in this work; for easy reference the first column assigns them a label $\mu = 1 \rightarrow 30$. Our energy scale was aligned using level $\mu = 8$, $(sp, 23+) \ ^1P$, which was fixed at the photoionization value [59]. (This level was chosen, rather than the more intense level $\mu = 4$, $2s2p \ ^1P$, in order to obviate the possibility of inaccuracies due to PCI effects; these are proportional to the natural width of a level [77] and for $n = 2$ the 1P width is 37 meV whereas for $n = 3$ the width is only 8 meV.) Relative energies were then determined from the increase of energy of 7.5 meV between points set by an in-house computer-controlled digital to analogue converter (DAC).

The energies and widths given in Table A.1 are the average values from fits to all of the nine spectra (the combinations of $E_0 = 550, 150, 75$ eV and $\theta_{EJ} = 60^\circ, 90^\circ, 120^\circ$) in which a level could be seen. Since the positions given are those found from fits

to the generalized line profile, they are resonance positions rather than peak positions; exceptions are listed below. The uncertainties given are the standard deviations among the fits except that there is a minimum uncertainty of 8 meV in our absolute energy scale. Widths not given in the table were too narrow to fit and were fixed at theoretical values [56] in the fits.

The upper part of the table consists of the four Rydberg series whose lowest members ($\mu = 1 \rightarrow 4$) are the four lowest energy $2\ell 2\ell'$ levels. It was found that if all α_μ, β_μ in Eq. (A.2) were independently fitted parameters, the fits were rather ambiguous because very small changes in χ^2 were accompanied by large changes in all fitted parameters for $n = 4, 5$. We attribute this to the fact that these levels are not well resolved. The discussion above relating to Fig. A.4 suggested a way around this problem and satisfactory fits with reduced $\chi^2 < 2$ were obtained by fixing α_μ, β_μ values for $n = 4, 5$ ($\mu = 9 \rightarrow 16$) at the values fitted for the corresponding well resolved $n = 3$ levels ($\mu = 5 \rightarrow 8$). For $n = 6$ there were two groups of two unresolved levels ($\mu = 17, 18$ and $\mu = 19, 20$); the peak positions of these features are given in the table. For $n = 7$ the four levels ($\mu = 21 \rightarrow 24$) appeared as a single unresolved feature whose peak position is given in the table.

The lower part of the table consists of other levels seen in this work which have been discussed in Figs. A.8 & A.10. The widths of very narrow levels were fitted with large uncertainties. Thus, for example, level $\mu = 25$ yields a width 0.007(7) eV which essentially provides an upper limit of 0.014 eV.

The theoretical levels and widths in the table are compiled from Refs.[56, 86, 87, 88, 89, 90, 91, 92, 93, 94, 95, 96]. The values are given as the central value of all the calculations, with an “uncertainty” corresponding to the range of the calculations. Thus, for example, 57.833(8) eV means that the minimum calculated value is 57.825 eV, and the maximum value is 57.841 eV; all other calculations lie between these values. Where necessary, values have been converted using an atomic unit of energy 2×13.60383 eV and a double ionization potential of 79.003 eV [59]. It can be seen that, with the exception of the two lowest $2pnp \ ^1D$ levels, the spread of the theoretical values is less than our experimental uncertainties; overall, there is excellent agreement between theory and experiment.

Also shown in the table are experimental levels taken from other workers. Our values for $(sp, 2n+)$ 1P ($n = 2, 4, 5$) are in excellent agreement with the photoionization values [59] which confirms the linearity and accuracy of our energy scale. Our electron impact results represent an increase in precision over the early electron impact data of Hicks and Comer [70]. The data of Iemura *et al* [81] include PCI shifts and we have used their estimated shifts as uncertainties in the level positions; there is then good agreement with our values.

Lastly, all the spectra contained a sharp reduction in intensity at, or close to, the $N = 2$ threshold. This is due to the end of the quasi-continuum formed by the $n \approx 8 \rightarrow \infty$ unresolved members of $2\ell n\ell'$ Rydberg series. We fitted this region of the spectrum by modifying Eq. (A.3) to include a step whose position and magnitude (folded with our energy instrument function) were two extra fitted parameters. Fig. A.11 (solid line) shows an example of such a fit. Similar fits were carried out for other spectra and gave an average value of 65.377(20) eV for the ionization threshold, just over one standard deviation less than the accepted value of 65.402 eV [59]. It is possible that this disagreement is caused by significant (10%) radiative damping effects that are predicted in the near threshold ionization yield [60]; i.e., fluorescence of the doubly excited levels becomes about 10% as important as autoionization and causes a corresponding decrease in intensity which, when folded with our instrument function, may lead to a fitted step at an energy slightly below the true threshold.

A.4 Summary and conclusions

We have obtained high quality electron impact ejected electron spectra over a wide range of incident energies and ejected electron directions. The four prominent autoionizing Rydberg series, 1S , 3P , 1D , 1P , have been tabulated up to $n = 5$ and observed, but not resolved, up to $n = 7$. It has been verified that for $n \geq 3$ the profile parameters are approximately n -independent. The very weak optically allowed $(sp, 23-)$ 1P level and the optically forbidden $(sp, 23-)$ 3P have been observed for the first time in an electron impact experiment. Also, three optically forbidden levels have been seen for the first time. The overall conclusion of this work is that theory does a good job of calculating the positions and widths of all levels we have observed; in all cases there is

no discrepancy within our experimental uncertainty.

ACKNOWLEDGMENTS

The authors wish to thank Dr. Peter van der Burgt for sharing his extensive compilation of data on, and references to, He energy levels, and Dr. Thomas Gorczyca for helpful discussions on near threshold damping effects. This work was supported by the United States National Science Foundation under grant PHY-9987861.

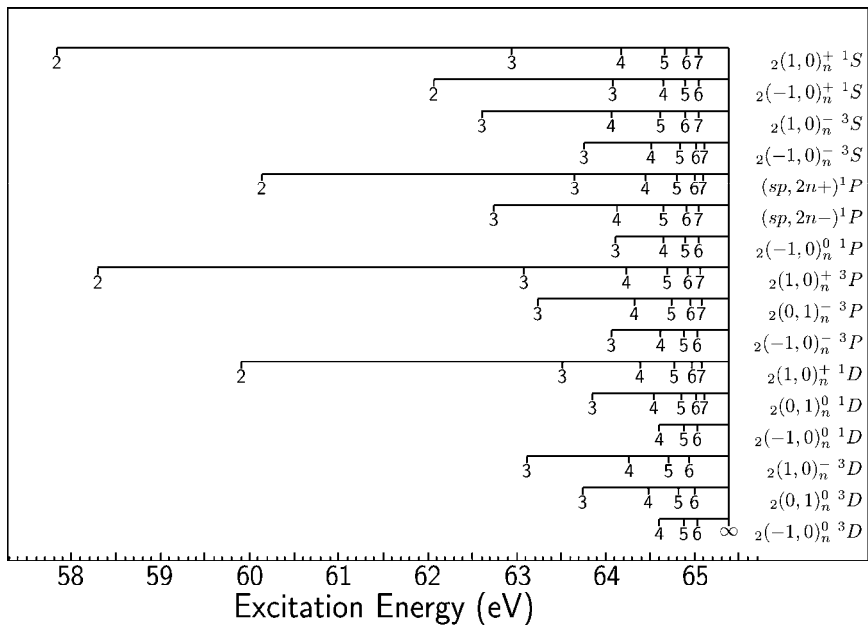


Figure A.1: Level positions above the helium ground state of the sixteen He doubly excited series with $L \leq 2$ that lie below the $N = 2$ threshold.

Table A.1: He autoionizing levels below the N=2 threshold seen in the present work. Theoretical values are a compilation of Refs.[56, 86, 87, 88, 89, 90, 91, 92, 93, 94, 95, 96] (see text). The remaining columns in the table are other workers' experimental values [59, 64, 70, 81, 82]. The numbers in parenthesis are the uncertainties in the last digits: 0.138(15) means 0.138 ± 0.015 . Level energies used for calibration are in parenthesis.

μ	State	Config- Term	This work		Theory		^a Ref.[70], ^b Ref.[82]		^c Ref [64], ^d Ref [59]	Ref.[81]
		uration	E (eV)	Γ (eV)	E (eV)	Γ (eV)	E (eV)	Γ (eV)	E (eV)	E (eV)
<i>n=2</i>										
1	$2(1,0)_2^+$	$1S^e 2s^2$	57.839(12)	0.120(14)	57.833(8)	0.1076(170)	57.82(4) ^a	0.138(15)		57.84(15)
2	$2(1,0)_2^+$	$3P^o 2s2p$	58.302(8)	0.005(11)	58.312(1)	0.0082(0)	58.30(3) ^a	<0.015		58.31(3)
3	$2(1,0)_2^+$	$1D^e 2p^2$	59.903(8)	0.052(21)	59.950(45)	0.0676(34)	59.89(3) ^a	0.072(18)	59.905(5) ^c	59.85(9)
4	$2(1,0)_2^+$	$1P^o 2s2p$	60.144(8)	0.037(7)	60.149(5)	0.0368(6)	(60.130) ^a	0.042(18)	60.147(4) ^d	60.09(6)
<i>n=3</i>										
5	$2(1,0)_3^+$	$1S^e 2s3s$	62.956(8)	0.033(10)	62.953(1)	0.0314(62)	62.94(3) ^a	0.041(10)		62.97(6)
6	$2(1,0)_3^+$	$3P^o sp,23+$	63.095(12)	0.003(2)	63.096(0)	0.0022(1)	63.07(3) ^a			63.11(2)
7	$2(1,0)_3^+$	$1D^e 2p3p$	63.515(9)	0.012(8)	63.529(13)	0.0161(10)	63.50(3) ^a			63.51(4)
8	$2(1,0)_3^+$	$1P^o sp,23+$	(63.658)	0.007(5)	63.657(1)	0.0083(1)	63.65(3) ^a		63.658(4) ^d	0.010(1)
<i>n=4</i>										
9	$2(1,0)_4^+$	$1S^e 2s4s$	64.184(8)	0.013(8)	64.178(0)	0.0123(13)	64.18(3) ^a			
10	$2(1,0)_4^+$	$3P^o sp,24+$	64.229(8)		64.234(0)	0.0008(0)	64.23(3) ^a			
11	$2(1,0)_4^+$	$1D^e 2p4p$	64.400(8)		64.408(8)	0.0068(5)	64.39(3) ^a			64.44(2)
12	$2(1,0)_4^+$	$1P^o sp,24+$	64.469(8)		64.465(1)	0.0034(1)	64.45(3) ^a		64.467(4) ^d	0.0040(5)
<i>n=5</i>										
13	$2(1,0)_5^+$	$1S^e 2s5s$	64.682(8)		64.673(2)	0.0058(5)	64.67(4) ^a			
14	$2(1,0)_5^+$	$3P^o sp,25+$	64.696(8)		64.700(0)	0.0004(0)	64.69(4) ^a			
15	$2(1,0)_5^+$	$1D^e 2p5p$	64.804(23)		64.789(9)	0.0034(2)				
16	$2(1,0)_5^+$	$1P^o sp,25+$	64.822(8)		64.814(0)	0.0018(0)			64.816(4) ^d	0.0020(3)
<i>n=6</i>										
17	$2(1,0)_6^+$	$1S^e 2s6s$			64.924(5)	0.0021(15)				
18	$2(1,0)_6^+$	$3P^o sp,26+$		64.924(12)	64.934(0)	0.0002(0)				
19	$2(1,0)_6^+$	$1D^e 2p6p$			64.988(9)	0.0021(3)				
20	$2(1,0)_6^+$	$1P^o sp,26+$		64.992(9)	64.999(0)	0.0010(0)				
<i>n=7</i>										
21	$2(1,0)_7^+$	$1S^e 2s7s$			65.059(1)	0.0019(0)				
22	$2(1,0)_7^+$	$3P^o sp,27+$			65.067(0)	<0.0001				
23	$2(1,0)_7^+$	$1D^e 2p7p$			65.096(1)	0.0012(0)				
24	$2(1,0)_7^+$	$1P^o sp,27+$		65.096(15)	65.108(1)	0.0006(0)				
25	$2(-1,0)_2^+$	$1S^e 2p^2$	62.093(12)	0.007(7)	62.097(24)	0.0117(59)	62.06(3) ^a			62.08(2)
26	$2(-1,0)_3^+$	$1S^e 2p3p$	64.088(16)		64.094(3)	0.0045(24)				
27	$2(1,0)_3^-$	$3S^e 2p3p$	62.603(13)		62.608(0)	0.0002(0)				
28	$2(1,0)_3^-$	$1P^o sp,23-$	62.748(10)		62.758(0)	0.0001(0)	62.759(2) ^b		62.758(4) ^d	0.0005(3)
29	$2(0,1)_3^-$	$3P^o sp,23-$	63.241(29)		63.249(0)	<0.0001	63.247(2) ^b			
30	$2(0,1)_3^0$	$1D^e 2s3d$	63.855(8)	0.008(8)	63.876(12)	0.0004(1)				

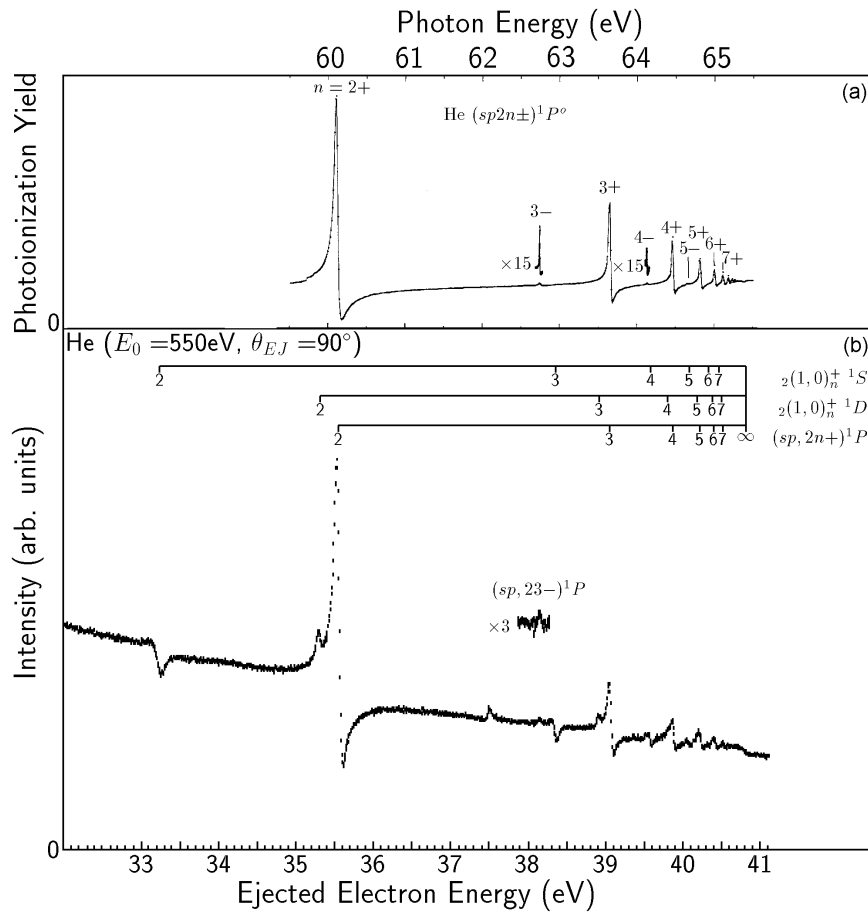


Figure A.2: (a) He photoabsorption spectrum from Ref.[62]. (b) Ejected electron spectrum taken at 90° with respect to a 550 eV incident electron beam.

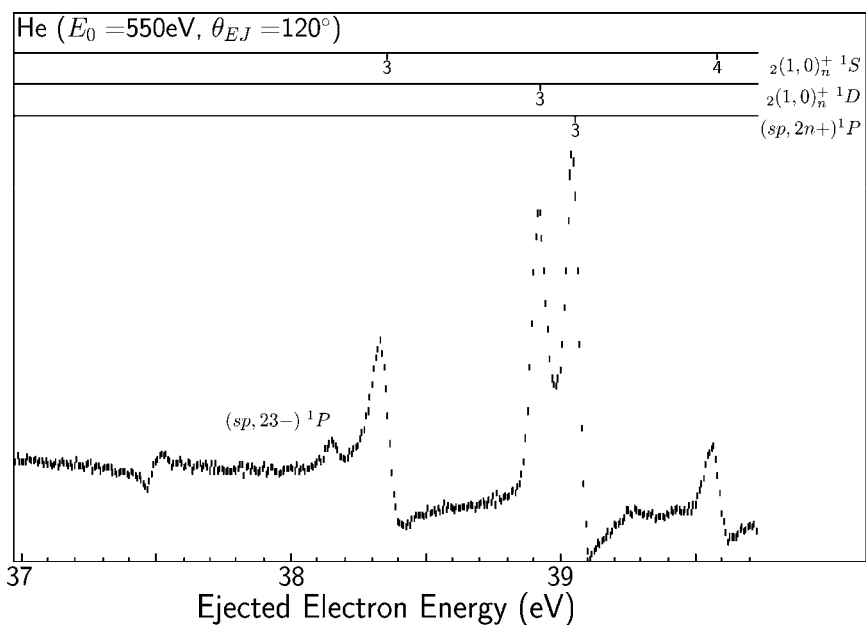


Figure A.3: The $n = 3$ region (background subtracted) of an ejected electron spectrum taken at 120° with respect to a 550 eV incident electron beam. The weak $(sp, 23-) 1P_1$ level is indicated.

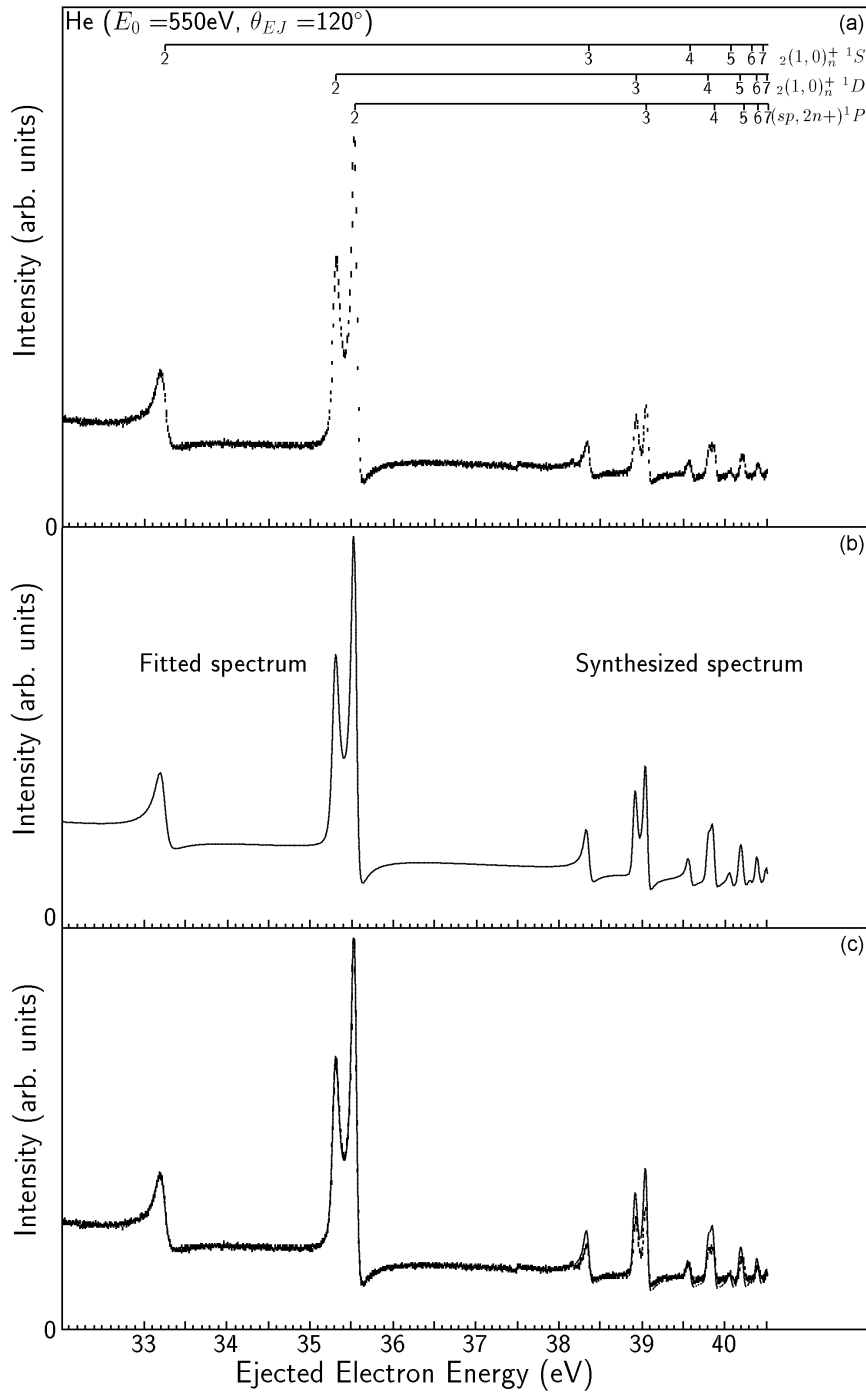


Figure A.4: (a) Ejected electron spectrum taken at 120° with respect to a 550 eV incident electron beam. (b) *Left half*: $n = 2$ spectrum reconstructed from fitting Eq. (A.2) to the three $n = 2$ levels. *Right half*: $n \geq 3$ spectrum synthesized from $n = 2$ parameters (see text). (c) shows (b) superimposed on (a).

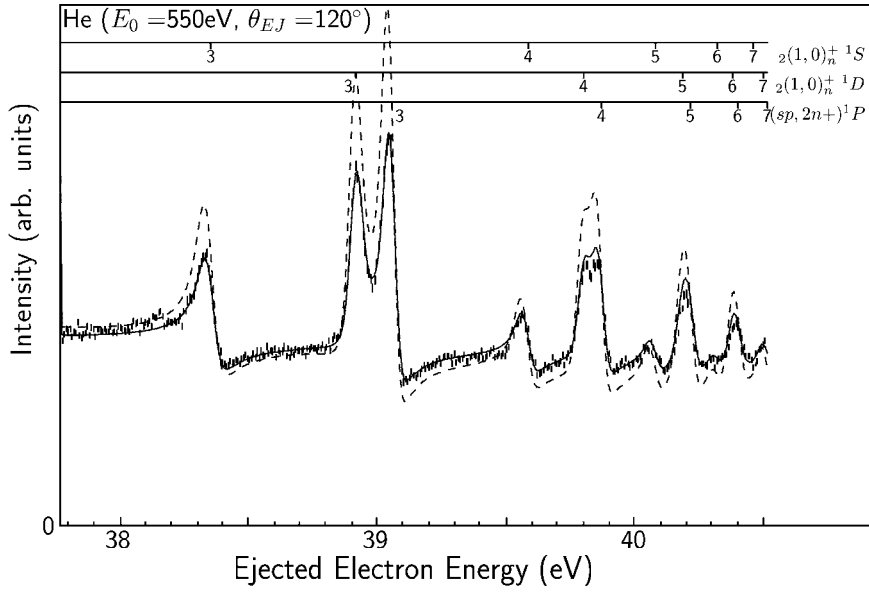


Figure A.5: Close up of right half of Fig. A.4. *Dashed line*: same as solid line in Fig. A.4 (b). *Solid line*: fitted $n = 3$ region and synthesized $n \geq 4$ region using $n = 3$ parameters (see text).

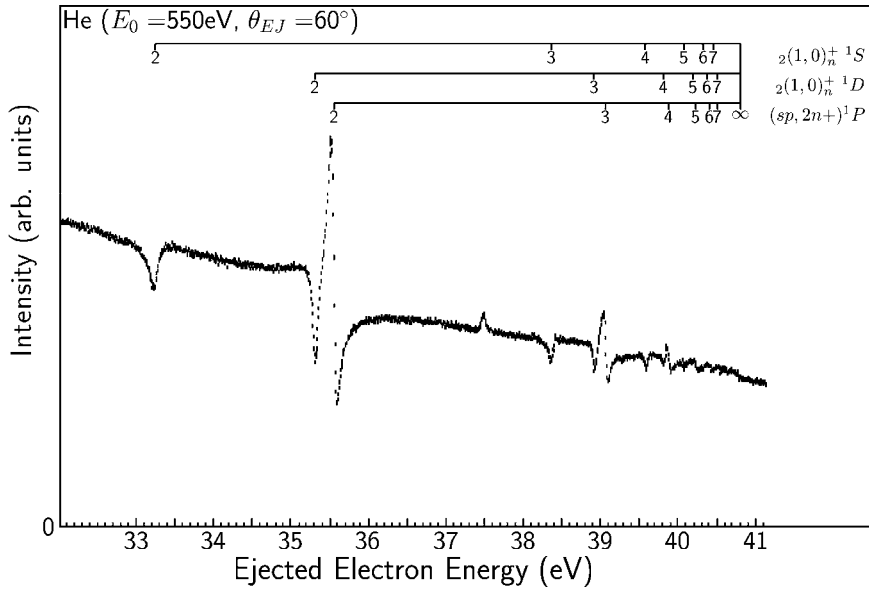


Figure A.6: Ejected electron spectrum taken at 60° with respect to a 550 eV incident electron beam. The feature at 37.5 eV is $2p^2 \ ^1S_0$.

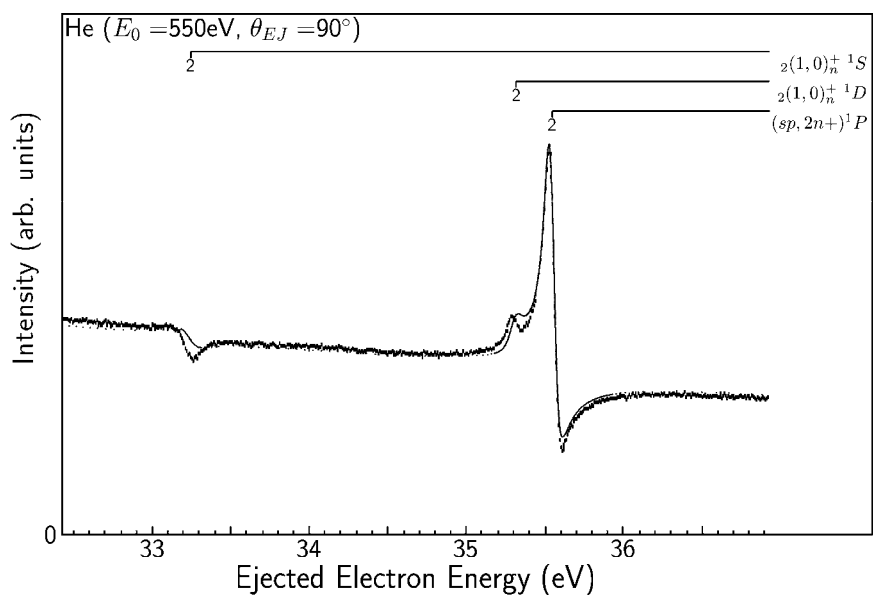


Figure A.7: $n = 2$ region of an ejected electron spectrum taken at 90° with respect to a 550 eV incident electron beam. *Solid line*: Sum of equivalent spectra for 60° and 120° (see text).

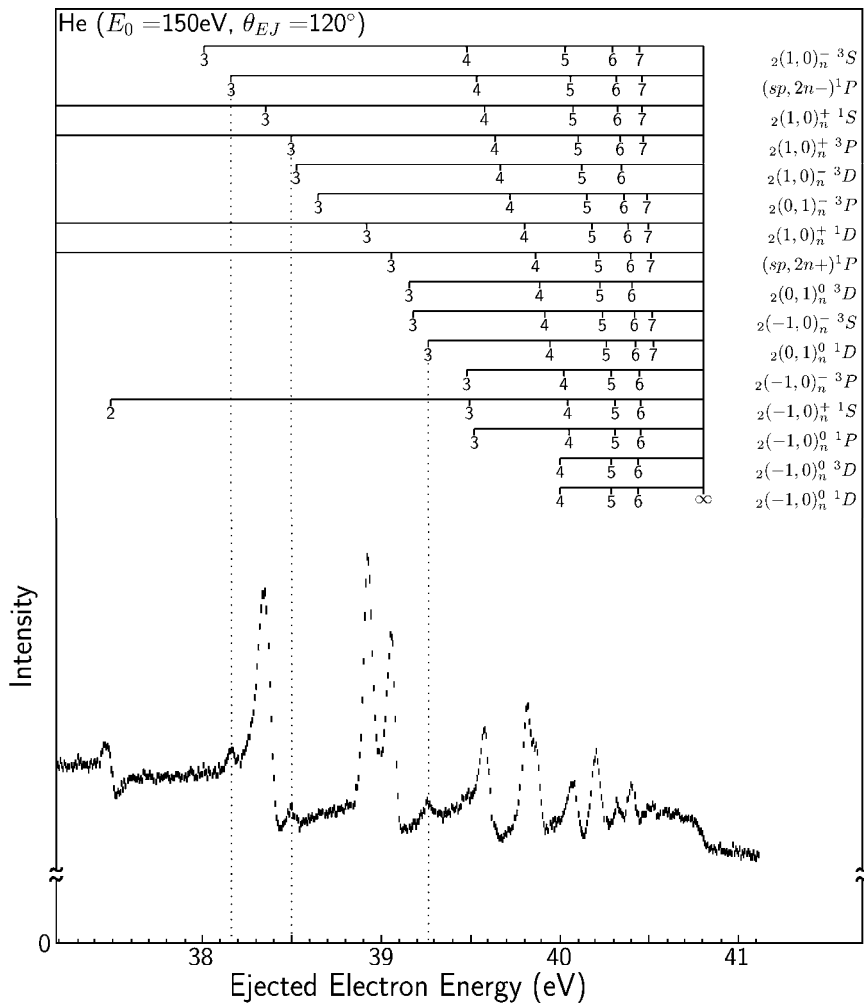


Figure A.8: $n \geq 3$ region of an ejected electron spectrum taken at 120° with respect to a 150 eV incident electron beam.

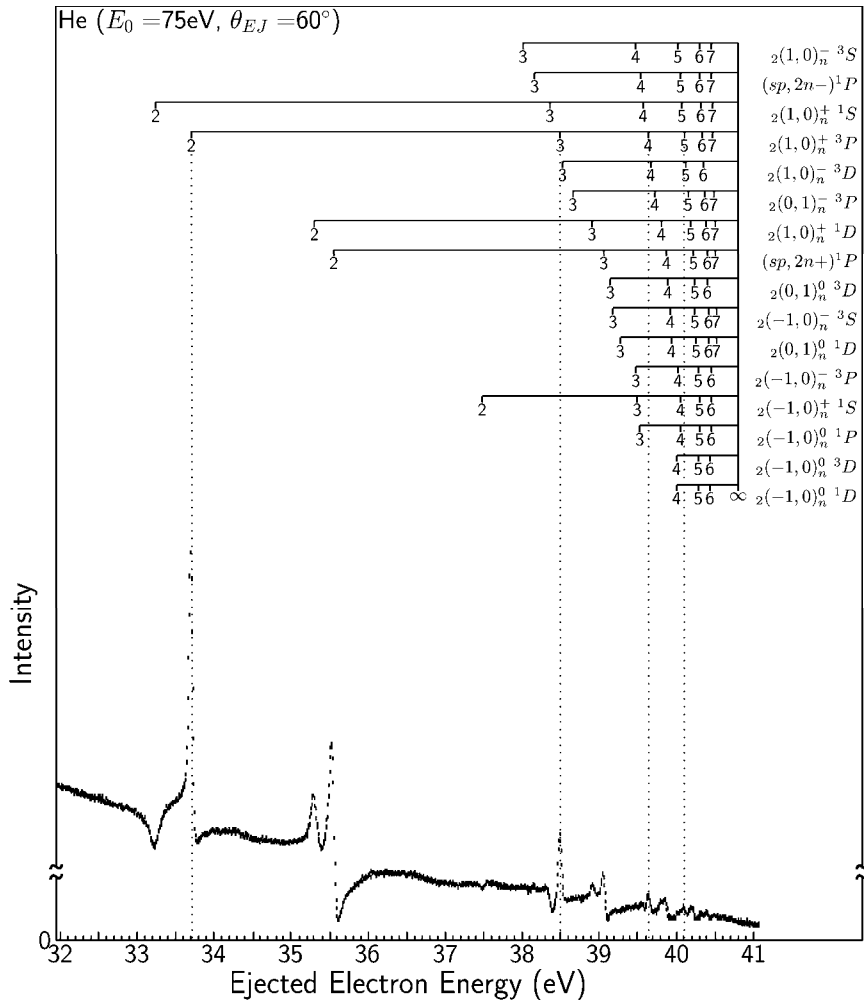


Figure A.9: Ejected electron spectrum taken at 60° with respect to a 75 eV incident electron beam. Note the prominent triplet levels indicated by the vertical dotted lines.

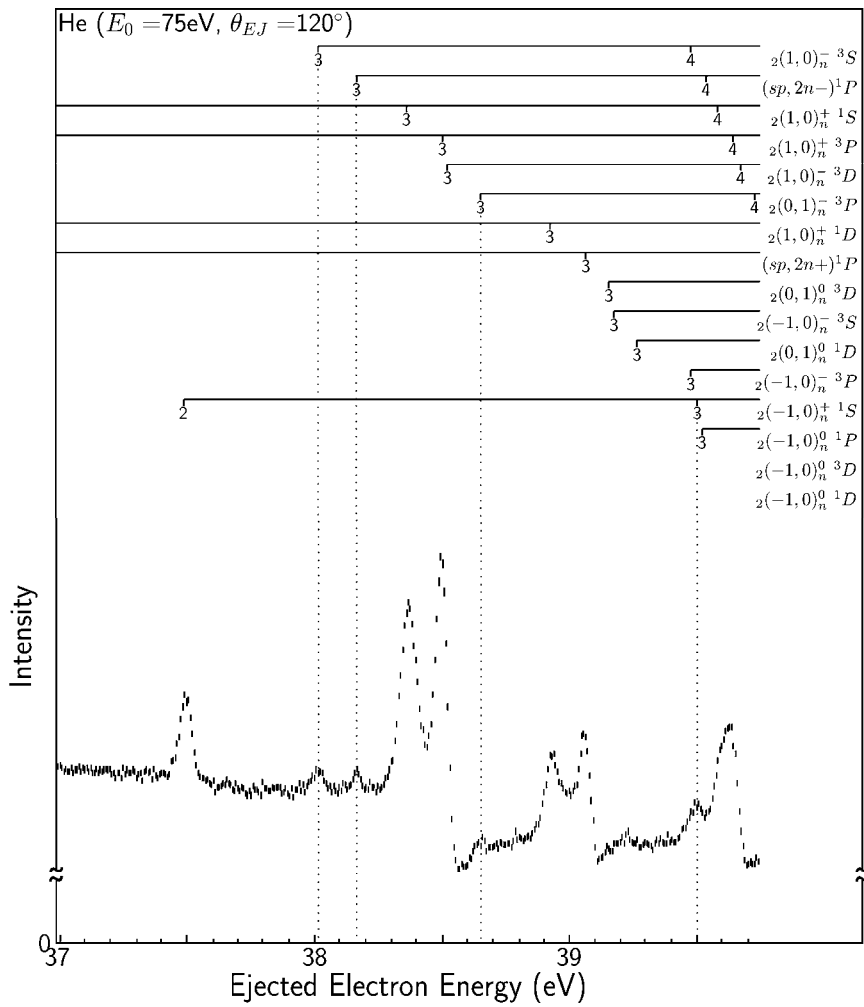


Figure A.10: $n = 3$ region of an ejected electron spectrum taken at 120° with respect to a 75 eV incident electron beam.

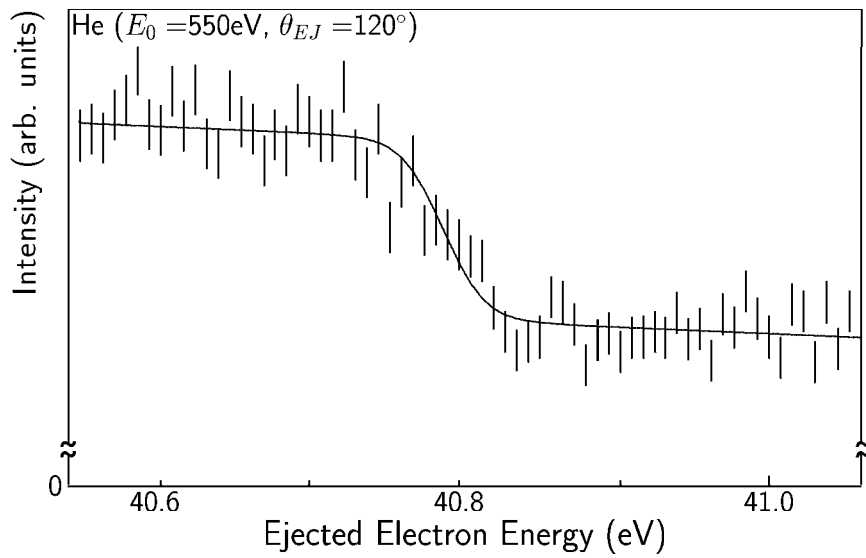


Figure A.11: Intensity step near the $N = 2$ threshold in an ejected electron spectrum taken at 120° with respect to a 550 eV incident electron beam. The solid line is a fit that includes a step function folded with the experimental energy resolution.

Appendix B

SIMION

B.1 SIMION Overview

SIMION is an electron and ion optics simulation program intended to provide methods for simulating a wide variety of general ion optics problems. Some of the general features of the software are:

- Windows compatibility.
- The ability to define electrode geometries either through the use of a graphical user interface or geometry files.
- An *ion optics workbench* that allows for virtual placement of up to 200 potential arrays in a simulated volume that is up to 8 km³.
- It allows for the visualization and recording of simulated ion/electron trajectories.
- There is a (limited) user program interface.

SIMION utilizes potential arrays to define electrostatic and magnetic fields. A potential array is a mesh of points filling a volume. Electrodes are defined by assigning some of these points a fixed potential. The potentials for points outside of the electrodes are then determined by solving the boundary value problem's Laplace equation via finite difference methods [97].

B.2 Purpose

Chapter 6 describes a set of four theoretical calculations that we compared to our experimental results. As mentioned in that chapter, a particular interest of our group is the taking of spectra with fixed ejected angles 180° apart. One can then manipulate the calculations and data to examine the sum and difference of spectra with ejected angles 180° apart, and the ratio of the difference to the sum of the two spectra. The main purpose of the work detailed in this appendix has been to obtain an instrument function that takes into account the finite size of the interaction region, which can then be folded with the theoretical calculations. By folding this instrument function with the

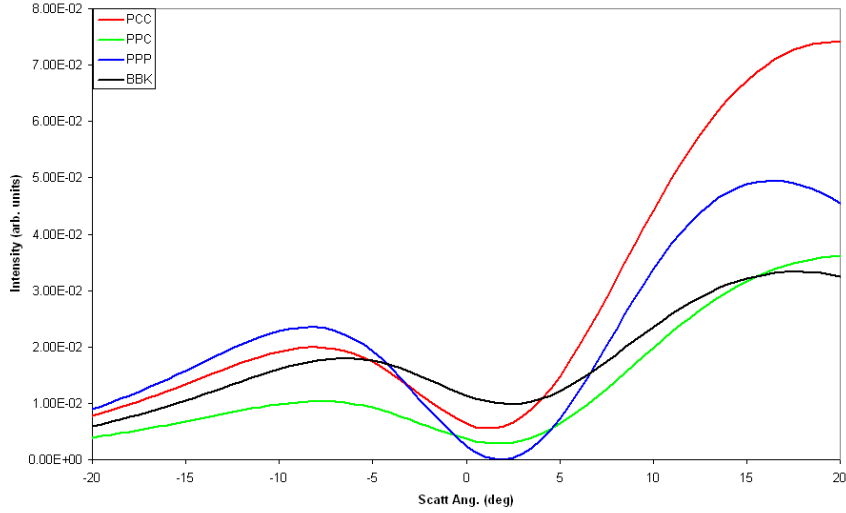


Figure B.1: Sample theoretical scattered angular distribution. Incident energy is 150 eV, and ejected electron angle of -90° .

theoretical calculations we hoped to determine if the finite size of the interaction region could account for our inability to resolve the “zig-zag” feature (see sections 6.2 and 6.4) in some of our experiments. Examples of these calculations (for a fixed ejected electron angle of -90°) are shown in figure B.1; figure B.2 shows a difference of two spectra, and provides an example of the “zig-zag” feature [2].

A schematic diagram of the apparatus being modeled is shown in figure 5.1 and is described in sections 5.1 through 5.7. Briefly, the apparatus consists of an unmonochromated electron gun, a scattered electron spectrometer, and two identical ejected electron spectrometers mounted 180° apart on the same turntable; all these elements are coplanar and all analyzers are hemispherical-sector electrostatic types [21]. Specifically, this work has modelled the scattered, and an ejected, electron spectrometer. The spectrometers were modelled individually; i.e., each simulation was of a single spectrometer. It should be noted that the voltages used in simulating each set of optics or entire spectrometer were close to (and often the same as) the voltages used on the actual apparatus.

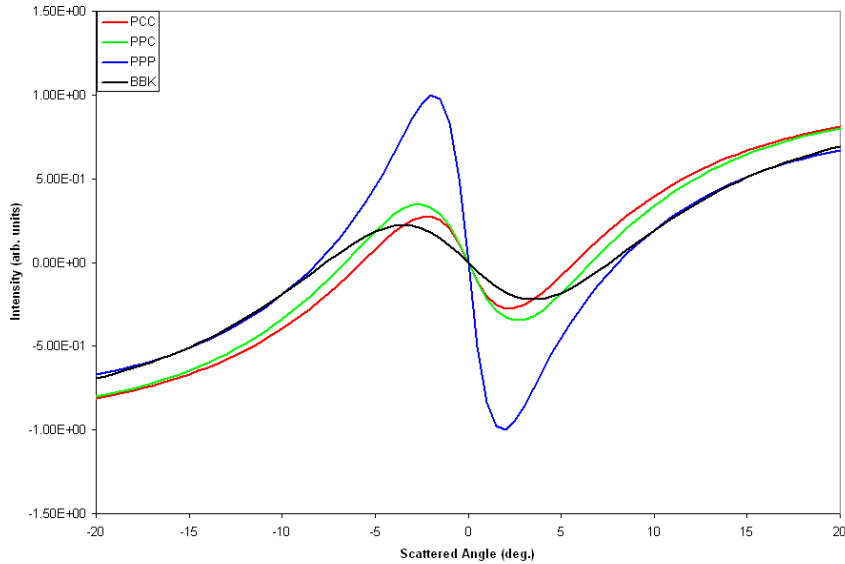


Figure B.2: Sample theoretical “difference” scattered angular distribution. Incident energy is 150 eV, and ejected electron angles of $\pm 90^\circ$.

B.3 Model Considerations

B.3.1 Potential Array Size

A spectrometer is modelled in SIMION by a potential array. The size (in number of points) of a potential array affects the accuracy with which SIMION can compute the trajectory of an electron travelling through it; so it would seem that one would want to make very large potential arrays to ensure accuracy. On the other hand the larger the array the longer the time required to compute a trajectory. So the goal is to size the array such that the required level of accuracy as well as reasonable performance are achieved.

Having no *a priori* knowledge of the details of the electron trajectories through the optics, one must decide on some other criteria to determine if a reasonable level of accuracy had been achieved. Two criteria which may be useful for judging the accuracy of a model are:

1. The angular distribution of electrons leaving the lens system should be smooth. Imagine a point source of electrons at the origin, and a lens system that is coaxial with the x-axis, with the entrance aperture of the lens some distance from the

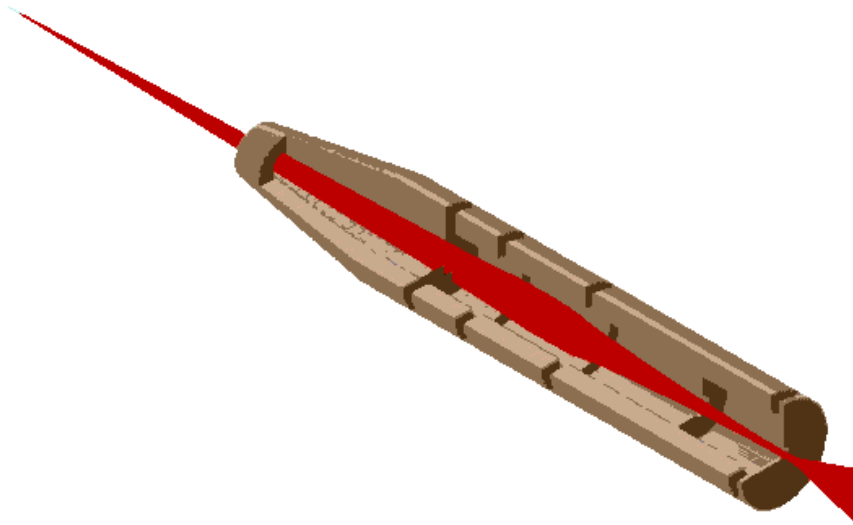


Figure B.3: Isometric view of the ejected lens. Electrons (in red) passing through a cut-away isometric view of the ejected lens system.

origin. Electrons leaving the point source are all given the same initial energy, but start off with trajectories that form a regular distribution of angles with respect to the x-axis. I expect that the distribution of angles that the trajectories of the electrons (that make it through the lens) will be smooth.

2. SIMION calculates (based on conservation of energy) a Kinetic Energy Error. Note that this error is only valid when using static potentials.[97] I expect that as the trajectory calculations become more accurate this error will become relatively small.

To find an array size that was appropriate for our purposes, models of our ejected lens system were created using potential arrays of various sizes. Each potential array (lens) was positioned in the ion optical workbench so that it was coaxial with the x-axis. Electrons leaving a point source at the origin with initial trajectories that lay within the xy plane, were flown through each lens (figure B.3 shows an example of this).

The distribution of positions that the electrons had after passing through the different sized arrays is shown in figure B.4. The horizontal scale indicates the angle of the initial trajectory relative to the x-axis. The vertical scale represents the final vertical position (i.e., the y-coordinate of the simulated electron when it reached the end of the simulated space; this is the right-hand edge of the trajectories shown in figure B.3).

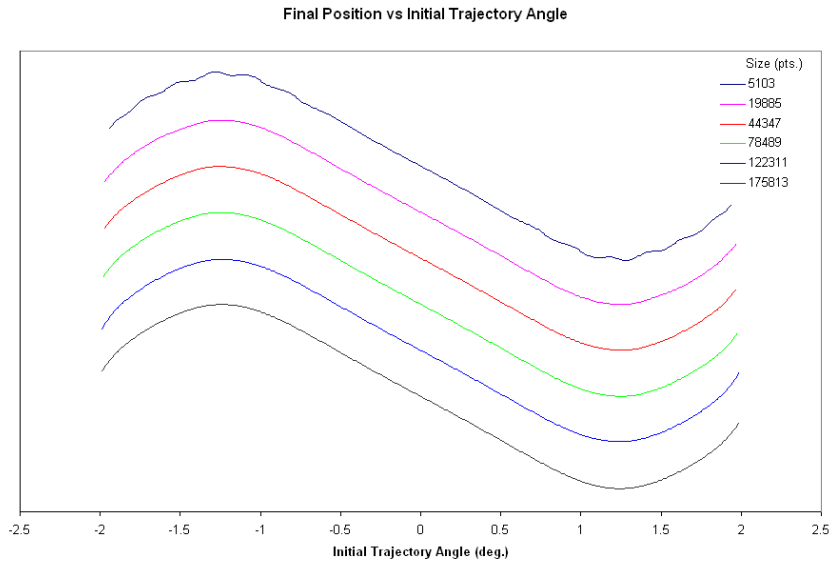


Figure B.4: Initial trajectory angle versus final position for arrays of various sizes. The horizontal axis gives the angle of the initial trajectory of each electron relative to the x-axis. The vertical axis gives the final y-coordinate for each simulated electron. The curves actually lie one atop another, but have been shifted to allow for easier comparisons.

Note that the curves in figure B.4 actually lie one atop another, but have been shifted vertically to allow for easier comparison. Notice that the curve for the 5103 point array is ragged while those for the larger arrays are relatively smooth. Figure B.5 shows the error in the kinetic energy that SIMION computed for each electron after the electron had passed through the various potential arrays. The errors associated with the 44347 point array are (roughly) an order of magnitude less than those for 5103 point array. The errors of the 122311 point array are (predictably) better than those for the 44347 point array, however one can already see that the increases in accuracy are diminishing in comparison with the increases in array size. For the present work the 122311 point array (with maximum and average percent errors of approximately 0.2% and 0.05% respectively) seems to provide a reasonable level of accuracy.

B.3.2 Distribution of Trajectories

As already stated, my main goal was to find the instrument function for the spectrometers. To accomplish this I needed to simulate electrons leaving the interaction region. I

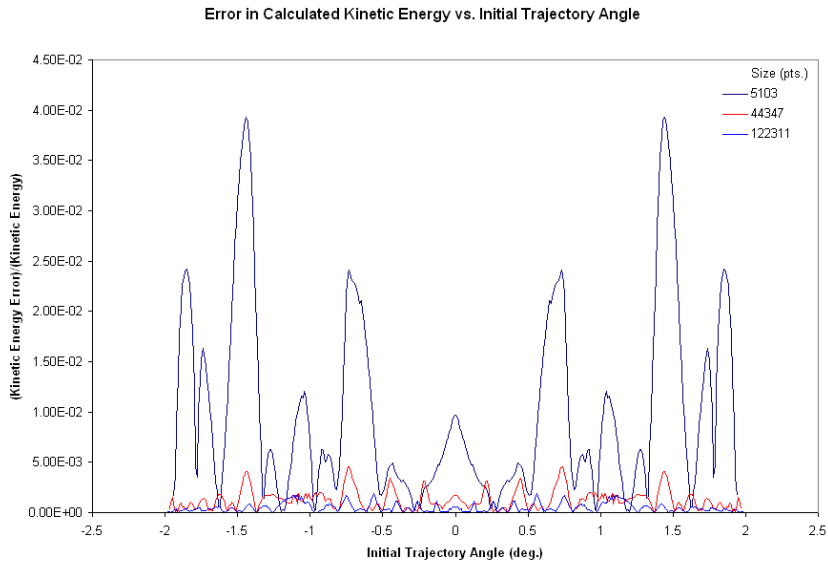


Figure B.5: Initial trajectory angle versus the error in the calculated value of the final kinetic energy (specifically $\frac{\text{Error in Calculated Kinetic Energy}}{\text{Calculated Kinetic Energy}}$) of the electron for arrays of various sizes.

wanted the distribution of electron trajectories leaving a point in the interaction region to be isotropic (at least within some solid angle that is greater than the lens system’s angular acceptance) both to simplify the determination of the angular acceptance of a spectrometer, and to provide an easy way to visualize the distortion of the distribution after it has passed through a spectrometer.

The simplest way of creating an isotropic distribution of trajectories is to have a user program that randomly assigns values of θ and ϕ to each initial trajectory (it is not possible to create a regular “grid” that meets this requirement). This method, although practical when modelling the interaction region as a single point source, was found to be too computationally intensive when modelling a finite interaction region; basically, too many randomly created trajectories needed to be “flowed” through a simulated spectrometer to get reasonable statistics. To circumvent this problem I wrote an algorithm that creates a semi-random set of unit vectors (which can then be scaled as needed) that is “fairly” isotropic (the distribution is shown in figure B.6). The algorithm used to create the distribution basically adds “rings” of trajectories in such a way that as each ring is added the density of trajectories is kept constant. A plot of the y and z

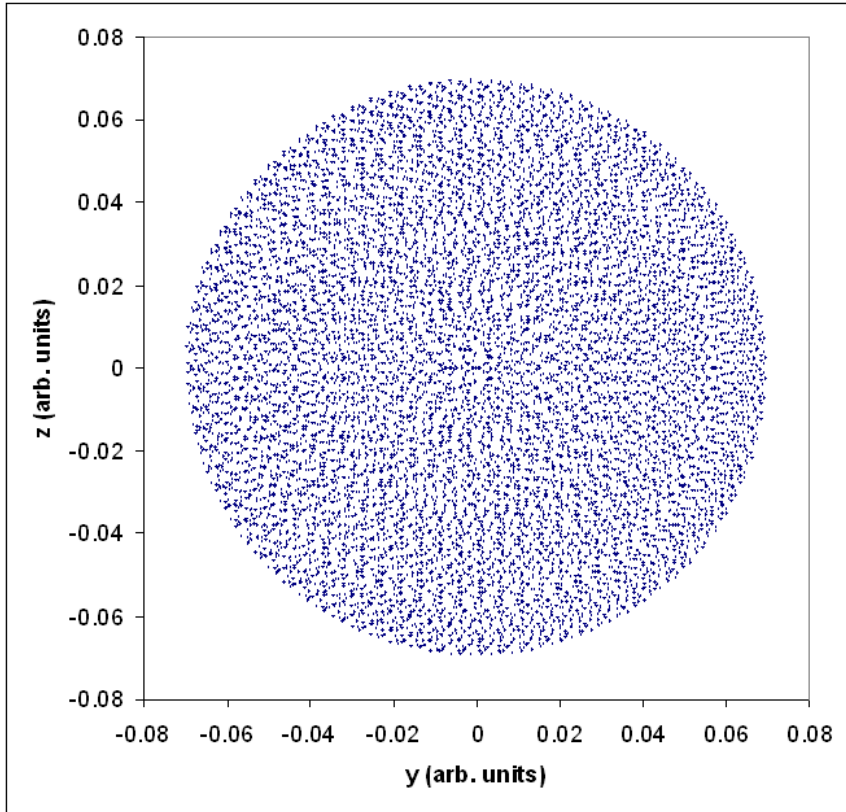


Figure B.6: The y and z components of the set of unit vectors used to create a (fairly) isotropic angular distribution of trajectories. This set contains 10^4 points, and subtends an angle of approximately 4° about the x axis.

coordinates of these unit vectors is shown in figure B.6. Use of this set of vectors gave good agreement when compared to using a set of random vectors several times as large.

B.4 Point Source

Before attempting to model a finite interaction region we modeled the interaction region as a point source. The point source is on the x -axis, which is coaxial with the simulated optics. Figure B.7 shows electrons being flown through the combined scattered lens system and hemispherical energy analyzer. The initial trajectories of the electrons were determined using the first 500 unit vectors of the set of vectors described above. The electrons that make it through the scattered lens and the hemispherical analyzer can then be binned based on their initial trajectory to determine the angular acceptance of the scattered optics. Bins can be assigned based on (see figure B.8):

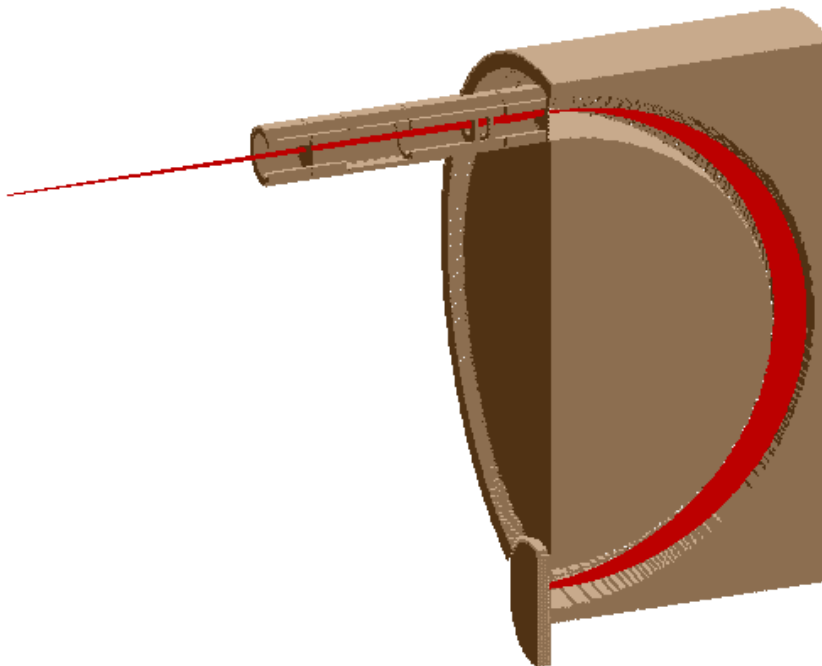


Figure B.7: A cut away view of electrons flying through the scattered lens system and the hemispherical energy analyzer. This figure shows the trajectories of 500 electrons. The unit vectors for the initial trajectories are a subset of the 10^4 points shown in figure B.6.

1. The angle formed by the x-axis and the initial direction of the electron trajectory. This angle will be referred to as θ .
2. The angle formed by the x-axis and the projection onto the xy-plane of the initial direction of the electron trajectory. This angle will be referred to as ϕ . The distribution obtained by binning by ϕ will make it easier to visualize the instrument function when dealing with an interaction region shaped like a line.

These two distributions can be quite different (see figures B.9 and B.10).

Regardless of how the angles are binned, simulations of the scattered electron spectrometer suggest that spectrometer has a small angular acceptance (0.6° or less). Meanwhile, simulations of an ejected electron spectrometer suggest that it has a much larger angular acceptance ($\sim 6^\circ$). Figures B.11 and B.12 show a simulation of where electrons would strike a PSD (see section 5.4)¹. The simulations for both figures used the same

¹Admittedly the scattered electron spectrometer does not, in reality, have a PSD. However, for this simulation the exit aperture of the scattered analyzer has been replaced with a PSD

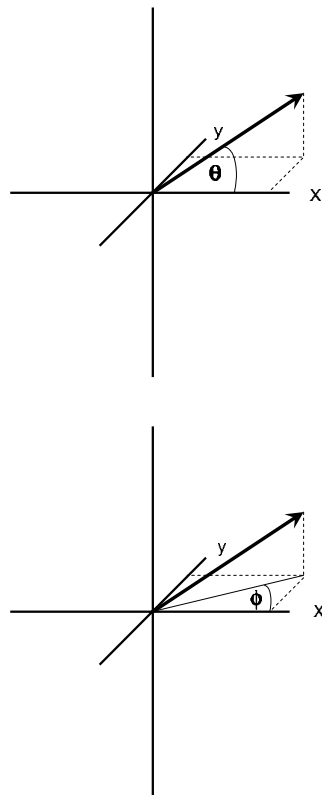


Figure B.8: Definition of angles. The top figure shows the definition for the angle θ , while the bottom shows ϕ .

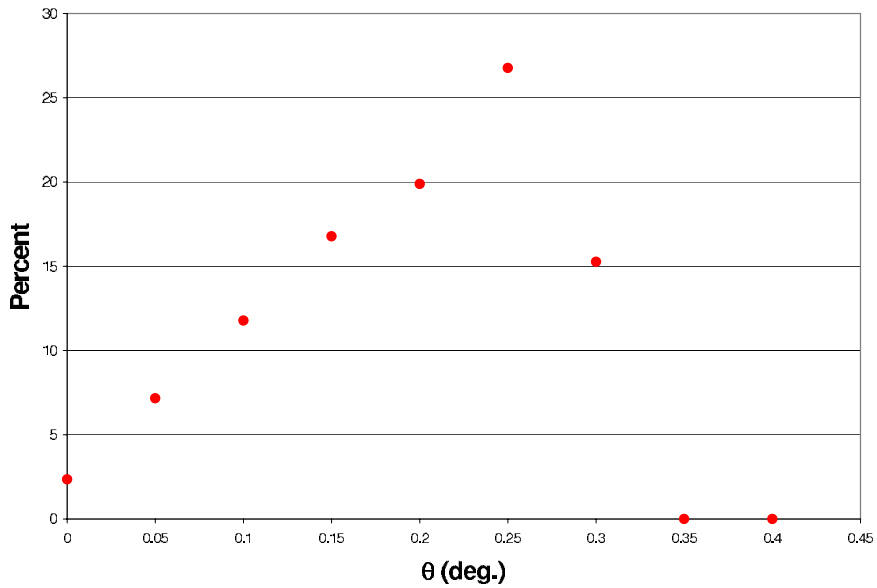


Figure B.9: Simulated angular acceptance of electrons (from a point source) binned by value of θ . The contribution of each bin to the total number of electrons that passed successfully through the spectrometer is shown on the vertical axis as a percentage. The bins are 0.5° wide. See the text and figure B.8 for the definition of θ .

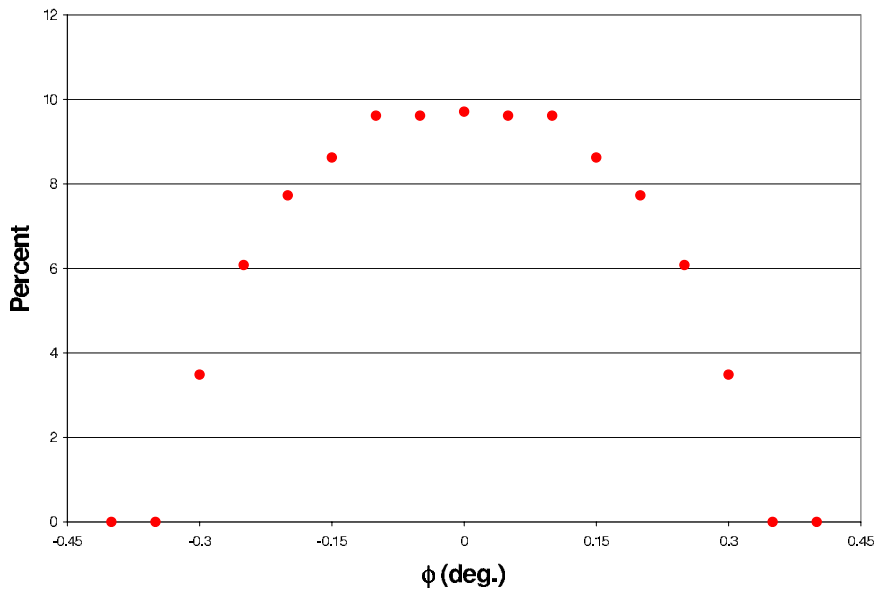


Figure B.10: Simulated angular acceptance of electrons (from a point source) binned by value of ϕ . The contribution of each bin to the total number of electrons that passed successfully through the spectrometer is shown on the vertical axis as a percentage. The bins are 0.5° wide. See the text and figure B.8 for the definition of θ .

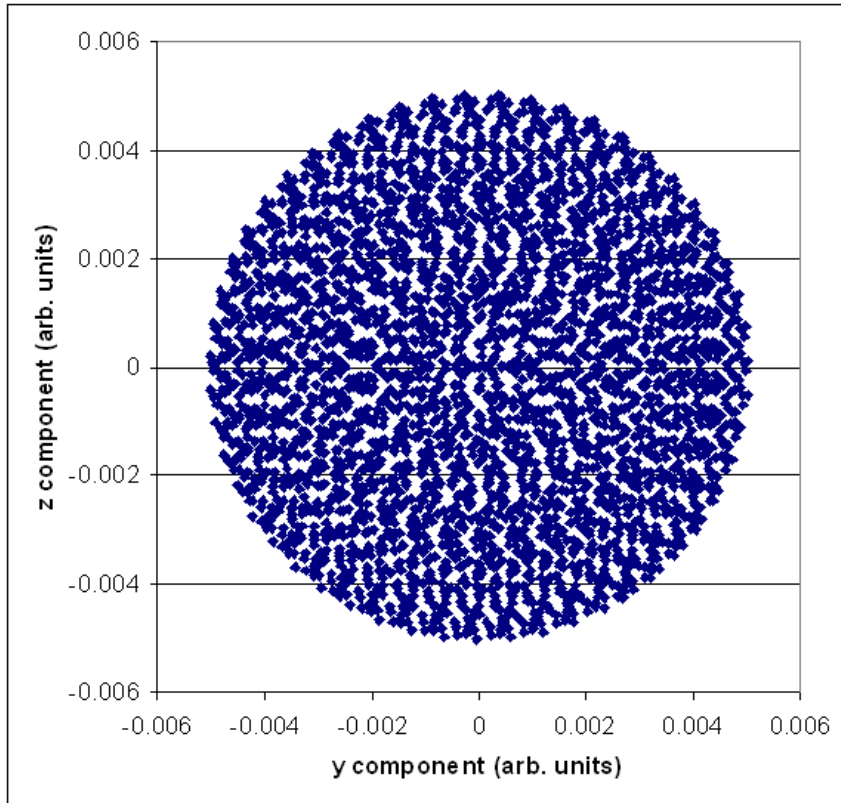


Figure B.11: Simulated distribution of electrons that have passed through the scattered optics and hemispherical energy analyzer. The initial (i.e., before entering the scattered spectrometer optics) distribution of electron trajectories is shown in figure B.6.

initial set of electron directions (shown in figure B.6); this initial distribution was scaled differently for the two simulations to account for the difference in energies of the electron detected by the two different spectrometers. Figure B.11 suggests that the scattered spectrometer, with its small angular acceptance and high pass energy, preserves the cylindrical symmetry of the initial distribution of trajectories. Meanwhile, figure B.12 suggests that the ejected spectrometer, which has a large angular acceptance and low pass energy, destroys this symmetry.

Folding the distribution shown in figure B.10 with theory (figure B.2) changes the predicted values by (at most) $+2\% \rightarrow -3.5\%$. The ratio of the corrected to the uncorrected values is shown in figure B.13.

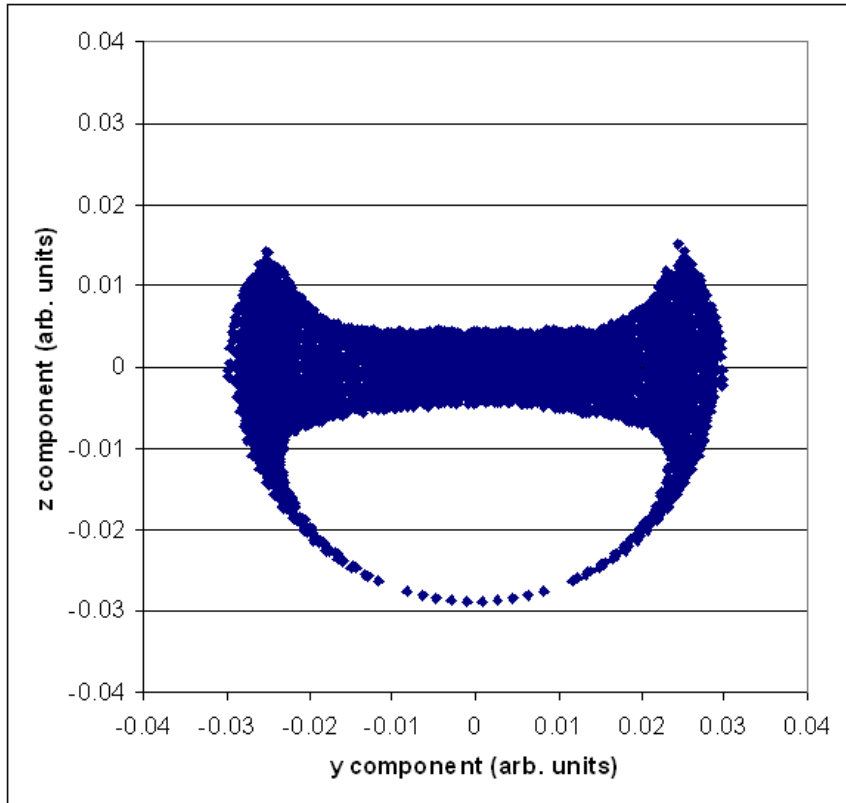


Figure B.12: Simulated distribution of electrons that have passed through the ejected optics and hemispherical energy analyzer. The initial (i.e., before entering the ejected spectrometer optics) distribution of electron trajectories is shown in figure B.6.

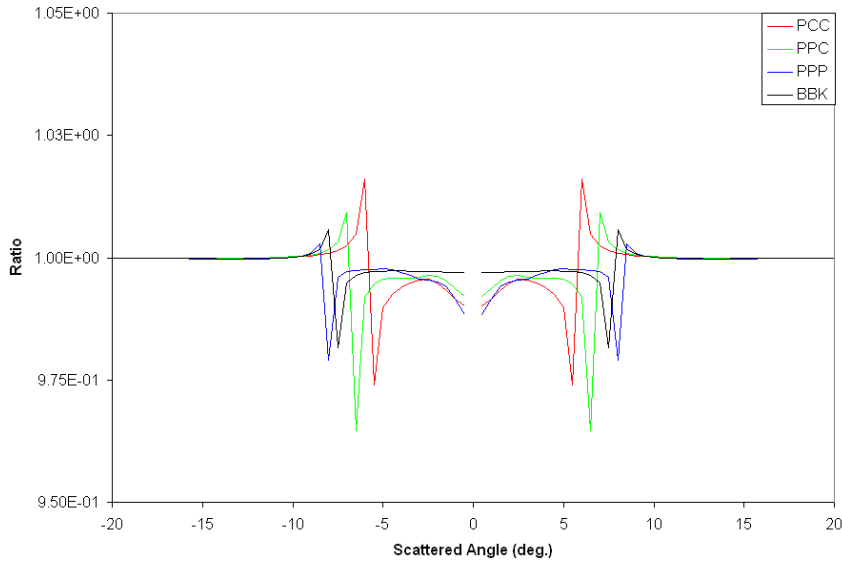


Figure B.13: Ratio of theoretical values which have been folded with the angular acceptance (assuming a point interaction region) to the unfolded theoretical values.

B.5 Line Source

We modeled the interaction region as a line source; i.e., as a series of point sources along a line. The length of the line (approx. 16 mm) was dictated by the region that is visible to the ejected optics (only that portion of the interaction region that is visible to both the ejected and scattered optics is of interest since these are coincidence experiments). The shape and width of the angular acceptance for the scattered optics varies significantly as the angular position of the detector is varied (see figure B.14).

Folding this angular acceptance with the theoretical calculations (figure B.1) had a slight effect (see figure B.15 for a comparison of the theoretical values; untouched, folded with the results from a point interaction region, and folded with the results from a line).

B.6 Predicted versus Actual Results

In general, one wants to know if a simulation reflects reality. In our case we wanted a way to test the simulation where we would be fairly certain that the real and simulated interaction regions were the same. A simple solution was to move the (actual, not

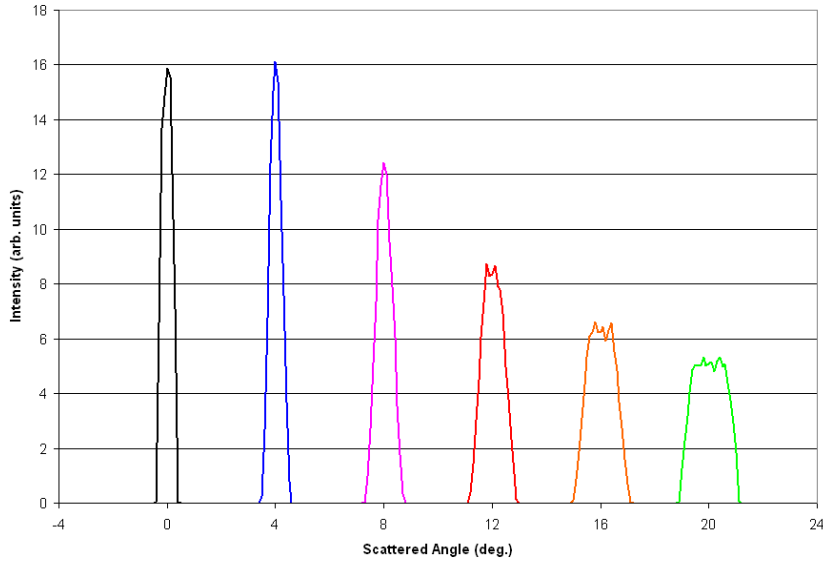


Figure B.14: Angular acceptance and intensity assuming a line shaped interaction region. Each peak corresponds to the scattered detector being positioned at a particular angle (indicated at the bottom of the graph). The area under the peak indicates the intensity for that position. The width of the peak shows the angular acceptance, while the height indicates the contribution of that angle to the intensity.

simulated) atomic beam out of the interaction region; i.e., the gas nozzle that formed the atomic beam was moved from a vertical position in the middle of the apparatus to a horizontal position on the bottom. We therefore knew that the gas pressure in the interaction region was (roughly) constant and equal to the background pressure, and that the interaction region was the entire volume of the electron beam (or, effectively, that part of the beam visible to the various lens systems). Several measurements of scattered count rates for various scattering angles were made with the apparatus in this configuration. Comparisons with simulated results ² for a line shaped interaction region showed discrepancies of 5% or less.

²Of course the simulations could not be expected to match the measurements on an absolute scale. To make the comparisons we scaled the simulated number of counts for one scattering angle to match the actual measurement. We then scaled the other simulated values by the same scaling factor and compared each to its corresponding measurement.

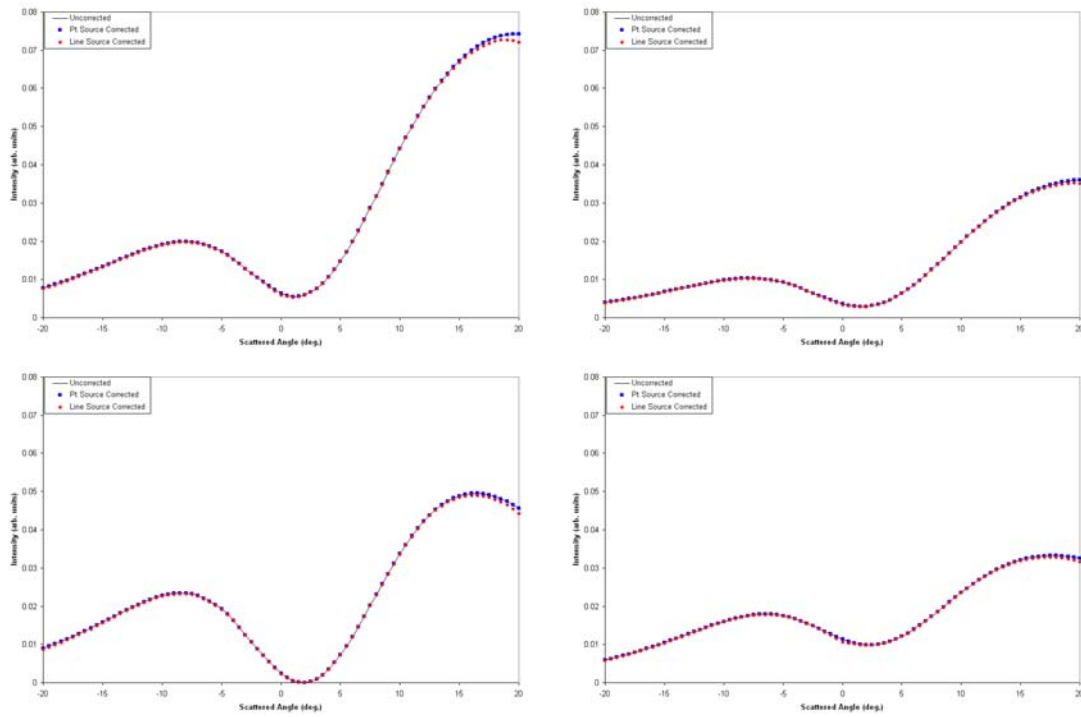


Figure B.15: Results of folding the instrument function assuming point interaction region (labeled *Pt Source Corrected*) or a line interaction region (labeled *Line Source Corrected*) with the calculated TDCS for an ejected electron angle of -90° (as shown in figure B.1).

B.7 Conclusion

A set of simulations have been run to find the instrument function resulting from a finite sized interaction region. It was found that this instrument function does not account for the difficulties in resolving the “zig-zag” feature described in chapter 6. The simulations also indicate that a spectrometer tuned to have a small angular acceptance ($\sim 0.6^\circ$) exhibits cylindrical symmetry (i.e., only the angle of the electron’s trajectory relative to the axis of the spectrometer lenses is important), while a spectrometer exhibiting a relatively large angular acceptance ($\sim 6^\circ$) is very asymmetric.

Appendix C

Thermal broadening

When we consider an electron impact ionization experiment, we normally treat the target atom as being at rest. Of course the reality is that the target moves. Let us assume that we need only worry about thermal motion. For our experiments, this motion might affect:

1. The incident energy (in the target frame).
2. The scattered angle (in the lab frame).
3. The ejected angle (in the lab frame).
4. The ejected electron energy (in the lab frame).

The greatest effect on the incident energy will occur for the case where the atom is moving parallel (or anti-parallel) to the incident electron (which I will say is the \hat{z} direction). What is the probability that an atom will have a given velocity along one axis (i.e., I would like to know the probability of a particular z-component of the velocity)? I start with the probability that an atom will have a particular momentum, which is [98, eqn. 13.12]:

$$\mathcal{P}(\vec{p})d^3p = \frac{e^{-p^2/2mkT}}{(2\pi mkT)^{3/2}}d^3p \quad (\text{C.1})$$

To get the probability for only one component of the momentum I integrate over the other two momenta:

$$\mathcal{P}(p_z)dp_z = \frac{\int dp_x dp_y e^{-(p_x^2+p_y^2+p_z^2)/2mkT}}{(2\pi mkT)^{3/2}}dp_z \quad (\text{C.2})$$

$$\mathcal{P}(p_z)dp_z = \frac{e^{-p_z^2/2mkT}}{(2\pi mkT)^{1/2}}dp_z \quad (\text{C.3})$$

A change in variables ($p_z = mv_z$) is now needed:

$$\mathcal{P}(v_z)dv_z = \sqrt{\frac{m}{2\pi kT}}e^{-mv_z^2/2kT}dv_z \quad (\text{C.4})$$

We will use the following mass and temperature for the helium atoms:

$$m_{He} = 6.65 * 10^{-27} \text{ kg}$$

$$T = 300 \text{ K}$$

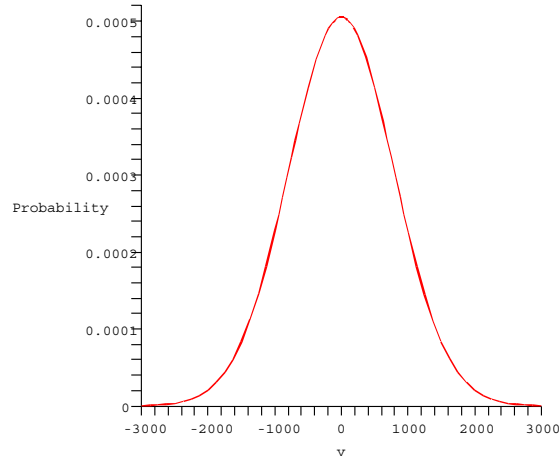


Figure C.1: Distribution of velocities along a single axis for Helium at a temperature of 300K.

These values give a distribution of velocities along a single axis as shown in figure C.1. The full width at half maximum (FWHM) occurs at approximately ± 930 m/s.

Meanwhile, a 448 eV electron has a speed v_0 found from:

$$\begin{aligned}
 m_e &= 9.11 * 10^{-31} \text{ kg} \\
 1 \text{ eV} &= 1.60 * 10^{-19} \text{ J} \\
 448 \text{ eV} &= 7.248 * 10^{-17} \text{ J} \\
 \frac{m_e v_0^2}{2} &= 7.248 * 10^{-17} \text{ J} \\
 v_0^2 &= \frac{2 * 7.248 * 10^{-17}}{9.11 * 10^{-31}} \\
 v_0^2 &= 1.59 * 10^{14} \text{ (ms}^{-1}\text{)}^2 \\
 v_0 &= 1.26 * 10^7 \text{ ms}^{-1}
 \end{aligned}$$

Adding ± 900 m/s should not have an appreciable affect on the velocity of the incident electron. To be exact, the energy shift (when we go to the atom's rest frame) is:

$$\begin{aligned}
 \Delta E_0 &= \frac{1}{2} m_e \{ (v_0 + v_{atom})^2 - v_0^2 \} \\
 \Delta E_0 &= \frac{1}{2} 9.11 * 10^{-31} \{ (1.26 * 10^7 + 1000)^2 - (1.26 * 10^7)^2 \} \\
 \Delta E_0 &= 1.193 * 10^{-20} \text{ J} \\
 \Delta E_0 &= 0.0746 \text{ eV}
 \end{aligned}$$

This is considerably less than the presumed spread of energies in the electron beam (section 5.2).

Suppose that the atom's velocity is perpendicular to the electron beam's, is there an appreciable change in incident angle $\Delta\theta_0$?

$$\begin{aligned}\Delta\theta_0 &= \arctan\left(\frac{930}{1.31 * 10^7}\right) \\ \Delta\theta_0 &= 0.004^\circ\end{aligned}$$

Which is insignificant for our purposes. Now let us check if the ejected angle might change significantly. For convenience we will assume the ejected angle θ_{ej} is 90° . The most extreme change in this angle would be when the atom is moving perpendicular to the ejected electron. The ejected angle in the lab frame θ'_{ej} and the change in angle $\Delta\theta_{ej}$ are:

$$\begin{aligned}\theta'_{ej} &= \arctan\left(\frac{v_{ej}}{v_{atom}}\right) \\ \Delta\theta_{ej} &= \theta_{ej} - \theta'_{ej}\end{aligned}$$

For a 35 eV ejected electron the velocity is:

$$\begin{aligned}35 \text{ eV} &= 5.6 * 10^{-18} \text{ J} \\ \frac{m_e v_{ej}^2}{2} &= 5.6 * 10^{-18} \text{ J} \\ v_{ej}^2 &= \frac{2 * 5.6 * 10^{-18}}{9.11 * 10^{-31}} \\ v_{ej}^2 &= 1.23 * 10^{13} (ms^{-1})^2 \\ v_{ej} &= 3.51 * 10^6 ms^{-1}\end{aligned}$$

Use this to find the change in angle:

$$\begin{aligned}\theta_{ej} &= 90^\circ \\ \theta'_{ej} &= \arctan\left(\frac{3.51 * 10^6}{930}\right) \\ \theta'_{ej} &= 89.98^\circ \\ \Delta\theta_{ej} &= 90^\circ - 89.98^\circ \\ \Delta\theta_{ej} &= 0.02^\circ\end{aligned}$$

Which is also too small a shift for us to be concerned with.

The only concern we are left with is the possible shift in the ejected electron energy in the lab frame. How big an effect will this be? If the atom has a velocity of 930 m/s in the direction of the ejected electron, the shift will be:

$$\begin{aligned}\Delta E'_{ej} &= \frac{1}{2}m_e \{(v_{ej} + v_{atom})^2 - v_{ej}^2\} \\ \Delta E'_{ej} &= \frac{1}{2}9.11 * 10^{-31} \{(3.51 * 10^6 + 930)^2 - (3.51 * 10^6)^2\} \\ \Delta E'_{ej} &= 3.20 * 10^{-21} J \\ \Delta E'_{ej} &= 0.020 eV\end{aligned}$$

Of course the atom could also be travelling in the exact opposite direction, so the total shift will be $\Delta E_{ej} = 2\Delta E'_{ej} = 0.040$ eV, which can be significant. Note that this compares well with the result we obtained in appendix A using equation A.1.

C.1 Conclusion

The only perceptible effect of the thermal motion of the target atoms is to broaden the energies of the ejected electrons in the lab frame. Since the thermal motion is in all directions this does not result in an overall shift in energy, but rather a broadening of any resonance features; i.e., there is a loss in resolution.

Appendix D

Analytical expression for a scaling factor

Suppose I have a set of theoretically determined absolute cross-sections, and a set of experimentally measured relative (as opposed to absolute) cross-section. I want to determine the scaling factors to give the theoretical values the same relative magnitudes as the experimental data. In general I do this by finding the scaling factor that minimizes χ^2 :

$$\chi^2 = \sum_{n=0}^N \frac{(\nu_n - \mu_n)^2}{\mu_n} \quad (\text{D.1})$$

where :

ν_n = experimental values

μ_n = $a x_n$

x_n = theoretical values

a = scaling factor

We usually do this numerically, but is there an analytic result if we assume that Poisson statistics are obeyed?

Following the principle of maximum likelihood, I want to maximize the probability that I would obtain my particular data set; i.e., assuming the theoretical values are the expected values, how do I scale them so that the probability for my data set is maximized? The Poisson distribution is:

$$P_{\mu}(\nu) = \frac{\mu^{\nu}}{\nu!} e^{-\mu} \quad (\text{D.2})$$

where :

μ = the expected value

ν = the actual value

So for an expected value $\mu_n = a x_n$ the probability of getting a particular value ν_n follows the proportionality relation:

$$P(\nu_n) \propto \frac{(a x_n)^{\nu_n}}{\nu_n!} e^{-a x_n} \quad (\text{D.3})$$

and the probability of obtaining a dataset $\{\nu_n\}$ given the expected values $\{a x_n\}$ is

$$P(\{\nu_n\}) \propto \prod_{n=1}^N \frac{(a x_n)^{\nu_n}}{\nu_n!} e^{-a x_n}, \quad (\text{D.4})$$

where N is the number of datapoints. To find the value of a that maximizes the probability simply requires setting the derivative of $P(\{\nu_n\})$ with respect to a equal to 0:

$$\begin{aligned} \frac{\partial}{\partial a} \left[\prod_{n=0}^N \frac{(a x_n)^{\nu_n}}{\nu_n!} e^{-a x_n} \right] &= 0 \\ \frac{\partial}{\partial a} \left[\prod \frac{x_n^{\nu_n}}{\nu_n!} a^{\nu_n} e^{-a x_n} \right] &= 0 \\ \frac{\partial}{\partial a} \left[\prod \frac{x_n^{\nu_n}}{\nu_n!} e^{\nu_n \ln(a)} e^{-a x_n} \right] &= 0 \\ \frac{\partial}{\partial a} \left[\prod \frac{x_n^{\nu_n}}{\nu_n!} e^{\nu_n \ln(a) - a x_n} \right] &= 0 \\ \left[\prod \frac{x_n^{\nu_n}}{\nu_n!} \right] \frac{\partial}{\partial a} e^{\sum (\nu_n \ln(a) - a x_n)} &= 0 \\ \frac{\partial}{\partial a} e^{\sum (\nu_n \ln(a) - a x_n)} &= 0 \\ \sum_{n=0}^N \left[\frac{\nu_n}{a} - x_n \right] &= 0 \\ \sum [\nu_n - a x_n] &= 0 \\ a &= \frac{\sum \nu_n}{\sum x_n} \end{aligned} \quad (\text{D.5})$$

Equation D.5 shows that, to the extent that the experimental datapoints follow Poisson statistics, a scaling factor to compare absolute theoretical values to the relative experimental data can be found simply by dividing the sum of the experimental values by the sum of the theoretical values. This method is simpler than fitting the scaling factor.

Appendix E

Effects of bin size on resolution

E.1 Introduction

Electrons with a range of energies pass through the spectrometer's electrostatic energy analyzer and subsequently impact the micro-channel plates (MCP) which cause a burst of electrons to strike the position sensitive detector (PSD); the position where this burst of electrons strikes the PSD is indicative of the position that the initial electron struck the MCP. Looking at the position indicated by the PSD is therefore indicative of the energy of the electron. This position is encoded as a binary number, and must therefore be binned. It is convenient to use bins of the same size (additionally this is the way the electronics for the PSD is built). Since position is indicative of energy, we can describe the width of the bin in terms of energy. This width is determined by:

1. the dimensions of the analyzer,
2. the difference in potential between the two hemispheres of the analyzer,
3. and the number of bins that are being used.

As long as the three quantities listed are kept constant, the bin size will remain constant.

In a typical experiment we want to take a spectrum over an energy range far greater than is passed by the analyzer. It is therefore necessary to scan over a range of energies (i.e., to take a series of measurements where the pass energy of the analyzer is incremented in a regular manner). Note that the potential across the hemispheres is not varied during this process (see section 5.4). Suppose that we have divided the PSD into four bins, each of which is one unit of energy wide (actually we use thirty-two or forty bins, and the width of each bin is several meV). Further, suppose we want to take a spectrum that spans eight units of energy. The simplest way to obtain the spectrum would be to take two measurements. The first measurement would have electrons with the lowest energy of the spectrum striking the edge of the first bin, and electrons with energies four units higher striking the edge of the fourth bin. The second measurement would have a pass energy four units higher. This would work well except that the efficiencies (i.e., the percentage of electrons with an energy that falls within a bin that

are actually detected in a bin) of all of the bins are not the same. There are a variety of reasons for this, including (but not limited to) variations in the efficiency of different areas of the MCPs, variations in the surface of the PSD, and the geometry of the energy analyzer. Since these efficiencies vary (in an unknown way) the above method for taking a spectrum does not work well.

To overcome this problem we take a spectrum as illustrated in figure E.1. Rather than incrementing the pass energy by the amount of energy spanned by all of the bins (four units of energy for the example above and the figure), the pass energy is incremented by one bin width (the amount of energy by which the pass energy is incremented will be referred to as the *step size*). Each row in figure E.1 shows a different measurement. The four boxes in the row represent the four bins of the PSD. The curve shown within the boxes represents intensity versus energy, and the area under the curve in each box indicates the number of counts that should be binned in that box (assuming perfect efficiency). Notice that a given portion of the curve appears in a different bin for each row. By summing together bins from different rows (the bins that are summed together have the same color in the figure) we average the different efficiencies.

If the step size is different than the bin size (see figure E.2), the resolution of the spectrum obtained is affected. To examine these affects I have written code in Maple to simulate the manner in which we obtain spectral data. The spectrum being processed was always a Gaussian. For one of the simulations I wanted to examine the impulse response of the system. A typical definition of impulse response is “. . . the output of the system at time t due to an impulsive input at time τ ” [99, pg. 232]. For my purposes I have extended this definition to spatial coordinates; i.e. for my purposes the impulse response is the output of the system at position x due to a delta function $\delta(x - x_0)$. For the case where I simulated the impulse response of the system I used a Gaussian with a standard deviation of 0.0001; i.e., the expression used was $exp(-\frac{(x-\bar{x})^2}{2*(0.0001)^2})$.

E.2 Results

E.2.1 Impulse response

The impulse response is shown (for several selected step sizes) in figure E.3. Note that since this is a discrete system the lines connecting the points are only included as an

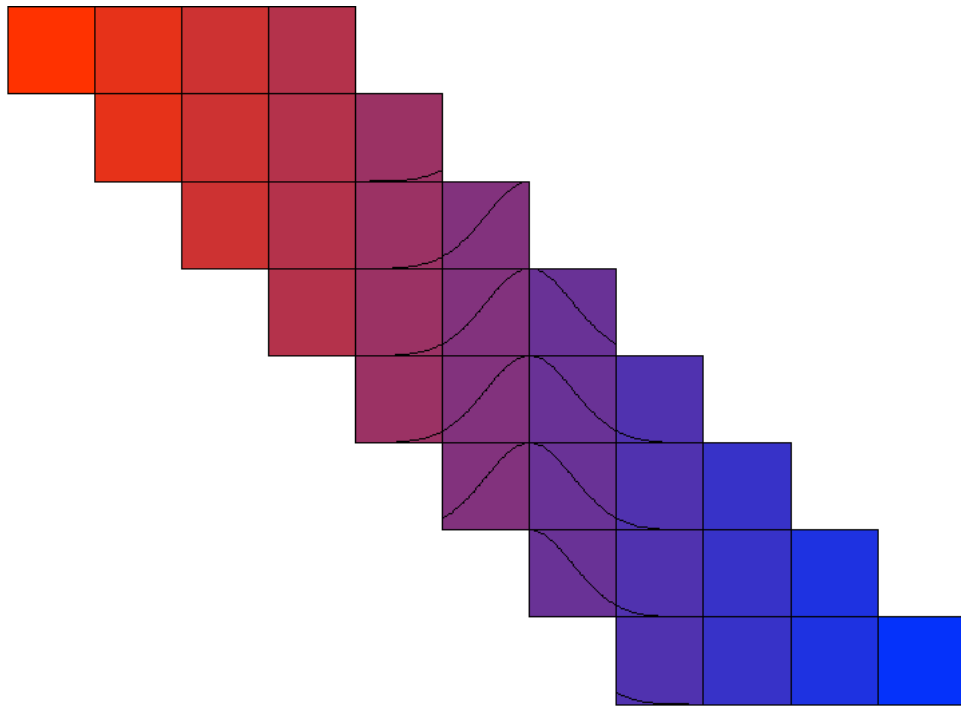


Figure E.1: Cartoon showing the process of obtaining a spectrum. Each row represents a set of measurements with the energy analyzer set for a particular pass energy. The pass energy for each row is one bin width higher than that for the previous row. Each box represents one bin of the PSD. The curve shown in the boxes of each row represents the intensity distribution that is being imaged. Bins of the same color are summed together to obtain the final spectrum.

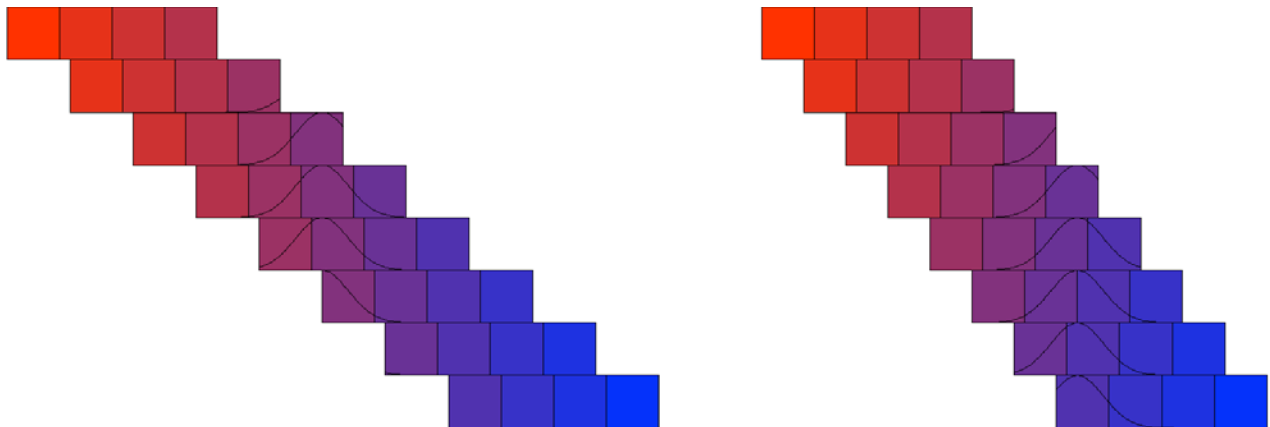


Figure E.2: Cartoon showing the process of obtaining a spectrum where the step size is incorrect. The step size is 110% (left) and 90% (right) of the bin size.

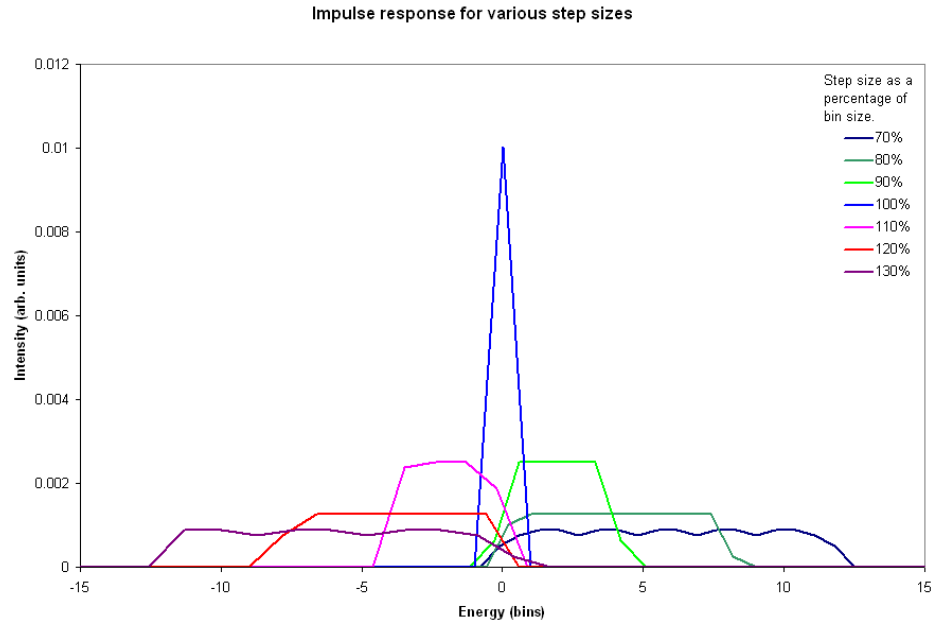


Figure E.3: Impulse response for various step sizes. The step sizes are expressed as percentages of the bin size.

aid to the eye and are in fact meaningless. One can therefore see that the response for a step size that is 100% of the bin size is a discrete delta function. The response for a step size of 70% and 130% of the bin size have a vaguely saw tooth form. This is because the number of times the delta function is imaged in a bin alternates between two values. Consider the case where the step size is four times the bin size, one can see that every other bin will image the delta function once, and the bins in between will not image the delta function at all.

E.2.2 The system is not invariant

If a system is linear and invariant one can figure out the response to an arbitrary input by convolving that input with the impulse response of the system. A system is invariant if a shift in the input signal (in our case the independent variable is energy, so we are talking about an energy shift) causes a shift in the output signal [100, p. 42]. In other words, if the input is some function $f(E)$ and the response is $y(E) = g(f(E))$, then the system is invariant if:

$$y(E + E') = g(f(E + E')) \tag{E.1}$$

Our system is clearly not invariant. Consider the rather unlikely case of the input being a square wave that is the same width as one of the bins. Further, let us assume that it is centered at an energy where it falls in exactly one bin. The output will have a single non-zero point. If we now shift the square wave so that it is centered at slightly higher energy then it will fall in two different bins; the output will then have two non-zero points, which is different than shifting the output. Since the system is not invariant, we should not expect to be able to convolve the input with the impulse response to get the output.

E.2.3 The area under the image is affected by the step size

We are imaging a Gaussian that has a certain area. For the case where the step size and bin size are equal the area of the image will simply be the number of bins times the area of the Gaussian (i.e., the area of the Gaussian is multiplied by the number of times a particular piece of the curve is imaged). When the step size is not equal to the bin size this is no longer true. Consider the image of a delta function; as long as it falls within the width of the PSD it will be imaged, and it will be within the width of the PSD for $(\text{number of bins}) \times (\text{bin width}) / (\text{step size})$ steps.

E.2.4 The image of a Gaussian is not a Gaussian

Figure E.4 shows an example where the step size is twice the bin size. Notice that it is impossible to fit a Gaussian to the image returned by the simulated imaging of a Gaussian (shown with black circles).

E.2.5 The resolution depends on *the size of the feature*

In this paper, when I talk about a feature, that feature has been distorted by all of the instrumental effects up to the combination of the MCPs (which I am assuming to be small and am not addressing) and the PSD. I will make the assumption that the error introduced by the PSD is independent of the error introduced by the rest of the apparatus. This assumption implies that the error from the PSD should be added in quadrature to the error caused by the various parts of the apparatus preceding the PSD.

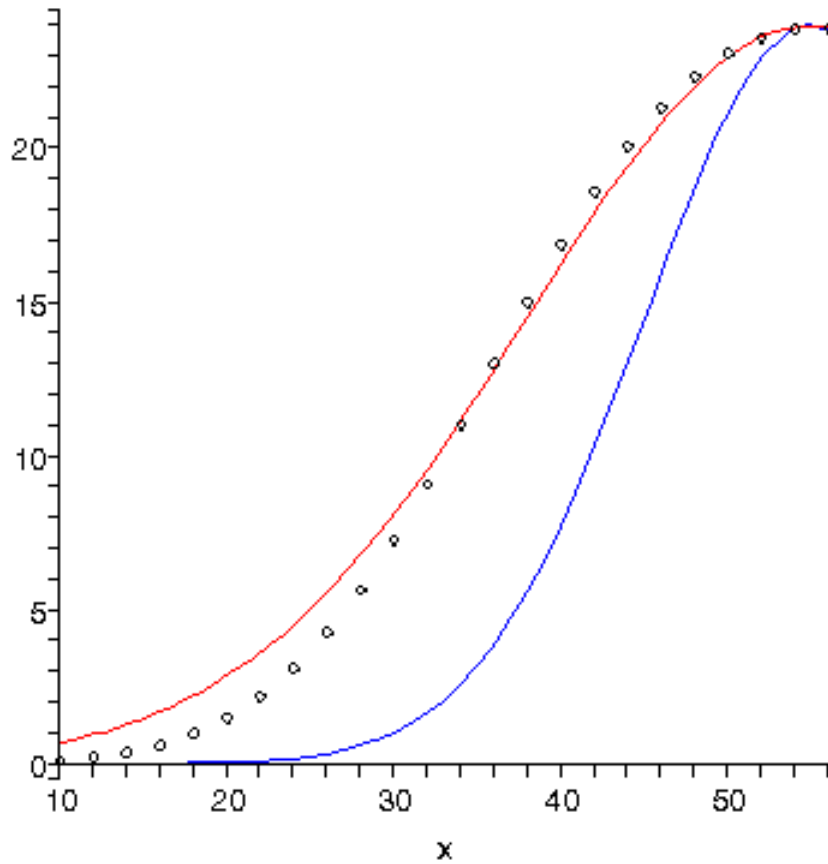


Figure E.4: Comparison of a Gaussian to its “image”. The Gaussian (with $\sigma = 20$ is shown by the blue line; its *image* shown with black circles. Additionally a Gaussian that has $\sigma = 34$ is shown by the red line. The unit for the x-axis is energy in bins; this is the true energy as opposed to the energy from the incorrect bin size. The y-axis indicates intensity using arbitrary units.

The total error will then be:

$$\sigma_{total} = \sqrt{\sigma_{before}^2 + \sigma_{PSD}^2} \quad (\text{E.2})$$

Where

σ_{before} = The error caused by the parts of the apparatus preceding the PSD.

σ_{PSD} = The error caused by the PSD.

In my simulation I am imaging Gaussians of particular widths; i.e., I am setting σ_{before} . I can then look at the width of the image to determine σ_{total} . The error caused by the incorrect step size is then:

$$\sigma_{PSD} = \sqrt{\sigma_{total}^2 - \sigma_{before}^2} \quad (\text{E.3})$$

Of course, in the expression I have been using for a Gaussian:

$$G_{\sigma, \bar{x}} = \exp\left(-\frac{(x - \bar{x})^2}{2 * \sigma^2}\right) \quad (\text{E.4})$$

the value of σ is not the FWHM (nor the HWHM for that matter). Rather it is the half width at $\exp(-1/2)$ times the maximum value. So when I examine the images I look at the half widths at $\exp(-1/2)$ times the maximum values. Using the Maple simulation I imaged Gaussians with $\sigma_{before} = \{1, 3, \text{ and } 10\}$ bins, using various step sizes; the results are shown in figure E.5. A few items to note are:

1. The error introduced by an incorrect step size is greater for a narrow feature and smaller for a broad feature.
2. For a step size that is the same as the bin width there is still a slight error introduced; this is because the bins act to integrate pieces of the curve (the effect is greater as the slope of the curve increases).
3. As the step size becomes grossly incorrect there is (for a given Gaussian being imaged) a fairly linear relation between step size and the error introduced.

E.3 Determining the bin size

To determine the bin size for each ejected electron spectrometer a xenon autoionizing resonance was chosen and imaged without stepping the voltage; i.e. a ramp voltage was

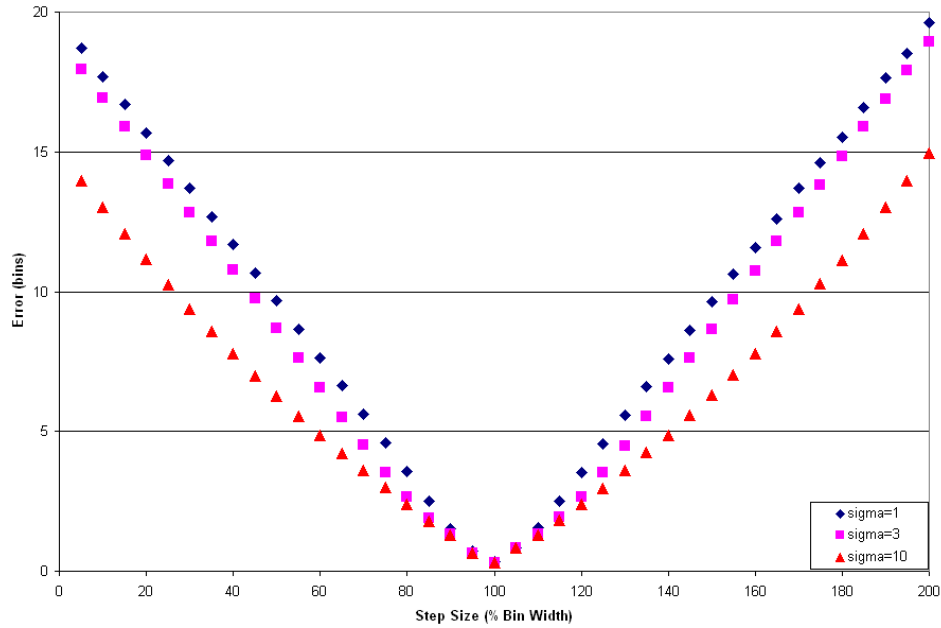


Figure E.5: Comparison of the error introduced by an incorrect step size for Gaussians of various widths.

selected and only that portion of the spectrum was obtained that was within the energy width of the PSD (see section 5.4). This was performed for several ramp voltages, so that the peak of the resonance fell within different bins (or channels) on the PSD. By performing a line fit to this data we were able to determine the bin size. Figure E.6 shows an example of the data, and line fit, for a set of measurements used to determine the bin size of the “red” spectrometer.

E.4 Conclusions

Use of an incorrect step size can have several subtle effects on the data being taken. Of particular concern is the case where an energy spectrum over multiple resonances is being obtained. These effects include distortion of the shape of the features, and the possibility that the energy resolution may differ for features of different (energy) width. We have therefore performed measurements to ensure that our step and bin sizes match.

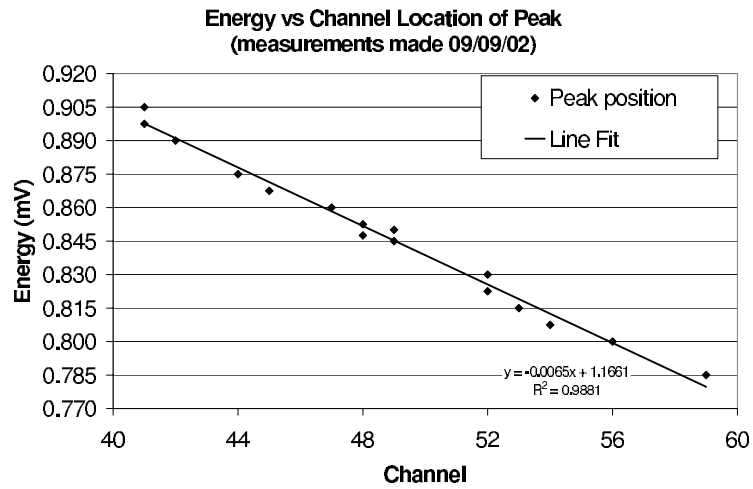


Figure E.6: Measurements to determine the bin size of the red spectrometer. Peak position refers to the position of the peak of a xenon autoionizing resonance. The vertical axis shows the ramp voltage for each measurement.

Bibliography

- [1] J. R. TAYLOR, *Scattering Theory: The Quantum Theory on Nonrelativistic Collisions*, John Wiley & Sons, Inc., 1972.
- [2] B. A. DEHARAK, Z. CHEN, D. H. MADISON, and N. L. S. MARTIN, *J. Phys. B* **38**, L145 (2005).
- [3] C. T. WHELAN, H. R. J. WALTERS, A. LAHMAM-BENNANI, and H. EHRHARDT, *(e, 2e) & related processes*, Kluwer Academic Publishers, 1993.
- [4] I. E. MCCARTHY and E. WEIGOLD, *Phys. Rep.* **27**, 275 (1976).
- [5] M. EMINYAN, K. B. MACADAM, J. SLEVIN, and H. KLEINPOPPEN, *Journal of Physics B: Atomic and Molecular Physics* **7**, 1519 (1974).
- [6] A. L. HUGHES and J. H. McMILLEN, *Phys. Rev.* **39**, 585 (1932).
- [7] E. C. BULLARD and H. S. W. MASSEY, *Proc. Roy. Soc. A* **130**, 579 (1931).
- [8] A. L. HUGHES and M. M. MANN, *Phys. Rev.* **53**, 50 (1938).
- [9] H. EHRHARDT, M. SCHULZ, T. TEKAAT, and K. WILLMANN, *Phys. Rev. Lett.* **22**, 89 (1969).
- [10] U. AMALDI JR., A. EGIDI, R. MARCONERO, and G. PIZZELLA, *Rev. of Sci. Instr.* **40**, 1001 (1969).
- [11] A. LAHMAM-BENNANI, *J. Phys. B* **24**, 2401 (1991).
- [12] I. E. MCCARTHY and E. WEIGOLD, *Electron-Atom Collisions*, Cambridge University Press, 1995.
- [13] H. FRAUENFELDER and E. M. HENLEY, *Subatomic Physics*, Prentice Hall, second edition, 1991.
- [14] J. J. SAKURAI, *Modern Quantum Mechanics*, Addison Wesley Longman, revised edition, 1994.

- [15] B. H. BRANSDEN, *Atomic Collision Theory*, W. A. Benjamin, Inc., 1970.
- [16] V. V. BALASHOV, S. S. LIPOVETSKIĬ, and V. S. SENASHENKO, *JETP* **36**, 858 (1973).
- [17] U. FANO, *Phys. Rev.* **124**, 1866 (1961).
- [18] R. D. COWAN, *The Theory of Atomic Structure and Spectra*, University of California Press, 1981.
- [19] J. G. CHILDERS, *A STUDY OF AUTOIONIZING RESONANCES IN NOBLE GASES USING (e, 2e) SPECTROSCOPY*, PhD thesis, University of Kentucky, 2001.
- [20] J. G. CHILDERS, D. B. THOMPSON, and N. L. S. MARTIN, *Phys. Rev. A* **64**, 062703 (2001).
- [21] B. A. DEHARAK, J. G. CHILDERS, and N. L. S. MARTIN, *J. Elec. Spec. Rel. Phen.* **141**, 75 (2004).
- [22] <http://www.varianinc.com/image/vimage/docs/products/vacuum/pumps/diffusion/shared/DiffusionPumps.pdf>.
- [23] D. ROY and D. TREMBLAY, *Rev. Prog. Phys.* **53**, 1621 (1990).
- [24] H. GOLDSTEIN, C. POOLE, and J. SAFKO, *Classical Mechanics*, Addison Wesley, third edition, 2002.
- [25] C. E. KUYATT and J. A. SIMPSON, *Rev. of Sci. Instr.* **38**, 103 (1967).
- [26] R. E. IMHOF, A. ADAMS, and G. C. KING, *J. Phys. E* **9**, 138 (1976).
- [27] P. HAYES, M. A. BENNETT, J. FLEXMAN, and J. F. WILLIAMS, *Rev. of Sci. Instr.* **59**, 2445 (1988).
- [28] Refer to the U.K. Dept. of Physics and Astronomy Electrons Shop documentation for project AT-73.
- [29] *About Your Enhanced Apple IIe: Programmer's Guide*, 1984, Apple Product #A2L2072.

- [30] <http://www.wmberg.com>.
- [31] C. B. OPAL, E. C. BEATY, and W. K. PETERSON, *At. Data* **4**, 209 (1972).
- [32] R. R. GORUGANTHU and R. A. BONHAM, *Phys. Rev. A* **34**, 103 (1986).
- [33] F. CATOIRE, E. M. STAIKU-CASAGRANDE, M. NEKKAB, C. DAL CAPPELLO, K. BARTSCHAT, and A. LAHMAM-BENNANI, *J. Phys. B* **39**, 2827 (2006).
- [34] A. LAHMAM-BENNANI, *J. Elec. Spec. Rel. Phen.* **123**, 365 (2002).
- [35] N. L. S. MARTIN, T. W. OTTLEY, and K. J. ROSS, *J. Phys. B* **13**, 1867 (1980).
- [36] A. LAHMANN-BENNANI, H. F. WELLENSTEIN, C. DAL CAPPELLO, M. ROUAULT, and A. DUGUET, *J. Phys. B* **16**, 2219 (1983).
- [37] N. L. S. MARTIN, R. P. BAUMAN, and M. WILSON, *Phys. Rev. A* **59**, 2764 (1999).
- [38] B. A. DEHARAK, Z. CHEN, D. H. MADISON, and N. L. S. MARTIN, *J. Phys. B* **40**, 755 (2007).
- [39] M. BRAUNER, J. S. BRIGGS, and H. KLAR, *J. Phys. B* **22**, 2265 (1989).
- [40] J. R. TAYLOR, *An Introduction to Error Analysis*, University Science Books, 2nd edition, 1997.
- [41] G. DU MAURIER, *Punch* **CIX**, 222 (1895).
- [42] G. LARSON, *The PreHistory of THE FAR SIDE A 10th Anniversary Edition*, Andrews and McMeel, 1989.
- [43] J. ULLRICH, R. MOSHAMMER, A. DORN, R. DÖRNER, L. P. H. SCHMIDT, and H. SCHMIDT-BÖCKING, *Rep. Prog. Phys.* **66**, 1463 (2003).
- [44] M. SCHULZ, R. MOSHAMMER, D. FISCHER, H. KOLLMUS, D. H. MADISON, S. JONES, and J. ULLRICH, *Nature* **422**, 48 (2003).
- [45] M. DÜRR, C. DIMOPOULOU, A. DORN, B. NAJJARI, I. BRAY, D. V. FURSA, Z. CHEN, D. H. MADISON, K. BARTSCHAT, and J. ULLRICH, *J. Phys. B* **39**, 4097 (2006).

- [46] M. DÜRR, C. DIMOPOULOU, B. NAJJARI, A. DORN, and J. ULLRICH, *Phys. Rev. Lett.* **96**, 243202 (2006).
- [47] R. W. VAN BOEYEN, N. WATANABE, J. W. COOPER, J. P. DOERING, J. H. MOORE, and M. A. COPLAN, *Phys. Rev. A* **73**, 032703 (2006).
- [48] B. A. DEHARAK, K. BARTSCHAT, and N. L. S. MARTIN, Out-of-plane ($e, 2e$) Experiments on Helium Autoionizing Levels., Submitted to *Phys. Rev. Lett.*
- [49] M. FOSTER, J. L. PEACHER, M. SCHULZ, D. H. MADISON, Z. CHEN, and H. R. J. WALTERS, *Phys. Rev. Lett.* **97**, 093202 (2006).
- [50] S. BELLM, J. LOWER, K. BARTSCHAT, X. GUAN, D. WEFLÉN, M. FOSTER, A. L. HARRIS, and D. H. MADISON, *Phys. Rev. A* **75**, 042704 (2007).
- [51] K. SCHULZ, G. KAINDL, M. DOMKE, J. D. BOZEK, P. A. HEIMANN, A. S. SCHLACHTER, and J. M. ROST, *Phys. Rev. Lett.* **77**, 3086 (1996).
- [52] J. P. VAN DEN BRINK, G. NIENHUIS, J. VAN ECK, and H. G. M. HEIDEMAN, *J. Phys. B* **22**, 3501 (1989).
- [53] B. A. DEHARAK, J. G. CHILDERS, and N. L. S. MARTIN, *Phys. Rev. A* **74**, 032714 (2006).
- [54] A. S. KHEIFETS, *J. Phys. B* **26**, 2053 (1993).
- [55] J. W. COOPER, U. FANO, and F. PRATS, *Phys. Rev. Lett.* **10**, 518 (1963).
- [56] M.-K. CHEN, *Phys. Rev. A* **56**, 4537 (1997).
- [57] D. R. HERRICK and O. SINANOĞLU, *Phys. Rev. A* **11**, 97 (1975).
- [58] C. D. LIN, *Phys. Rev. A* **29**, 1019 (1984).
- [59] M. DOMKE, K. SCHULZ, G. REMMERS, G. KAINDL, and D. WINTGEN, *Phys. Rev. A* **53**, 1424 (1996).
- [60] T. W. GORCZYCA, J.-E. RUBENSSON, C. SÅTHE, M. STRÖM, M. AGÅKER, D. DING, S. STRANGES, R. RICHTER, and M. ALAGIA, *Phys. Rev. Lett.* **85**, 1202 (2000).

- [61] R. P. MADDEN and K. CODLING, *Phys. Rev. Lett.* **10**, 516 (1963).
- [62] M. DOMKE, C. XUE, A. PUSCHMANN, T. MANDEL, E. HUDSON, D. A. SHIRLEY, G. KAINDL, C. H. GREENE, H. R. SADEGHPOUR, and H. PETERSEN, *Phys. Rev. Lett.* **66**, 1306 (1991).
- [63] A. MENZEL, S. P. FRIGO, S. B. WHITFIELD, C. D. CALDWELL, and M. O. KRAUSE, *Phys. Rev. A* **54**, 2080 (1996).
- [64] B. KRÄSSIG, E. P. KANTER, S. H. SOUTHWORTH, R. GUILLEMIN, O. HEMMERS, D. W. LINDLE, R. WEHLITZ, and N. L. S. MARTIN, *Phys. Rev. Lett.* **88**, 203002 (2002).
- [65] J. R. HARRIES, J. P. SULLIVAN, J. B. STERNBERG, S. OBARA, T. SUZUKI, P. HAMMOND, J. BOZEK, N. BERRAH, M. HALKA, and Y. AZUMA, *Phys. Rev. Lett.* **90**, 133002 (2003).
- [66] C. SÅTHE, M. STRÖM, M. AGÅKER, J. SÖDERSTRÖM, J.-E. RUBENSSON, R. RICHTER, M. ALAGIA, S. STRANGES, T. W. GORCZYCA, and F. RO-BICHEAUX, *Phys. Rev. Lett.* **96**, 043002 (2006).
- [67] K. C. PRINCE, M. CORENO, R. RICHTER, M. DE SIMONE, V. FEYER, A. KIVIMÄKI, A. MIHELIC, and M. ŽITNIK, *Phys. Rev. Lett.* **96**, 093001 (2006).
- [68] J. A. SIMPSON, G. E. CHAMBERLAIN, and S. R. MIELCZAREK, *Phys. Rev.* **139**, A1039 (1965).
- [69] N. ODA, F. NISHIMURA, and S. TAHIRA, *Phys. Rev. Lett.* **24**, 42 (1970).
- [70] P. J. HICKS and J. COMER, *J. Phys. B* **8**, 1866 (1975).
- [71] D. G. McDONALD and A. CROWE, *J. Phys. B* **25**, 2129 (1992).
- [72] A. CROWE, D. G. McDONALD, S. E. MARTIN, and V. V. BALASHOV, *Can. J. Phys.* **74**, 736 (1996).
- [73] M. J. BRUNGER, O. SAMARDZIC, A. S. KHEIFETS, and E. WEIGOLD, *J. Phys. B* **30**, 3267 (1997).

- [74] O. SAMARDZIC, L. CAMPBELL, M. J. BRUNGER, A. S. KHEIFETS, and E. WEIGOLD, *J. Phys. B* **30**, 4383 (1997).
- [75] H. B. VAN LINDEN VAN DEN HEUVELL, W. VAN DE WATER, H. G. M. HEIDEMAN, J. VAN ECK, and L. MOORMAN, *J. Phys. B* **13**, 2475 (1980).
- [76] P. J. HICKS, S. CVEJANOVIĆ, J. COMER, F. H. READ, and J. M. SHARP, *Vacuum* **24**, 573 (1974).
- [77] R. MORGENSTERN, A. NIEHAUS, and U. THIELMANN, *J. Phys. B* **10**, 1039 (1977).
- [78] P. W. ARCUNI, *Phys. Rev. A* **33**, 105 (1986).
- [79] P. W. ARCUNI and D. SCHNEIDER, *Phys. Rev. A* **36**, 3059 (1987).
- [80] P. MORETTO-CAPELLE, D. BORDENAVE-MONTESQUIEU, A. BORDENAVE-MONTESQUIEU, A. L. GODUNOV, and V. A. SCHIPAKOV, *Phys. Rev. Lett.* **79**, 5230 (1997).
- [81] K. IEMURA, S. OHTANI, H. SUZUKI, J. TAKEDA, S. MACHIDA, K. TANABE, T. TAKAYANAGI, K. WAKIYA, M. SEKIGUCHI, Y. KANAI, S. KITAZAWA, X. M. TONG, D. KATO, S. SAKAGUCHI, T. WATANABE, and F. J. CURRELL, *Phys. Rev. A* **64**, 062709 (2001).
- [82] P. BALTZER and L. KARLSSON, *Phys. Rev. A* **38**, 2322 (1988).
- [83] P. J. CHANTRY, *J. Chem. Phys.* **55**, 2746 (1971).
- [84] B. W. SHORE, *J. Opt. Soc. Am.* **57**, 881 (1967).
- [85] J. G. CHILDERS, B. A. DEHARAK, and N. L. S. MARTIN, *Phys. Rev. A* **69**, 042713 (2004).
- [86] D. H. OZA, *Phys. Rev. A* **33**, 824 (1986).
- [87] Y. K. HO, *Z. Phys. D* **21**, 191 (1991).
- [88] Y. K. HO, *Phys. Rev. A* **48**, 3598 (1993).

- [89] Y. K. HO, *Phys. Rev. A* **34**, 4402 (1986).
- [90] Y. K. HO and A. K. BHATIA, *Phys. Rev. A* **44**, 2895 (1991).
- [91] D. WINTGEN and D. DELANDE, *J. Phys. B* **26**, L399 (1993).
- [92] E. LINDROTH, *Phys. Rev. A* **49**, 4473 (1994).
- [93] L. WU and J. XI, *J. Phys. B* **23**, 727 (1990).
- [94] M. VENUTI, P. DECLEVA, and A. LISINI, *J. Phys. B* **29**, 5315 (1996).
- [95] A. MACÍAS and A. RIERA, *Phys. Lett. A* **119**, 28 (1986).
- [96] A. MACÍAS, F. MARTÍN, A. RIERA, and M. YÁNEZ, *Phys. Rev. A* **36**, 4187 (1987).
- [97] D. A. DAHL, *Int. J. Mass Spectrom.* **200**, 3 (2000).
- [98] R. BAIERLEIN, *Thermal Physics*, Cambridge University Press, 1999.
- [99] R. SNIEDER, *A Guided Tour of Mathematical Methods for the Physical Sciences*, Cambridge University Press, second edition, 2006.
- [100] A. V. OPPENHEIM, A. S. WILLSKY, and I. T. YOUNG, *Signals and Systems*, Prentice-Hall, 1983.

VITA

Bruno A. deHarak

Date and place of birth:

June 11, 1964, in New York City, New York

Educational institutions attended and degrees awarded:

2002	University of Kentucky Lexington, Kentucky B.S. cum laude, Physics
2006	University of Kentucky Lexington, Kentucky M.S., Physics

Professional positions held:

Research Assistant, University of Kentucky, 2002–2007
Teaching Assistant, University of Kentucky, 2004, 2005
Database Administrator, Yorkshire Global Restaurants, 1997–2002
Data Processor, Lockheed Martin Corporation, 1994–1997
Electronics Technician, Lockheed Martin Corporation, 1988–1994
Marine, United States Marine Corps, 1981–1988

Scholastic and professional honors:

Steckler Fellowship, 2006–2007
U.S. Dept. of Education Areas of National Need Fellowship, 2003–2004
University of Kentucky Summer Research and Creativity Grant, 2002

Publications

- B. A. deHarak, Z. Chen, D. H. Madison, and N. L. S. Martin, "Experimental and theoretical momentum transfer dependence of the He ($e, 2e$) cross section for incident electron energies 150 eV and 488 eV", J. Phys. B **40**, 755 (2007)
- B. A. deHarak, J. G. Childers, and N. L. S. Martin, "Ejected electron spectrum of He below the N=2 threshold", Phys. Rev. A **74**, 032714 (2006)
- B. A. deHarak, Z. Chen, D. H. Madison, N. L. S. Martin, "Experimental and theoretical momentum transfer dependence of the He ($e, 2e$) cross section", J. Phys. B letters. **38**, (10), L145-L152 (2005)
- B. A. deHarak, J. G. Childers, N. L. S. Martin, "Non-dipole effects in ($e, 2e$) and photoelectron experiments: a comparison", JESRP **130**, 75 (2004).
- J. G. Childers, B. A. deHarak, and N. L. S. Martin, "Ejected electron spectrum of Xe between the $^2P_{3/2}$ and $^2P_{1/2}$ ionic limits", Phys. Rev. A **69**, 042713 (2004).
- Y. V. Sushko, B. DeHarak, G. Cao, G. Shaw, D. K. Powell, J. W. Brill, "Hydrostatic pressure effects on the magnetic susceptibility of ruthenium oxide $\text{Sr}_3\text{Ru}_2\text{O}_7$: evidence for pressure-enhanced antiferromagnetic instability", Solid State Comm. **130**, 341 (2004).